NOVEL OBSERVER BASED FRICTION ESTIMATION AND CONTROL METHODS FOR SIMPLE NONLINEAR MECHANICAL SYSTEMS

A THESIS SUBMITTED TO

THE GRADUATE SCHOOL OF ENGINEERING AND SCIENCE

OF BILKENT UNIVERSITY

IN PARTIAL FULFILLMENT OF THE REQUIREMENTS FOR

THE DEGREE OF

MASTER OF SCIENCE

IN

ELECTRICAL AND ELECTRONICS ENGINEERING

By

Emre Orta

January 2025

Novel Observer Based Friction Estimation and Control Methods for Simple Nonlinear Mechanical Systems
By Emre Orta
January 2025

We certify that we have read this thesis and that in our opinion it is fully adequate, in scope and in quality, as a thesis for the degree of Master of Science.

Ömer Morgül(Advisor)

Naci Saldı

İsmail Uyanık

Approved for the Graduate School of Engineering and Science:

Orhan Arıkan
Director of the Graduate School

ABSTRACT

NOVEL OBSERVER BASED FRICTION ESTIMATION AND CONTROL METHODS FOR SIMPLE NONLINEAR MECHANICAL SYSTEMS

Emre Orta
M.S. in Electrical and Electronics Engineering
Advisor: Ömer Morgül
January 2025

Friction is a common nonlinear phenomenon in inertial mechanical systems, often leading to undesirable effects such as stick-slip motion, hysteresis, and reduced tracking accuracy. Effective friction compensation is essential for enhancing robustness and achieving high precision in controlling such systems. Both model-based and non-model-based approaches have been widely utilized for friction compensation, with friction observers playing a significant role in estimating the friction acting on the system. This study focuses on observer-based adaptive estimation techniques, specifically employing the Friedland-Park observer to estimate the parameters of a friction model in an inertial system. The proposed approach aims to mitigate stick-slip motion and enhance tracking performance. The research evaluates various applications of the Friedland-Park observer for friction compensation and its implementation in high-order systems. Both two-state and single-state observers are examined, alongside different system models and controllers, to ensure the robustness of the proposed methods. Performance metrics include velocity reference tracking accuracy and the compensator's responsiveness during velocity sign reversals, assessed under diverse reference input conditions. Simulation results demonstrate a significant improvement in velocity tracking accuracy, with up to a 65% reduction in tracking error. The proposed friction compensation methods effectively handle varying friction conditions, ensuring system robustness and precision. This study contributes a comprehensive approach to friction compensation, offering various design options for inertial mechanical systems. Future work will extend this research by incorporating a gyroscope model to address the noisy nature of inertial sensors and performing the hardware implementation of the proposed methodology on gyro-stabilized platforms to validate its practical applicability. This work can also be extended within the scope of system identification by developing a novel approach for estimating

plant parameters through the adaptation of Friedland-Park observer equations.

Keywords: Observer-based friction estimation, Friction modelling, Friction compensation, Adaptive control, Stick-slip phenomena, Reference tracking.

ÖZET

BASİT DOĞRUSAL OLMAYAN MEKANİK SİSTEMLER İÇİN YENİ GÖZLEMCİ TABANLI SÜRTÜNME TAHMİNİ VE KONTROL YÖNTEMLERİ

Emre Orta
Elektrik ve Elektronik Mühendisliği, Yüksek Lisans
Tez Danışmanı: Ömer Morgül
Ocak 2025

Sürtünme, ataletsel mekanik sistemlerde yaygın olarak görülen doğrusal olmayan bir olgudur ve genellikle tutma-bırakma hareketi, histerezis ve takip doğruluğunun azalması gibi istenmeyen etkilere yol açar. Bu tür sistemlerin kontrolünde yüksek hassasiyet ve gürbüzlük sağlamak için etkili sürtünme telafisi büyük önem taşımaktadır. Hem model tabanlı hem de model tabanlı olmayan yöntemler sürtünme telafisinde yaygın olarak kullanılmakta olup, sürtünme gözlemcileri, sistemdeki sürtünmenin tahmin edilmesinde önemli bir rol oynamaktadır. Bu çalışma, gözlemci tabanlı uyarlamalı tahmin tekniklerine odaklanmakta ve özellikle Friedland-Park gözlemcisini kullanarak bir ataletsel sistemdeki sürtünme modelinin parametrelerini tahmin etmeyi amaçlamaktadır. Önerilen yaklaşım, tutma-bırakma hareketini azaltmayı ve takip performansını artırmayı hedeflemektedir. Bu araştırma, Friedland-Park gözlemcisinin sürtünme telafisi uygulamalarını ve yüksek mertebeli sistemlerdeki kullanımını değerlendirmektedir. İki durumlu ve tek durumlu gözlemciler ile farklı sistem modelleri ve denetleyiciler, önerilen yöntemlerin sağlamlığını sağlamak için incelenmiştir. Performans ölçütleri, hız referans takibi doğruluğu ve hız yön değişiklikleri sırasında telafi edicinin tepki verme yeteneği gibi unsurları kapsamaktadır ve çeşitli referans giriş koşulları altında değerlendirilmiştir. Simülasyon sonuçları, hız takibi doğruluğunda önemli bir iyileşme sağlandığını ve hız takip hatasında %65'e varan bir azalma olduğunu göstermektedir. Önerilen sürtünme telafisi yöntemleri, değişken sürtünme koşullarını etkili bir şekilde yöneterek sistemin gürbüzlüğünü ve hassasiyetini sağlamaktadır. Bu çalışma, ataletsel mekanik sistemler için sürtünme telafisine kapsamlı bir yaklaşım sunarak çeşitli tasarım seçenekleri sunmaktadır. Gelecek çalışmalar, ataletsel

sensörlerin gürültülü doğasını ele almak amacıyla bir jiroskop modelinin entegrasyonunu ve önerilen metodolojinin pratik uygulanabilirliğini doğrulamak için jiroskop stabilizasyonlu platformlarda uygulanmasını içerecektir. Ayrıca, bu çalışma, Friedland-Park gözlemci denklemlerinin uyarlanması yoluyla sistem parametrelerinin tahmini için yeni bir yaklaşım geliştirilerek sistem tanımlama bağlamında da genişletilebilir.

Anahtar sözcükler: Gözlemci tabanlı sürtünme tahmini, Sürtünme modellemesi, Sürtünme telafisi, Adaptif kontrol, Tutma-bırakma olgusu, Referans takibi.

Acknowledgement

First, I would like to express my deepest gratitude to my advisor, Prof. Dr.Ömer Morgül, for their invaluable guidance, encouragement, and support throughout the journey of this thesis. His insights and expertise have been instrumental in shaping this work, and his mentorship has profoundly influenced my academic and personal growth. I am also highly grateful to Asst. Prof. Naci Saldı and Assoc. Prof. İsmail Uyanık for their involvement in my thesis committee.

Finally, I am profoundly thankful to my family for their unconditional love and encouragement. To my parents, thank you for your unwavering belief in me and for the sacrifices you have made to support my education. Thank you for your patience, understanding, and encouragement throughout this journey.

Contents

List of Figures

List of Tables

Chapter 1

Introduction

Friction is a ubiquitous nonlinear phenomenon in mechanical systems that profoundly influences their dynamics and control behavior. It arises from the interaction between surfaces in relative motion and manifests in various forms, such as static, kinetic, or viscous friction, each governed by distinct physical principles. In control systems such as servomechanisms, friction introduces nonlinearities to the system, such as hysteresis and stick-slip motion, which can degrade performance. These effects are particularly pronounced in precision systems, where even minor frictional forces can lead to steady-state and tracking errors, limit cycles, instability or stick-slip motion. Consequently, identifying friction characteristics and counteracting its adverse effects is crucial to system performance. To this end, numerous studies focus on modeling and compensating for friction. In the literature, friction models often appear as extensions or more complex versions of previous studies. Each model focuses on specific aspects of friction behavior, creating the need to classify them into static and dynamic friction models. To motivate our analysis, let us consider a single mass m moving in one direction with velocity v under the effect of a force F. The basic Newtonian equation of motion resulting from conservation of linear momentum can be given as

$$m\dot{v} = F - F_c, \tag{1.1}$$

where F_c represent any force effect which opposes to the motion, which is the friction in our case. Obviously a similar equation can be given for a rotating body in one dimension. The most simple static friction model that represents the friction force in (1.1), is Coulomb friction described as

$$F_c = \mu F_n \operatorname{sign}(v). \tag{1.2}$$

F_n represents the normal force, μ is the coefficient of friction and v is the relative velocity. Coulomb friction model can be extended by adding a term proportional to the velocity, representing viscous friction by σ in (1.3). This addition models fluid-like effects in contact interface [1].

$$F_c = \mu F_n \operatorname{sign}(v) + \sigma v. \tag{1.3}$$

Combination of Coulomb and viscous friction is not sufficient to model the friction at rest. There is a concept called Stiction described as the resistance to the initiation of motion between two surfaces [2]. Therefore, the Stiction model focuses on the force required to overcome static friction and initiate motion. It assumes a sharp transition between the static and kinetic friction states. Stribeck effect described in [3] introduces a smooth curve for this transition. Using the Stribeck curve with the friction models mentioned earlier, a model is obtained that is more reflective of real-world systems since it provides a continuous friction force and maintains the velocity dependency. The main contribution of Stribeck effect is that the friction force does not change suddenly but gradually decreases as the velocity increases. Hence, using Stribeck curve in friction modeling can address the challenges of low-speed regimes. The Stribeck curve is defined as

$$F(v) = F_c + (F_s - F_c)e^{-|v/v_s|^\delta} + \sigma v, \tag{1.4}$$

where v_s is Stribeck velocity and δ is friction decay rate. The resulting friction model with Stribeck effect is, therefore

$$F_f = \begin{cases} F(v) & \text{if } v \neq 0, \\ F_a & \text{if } v = 0 \text{ and } |F_a| < F_s, \\ F_s \operatorname{sign}(F_a) & \text{otherwise.} \end{cases} \tag{1.5}$$

The applied and the total forces are represented by F_a and F_f, respecively. $F(v)$ is the Stribeck force defined in (1.4) and F_s is the static friction force.

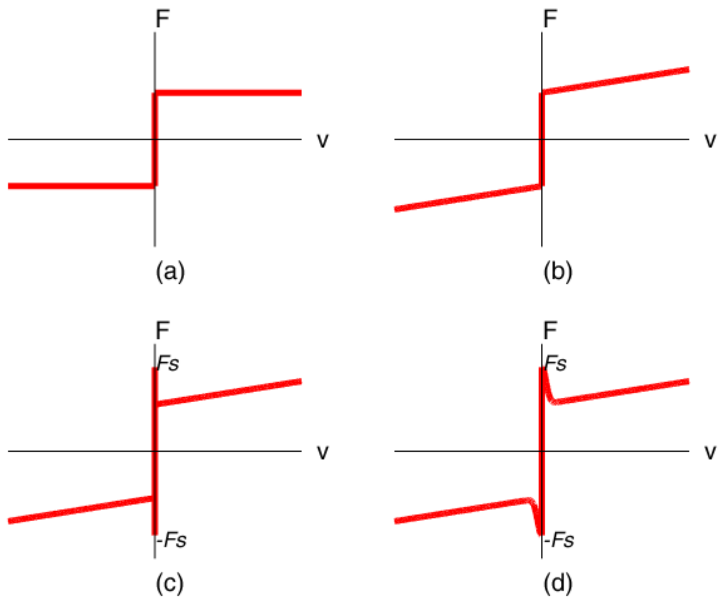

Figure 1.1: Friction forces with respect to velocity for static friction models. (a) Coulomb Model, (b) Coulomb+Viscous Model, (c) Coulomb+Viscous+Stiction Model, (d) Stribeck Model

The behavior of the friction forces with respect to velocity of the static models are shown in Figure 1.1. The friction models described up to this point are static friction models, meaning that they lie on the assumption of having no motion without sliding. Before full motion occurs, systems often experience pre-sliding displacement, a micro-level deformation of surface asperities. This behavior is characterized by elasticity and hysteresis, as highlighted in [4]. The asperities deform when force is applied. As the applied force exceeds the breakaway force, asperity junctions break and sliding occurs [5]. Pre-sliding concept becomes crucial in systems that experiences stick-slip motion. Stick-slip occurs when the force surpasses the maximum static friction (breakaway force), causing abrupt sliding followed by a return to the pre-sliding regime as the velocity decreases [6]. The transitions between stick and slip phases occur in cycles, creating oscillations

[7]. This oscillatory nature of stick-slip creates a highly nonlinear and discontinuous velocity profile. These oscillations create challenges in systems such as gyro-stabilized platforms where the stick-slip motion generates chattering in velocity reversals. This degrades the performance of the system especially during target tracking applications where the objective is to track an object with very low frequency velocity command. In robotics, the stick-slip phenomenon is also undesirable behavior since it may cause erratic motion and poor tracking performance. In [8], a novel friction model is proposed and validated on KUKA IR 361 industrial robot joint. The measured stick-slip motion closely matches the model's predictions, improving the tracking performance of the robot.

In order to have a smooth and more accurate transition between stick and slip phases, pre-sliding has to be modeled. Friction models that account pre-sliding are called dynamic friction models. Dahl friction model introduced in [4] treats friction as an elastic deformation of surface asperities. Hence, the friction is modeled as a differential equation of a stress-strain curve given in (1.6). It models friction force as a function of displacement rather than velocity alone. The Dahl model can be considered as a milestone in friction modeling since it provides insights into pre-sliding and hysteresis behavior and it pioneered the dynamic models that were later introduced. More precisely, the friction force F_f is given as

$$\frac{dF_f}{dx} = \sigma(1 - \frac{F_f}{F_c}\,\mathrm{sign}(v))^{\alpha}, \tag{1.6}$$

where F_f is the friction force, F_c is the Coulomb friction, σ is stiffness coefficient and α is a curve shaping parameter. Another dynamic model that is widely used in literature is LuGre friction model proposed in [6]. In LuGre model, friction is conceptualized as the mean deflection force exerted by elastic bristles, which behave like springs. When a tangential force is applied, these bristles deform elastically. However, if the deformation exceeds a certain threshold, the bristles begin to slip [9]. The model introduces an internal state variable z to represent the average deformation of microscopic bristles at the contact surface. This variable evolves dynamically with time and reflects the system's internal friction state [10]. The model can be expressed in the following form:

$$\frac{dz}{dt} = v - \sigma_0 \frac{|v|}{g(v)} z \tag{1.7}$$

$$F_f = \sigma_0 z + \sigma_1 \frac{dz}{dt} + \sigma_2 v, \tag{1.8}$$

where z is the internal state variable, σ_0 the stiffness of the bristles, σ_1 the micro-damping coefficient, σ_2 the viscous friction coefficient and $g(v)$ is the Stribeck function described in (1.4). Identifying the parameters of LuGre model is not a trivial task. The parameters are classified as static and dynamic parameters. The static parameters are identified by doing constant velocity experiments. During these experiments, the torque is measured for different range of velocities. The collected data is then fitted to a curve to obtain a friction-velocity map. By using this map, one can identify the viscous coefficient, Coulomb and static friction torques. For identifying dynamic parameters, friction vs position curve is obtained and σ_0 can be identified from the slope of this curve under the assumption that $\dot{z}$ is constant. Then σ_1 can be found from (1.7). In [11], identification of the LuGre model parameters and evaluation of the model performance in terms of stability and tracking are implemented for a gyro-stabilized gun turret system. It is observed that LuGre friction model effectively reduces the stick-slip behavior and it decreases the stabilization error under low frequency disturbances. An adaptive compensation method is proposed in [12] that estimates and compensates for friction disturbances modeled by the LuGre friction model within electromechanical actuator servo systems. Another application of LuGre friction model is given in [13]. The work investigates the design and implementation of an observer-based friction compensation system using the LuGre friction model. While the article highlights the practical utility of the LuGre model and the observer framework, a major contribution of the study is the development of a new discretization approach for implementing the observer in real-time. Experimental validation on a DC motor with a rigid arm demonstrates the efficacy of the proposed method, showing improved performance in reducing tracking errors, particularly during low-velocity or stiction-dominated phases.

After examining various friction models and their applications, we now address the friction compensation problem, which gives rise to the need for friction modeling. Friction compensation, as mentioned at the beginning of the chapter, is a technique used to mitigate the adverse effects of friction in a system. It can be classified into two as model based and non-model based approaches. Model based friction compensation techniques rely on the identification of the parameters of friction models described earlier. The simple idea in model-based friction compensation is to add the estimated friction force to the control signal [5]. The compensation can be made either feedforward or feedback. In feedforward compensation, a predetermined estimate of the friction force is directly added to the control signal. Whereas in feedback compensation, real-time error signals are used to adjust the control input. To achieve that, observers are commonly used along with the friction model. Different observer structures such as disturbance observers (DOB), Extended Kalman Filter (EKF) [14], sliding mode observers and adaptive observers can be used for friction compensation. Disturbance observer (DOB) estimates disturbances such as friction by modeling them as unknown inputs to the system. In [15], a hybrid approach to friction compensation is presented that combines model-based feedback control with a disturbance observer (DOB) on an XY feed table. The feedforward component utilizes a detailed friction model called Generalized Maxwell-Slip (GMS) model. For the observer, inverse model disturbance observer is used. The results given in [15] demonstrates that the combination of feedforward compensation and the DOB enhances tracking performance significantly compared to using either method alone. It is also shown that the closed-loop system bandwidth is increased which enhances the disturbance rejection and tracking in low frequencies. A novel adaptive controller that incorporates a sliding mode observer to estimate the internal friction state of the LuGre model of servo actuators is proposed in [16]. [17] uses a LuGre model and an adaptive observer structure that is designed to estimate the parameters of the friction model, such as stiffness and damping coefficients. A very recent study in [18] focuses on designing a robust adaptive observer for (PMSM)-based servo systems to update the LuGre model parameters. It enhances the design with a neural network approach by using radial basis function (RBF) to guarantee the convergence of the estimation error.

Unlike model based approaches, the friction compensation methods that do not rely on explicit mathematical model of friction are called non-model based friction compensation methods. Non-model based methods are often simpler to implement since identification of friction model parameters may be computationally demanding. The most simple approach is to inject a Dither signal [19] which refers to high-frequency, small-amplitude signal that is added to the control input. The purpose is to reduce the effect of stick-slip behavior, by effectively linearizing the friction force at low velocities. For instance, [20] uses a sliding mode control approach with Dither signal to avoid the chattering effect caused by stick-slip behavior. Furthermore, observers are commonly used in non-model based friction compensation. [21] compares a disturbance observer with model-based techniques for friction compensation in machine tool tables, highlighting the observer's effectiveness in pre-sliding regimes. Similarly in [22], different non-model based method is proposed using two observers as a generalized momenta observer and a velocity observer. The observers use the estimations of each other to improve the quality of the estimations.

Friction is a highly nonlinear phenomena and it depends on various factors such as normal force, position, temperature and surface conditions [9]. Due to the varying nature of friction, adaptive friction compensation is often preferred regardless of whether a friction model is used or not. The study in [23] addresses this varying nature where the friction depends not only on velocity but also on position. An observer-based adaptive control framework is proposed along with LuGre friction model. The observer estimates the internal states in the model. The work also investigates methods for approximating the friction dependency. Some other approaches of adaptive friction compensation in robotics field are proposed in [24, 25, 26]. They all use Lyapunov-based stability analysis to design an adaptive law for friction compensation.

Finally, we examine an observer-based adaptive friction compensation method as proposed in [27]. This method introduces a nonlinear observer known as the Friedland-Park observer, designed specifically for estimating Coulomb friction in dynamic systems. The observer models friction as a constant scaled by the sign of the velocity and employs an adaptive control mechanism to estimate this constant. A key advantage of this approach is that it does not require direct velocity measurement, relying instead on the velocity's direction. This feature makes it particularly suitable for systems where velocity measurements are noisy, such as gyro-stabilized platforms. In the literature, the Friedland-Park observer has been widely adopted and extended for friction estimation and compensation across various mechanical systems. For instance, [28] investigates adaptive observer-based friction compensation techniques, using the Friedland-Park observer to estimate Coulomb friction in mechanical systems, including those with time delays. The study establishes necessary conditions to extend the observer's estimation capabilities to a broader class of functions, enhancing its applicability. Moreover, challenges associated with measurement delays are addressed by incorporating velocity predictors based on numerical differential equation solvers or inverse Padé approximations. The findings indicate that observer-based friction compensation significantly improves system performance, even when actual friction deviates from the Coulomb model, particularly in systems with low-bandwidth controllers. Additionally, a novel observer inspired by the Friedland-Park structure for estimating and compensating LuGre friction is presented in [29]. This study provides a Lyapunov stability analysis to demonstrate the asymptotic stability of the observer dynamics under specific conditions. The proposed observer estimates velocity and incorporates velocity error, alongside control input, to enhance friction estimation. This improvement results in better position and velocity tracking performance in the presence of friction.

This dissertation introduces the Friedland-Park observer and explores its applications in the literature, aiming to extend its functionality for friction estimation in simple nonlinear mechanical systems. The primary contribution of this study is the development of a novel observer-based two-state friction estimation technique for various reference inputs. The proposed observer is designed to estimate the unknown parameters of the friction model, offering flexibility in adapting to varying friction characteristics across different systems. Friction exhibits diverse behaviors depending on the system, with certain nonlinear effects being more pronounced in some contexts. Accurate friction modeling is essential to ensure that the model effectively captures the undesirable nonlinear phenomena present in the system. To address this, the study introduces an observer design that can be adapted to various friction models, thereby broadening its applicability. Another significant contribution of this dissertation is the investigation of alternative structures of the Friedland-Park observer. By appropriately formulating the state equations, the observer can estimate plant model parameters. This capability extends the scope of the study to system identification applications. In practical applications, plant models are often much complex and require representation through high-order transfer functions. To address this complexity, the study implements a friction estimator designed for high-order systems, incorporating various control methods to enhance performance. These contributions collectively advance the applicability of the Friedland-Park observer in friction estimation.

The study is organized into three main chapters, followed by a concluding section and an appendix. Chapter 2 focuses on exploring various structures of the Friedland-Park observer, with an emphasis on modifications to address the friction compensation problem and their impact on system performance. Chapter 3 introduces the implementation of the friction compensation method for high-order plant models. This chapter provides a detailed analysis of the system by employing two distinct controllers to evaluate the proposed approach. In Chapter 4, the novel two-state friction estimator is presented, along with its application to different friction models, demonstrating its adaptability and effectiveness in handling diverse nonlinear friction phenomena. Chapter 5 serves as the concluding section, summarizing the key findings and evaluating the overall outcomes of the study. Additionally, the Appendix section includes supplementary materials such as additional figures, simulation models, and implementation codes to support and enhance the concepts discussed in the main chapters.

Chapter 2

Friction Compensation Applications with Friedland-Park Observers

In this chapter, the applications of the Friedland-Park observer to friction compensation are discussed. We formulate the friction compensation problem based on a rotational mass-damper system and incorporate the Coulomb friction model as the friction component. From Newton's second law of motion for rotation, it is known that

$$J\alpha = T_n, \tag{2.1}$$

where T_n is the net torque acting on the system, J is the moment of inertia and α is the angular acceleration. The net torque can be expressed as the difference between the applied and friction torques,

$$J\dot{w} = T - T_f. \tag{2.2}$$

The angular velocity is denoted by w and $\dot{w}$ is therefore the angular acceleration. T is the applied torque and T_f is the friction torque defined as

$$T_f = k\,\mathrm{sign}(w) + bw, \tag{2.3}$$

where k is the Coulomb friction torque and b is the viscous damping coefficient. Substituting (2.3) to (2.2) results in the general system model used in this study:

$$J\dot{w} = u_n - k\,\text{sign}(w) - bw. \tag{2.4}$$

The applied torque T is substituted with u_n for generalization, where u_n represents the nominal input applied to the system. The underlying concept is that, if k is known, the friction component can be compensated by appropriately designing u_n. Hence, u_n can be defined as

$$u_n = u + k\,\text{sign}(w), \tag{2.5}$$

where u is the input applied to the system. By substituting (2.5) into (2.4), the ideal scenario is obtained in which k is assumed to be perfectly known:

$$J\dot{w} = u - bw. \tag{2.6}$$

By taking the Laplace Transform of the system described in (2.6), the transfer function from input u to angular velocity w can be written as

$$JsW(s) = U(s) - bW(s). \tag{2.7}$$

Rearranging the equation by grouping the terms on both sides, we obtain

$$\frac{W(s)}{U(s)} = \frac{1}{Js + b}. \tag{2.8}$$

Having derived the transfer function of the plant, the generalized structure of the feedback control system, as shown in Figure 2.1, can be established.

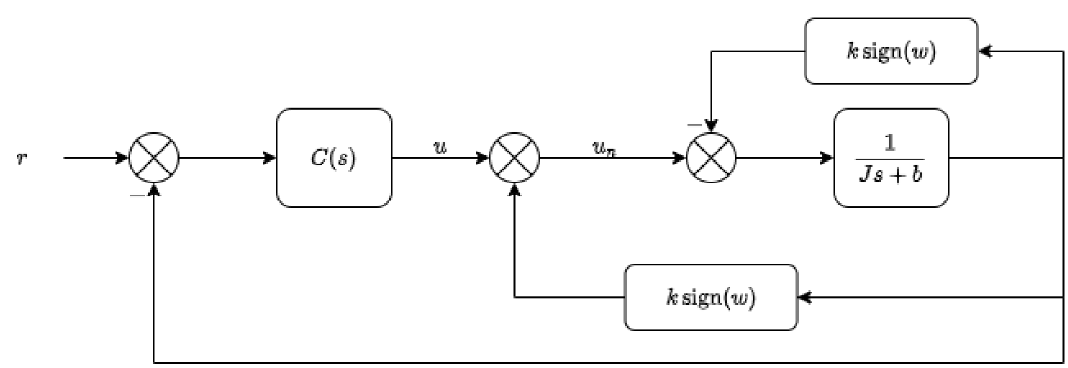

Figure 2.1: Generalized feedback system

In Figure 2.1, r is the angular velocity reference input and $C(s)$ is the velocity controller. In the preceding sections, various configurations of this system have been analyzed through simulations in the context of friction compensation, employing the Friedland-Park observer. The simulations are performed in MATLAB Simulink environment.

2.1 Case 1: Friction Compensation Using the Classical Friedland-Park (CFP) Observer

In the system described in 2.1, it is assumed that the parameters k and b are known. To formulate the friction compensation problem, the viscous damping coefficient b is considered known, while the Coulomb friction coefficient k is treated as an unknown parameter. Estimating k and compensating for friction constitute the foundation of the classical Friedland-Park observer approach. The classical FP observer is a nonlinear reduced-order Coulomb friction observer proposed in [27]. Let $\hat{k}$ denote the estimate of k. Consequently, the expression for u_n and the differential equation that describes the system model that are defined in (2.5) and (2.4) respectively, become

$$u_n = u + bw + \hat{k}\,\mathrm{sign}(w) \tag{2.9}$$

$$J\dot{w} = u - k\,\mathrm{sign}(w) + \hat{k}\,\mathrm{sign}(w). \tag{2.10}$$

The feedback system to be analyzed is presented in Figure 2.2. By applying block diagram manipulations, the upper block diagram can be simplified to the one shown at the bottom, given that b is assumed to be known.

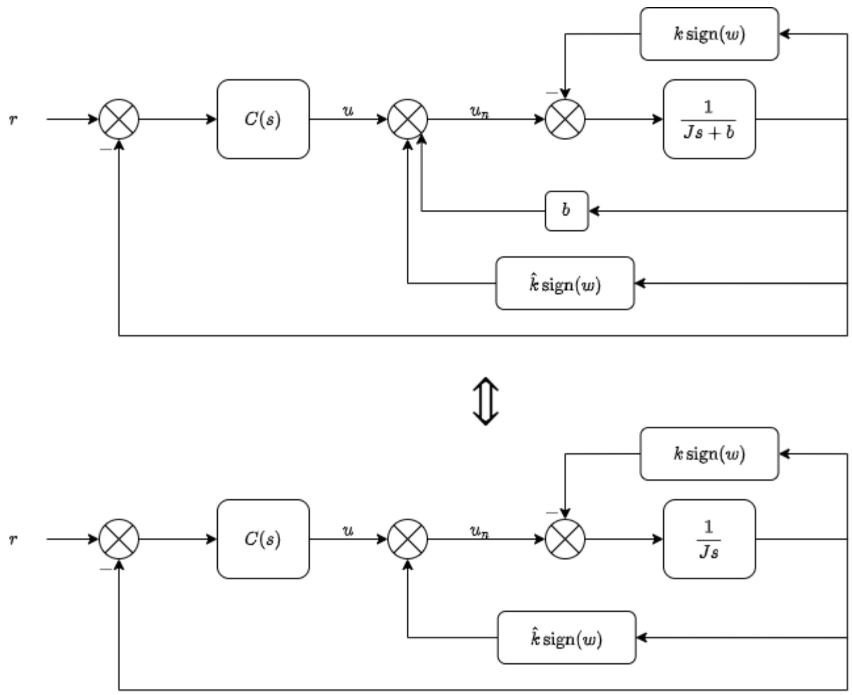

Figure 2.2: System model with friction estimator

Following the introduction of the general structure of the feedback system, the design of the CFP observer will be undertaken. The CFP observer is defined by the following set of equations:

$$\dot{z} = \frac{u}{J} g'(w) \tag{2.11}$$

$$\hat{k} = z - g(w), \tag{2.12}$$

where z represents the state of the observer and $g(w)$ is an appropriate nonlinear function defined as $g(\cdot) : \mathbb{R} \to \mathbb{R}$

To identify the type of nonlinearity $g(w)$, the derivative of the estimation error is as follows:

$$e_k = k - \hat{k} \tag{2.13}$$

$$\dot{e}_k = -\dot{\hat{k}} = -\dot{z} + g'(w)w'. \tag{2.14}$$

Substituting $\dot{z}$ in (2.11) and $\dot{w}$ in (2.10) into (2.14) we obtain

$$\dot{e_k} = -\frac{u}{J}g'(w) - g'(w)\,\mathrm{sign}(w)\frac{e_k}{J} + \frac{u}{J}g'(w) \tag{2.15}$$

$$= -g'(w)\,\mathrm{sign}(w)\frac{e_k}{J}. \tag{2.16}$$

Through this process, the condition on $g'(w)$ is derived to make the estimation error asymptotically stable. Analyzing the estimation error in terms of stability is crucial since asymptotic stability of e_k implies that $e_k(t) \to 0$ as $t \to \infty$. Considering the error dynamics described in (2.16), the error e_k is asymptotically stable if $g'(w)\,\mathrm{sign}(w) > 0$, $\forall w \neq 0$. Let us define the Lyapunov function as

$$V(e_k) = \frac{1}{2}e_k^2. \tag{2.17}$$

Taking the time derivative of the Lyapunov function yields

$$\dot{V}(e_k) = e_k\dot{e}_k = -g'(w)\,\mathrm{sign}(w)\frac{e_k^2}{J}. \tag{2.18}$$

For $\dot{V}(e_k) < 0$, we need to have $g'(w)\,\mathrm{sign}(w) > 0$, $\forall w \neq 0$ since J is a positive constant. One can observe that the function $g'(w)$ must lie in the first and third quadrants in the Cartesian plane to satisfy $g'(w)\,\mathrm{sign}(w) > 0$. Hence, $g'(w)$ belongs to a sector $[0, \infty]$.

Remark 1. *A function $h(\cdot) : \mathbb{R} \to \mathbb{R}$ is said to belong to a sector $[\alpha, \beta]$ ($h(.) \in [0, \infty]$) if the following condition holds,*

$$\alpha w^2 \leq wh(w) \leq \beta w^2. \tag{2.19}$$

Exponential stability of the error dynamics which ensures a stronger condition for rapid convergence can be shown as described in Lemma 1 [30], [31].

Lemma 1. *In system defined in (2.16), assume $g'(w) \in [0, \infty]$ with $g(w) \neq 0$ and $g'(w) \neq 0$ for $w \neq 0$. If $|w| > 0$ $\forall t$, then the error dynamics is exponentially stable.*

Proof. For $g'(w) \in [0, \infty]$, we have $-g'(w)\,\mathrm{sign}(w)\frac{e_k}{J} \geq 0$. Under this assumption, for $|w| > 0$, the following condition, $-g'(w)\,\mathrm{sign}(w)\frac{e_k}{J} > \beta$ holds for some $\beta > 0$.

The associated Lyapunov function can be defined as in (2.17). Differentiating it by using the error dynamics described in (2.16), we obtain

$$\dot{V}(e_k) = e_k \dot{e}_k \leq -\beta e_k^2 = -2\beta V. \tag{2.20}$$

By expressing the solution of differential inequality in (2.20) explicitly, the following is obtained:

$$\dot{V}(t) \leq e^{-2\beta t} V(0). \tag{2.21}$$

Therefore, we have

$$|e(t)| \leq e^{-\beta t} |e(0)|. \tag{2.22}$$

The decay in (2.22) is exponential, which concludes the proof of exponential stability using a Lyapunov function. □

In [30], the exponential stability of e_k is also deduced by the persistent excitation principle described in Lemma 2.

Lemma 2. *Let $w(t)$ be the solution to system described in (2.16) and let $G(t)$ be defined as*

$$G(t) = \frac{g'(w(t)) sign(w(t))}{J}. \tag{2.23}$$

Assume that the following condition

$$\int_t^{t+T} G(s)\, ds \geq \alpha, \tag{2.24}$$

holds for some $\alpha > 0$ and $T > 0$ for all $t \geq 0$. Then, $e_k \to 0$ as $t \to 0$ exponentially fast which implies the exponential stability of e_k.

Proof. The explicit solution of the error dynamics is given as

$$e_k(t) = e^{-\int_0^t G(s)\, ds} e_k(0). \tag{2.25}$$

Let $t = kT + \tau$ for some positive integer k and $0 < \tau < T$. Then, using the condition in (2.24), we obtain

$$\int_0^t G(s)\, ds = \int_0^T G(s)\, ds + \int_T^{2T} G(s)\, ds + ... + \int_{(k-1)T}^{kT+\tau} G(s)\, ds \;\geq k\alpha. \tag{2.26}$$

Plugging (2.26) into (2.25), yields

$$|e_k(t)| \leq e^{-k\alpha}|e_k(0)|, \tag{2.27}$$

since $G(s)$ is positive definite. Hence, $e_k(t)$ converges exponentially to 0 due to the exponential decay in (2.27). □

To conclude, the condition given in (2.22) is satisfied for inputs where $|w(t)| > 0$. This condition holds, for instance, in the case of step inputs where the sign of velocity does not change with time. However, for sinusoidal signals with a period T, $|w(t)| > 0$ is not guaranteed at all times. Therefore, Lemma 2 is employed to evaluate exponential stability for periodic signals where Lemma 1 may not hold.

Selection of $g(w)$ that satisfies the conditions for exponential stability is a design preference since it affects the observer performance. Therefore, three distinct nonlinear functions are used, each of which satisfies the necessary stability conditions as defined below:

$$g_1'(w) = \alpha w \rightarrow g_1(w) = \frac{\alpha}{2}w^2 \tag{2.28}$$

$$g_2'(w) = \alpha\,\mathrm{sign}(w) \rightarrow g_2(w) = \alpha|w| \tag{2.29}$$

$$g_3'(w) = \alpha\tanh(\lambda w) \rightarrow g_3(w) = \frac{\alpha}{\lambda}\ln(\cosh(\lambda w)), \tag{2.30}$$

where $\alpha > 0$ and $\lambda > 0$ are adjustable parameters. $g_2(w)$ is the nonlinear function that is used in [27]. The effects of these functions with varying parameters on the estimator's performance will be compared in terms of accuracy and convergence.

After introducing the observer structure, the block diagram of the friction estimator can be illustrated as shown in Figure 2.3. The simulations are made based on this feedback system. A PI velocity controller, $C(s)$, that stabilizes the plant $\frac{1}{Js}$ is used. The PI controller parameters are tuned in the absence of the estimator to better highlight the impact of the compensation strategy, as the controller reduces the effects of friction to a certain degree. The parameters are obtained according to the step response of the system that satisfies the 2% criterion of settling time and 10% maximum overshoot. The numerical values of the parameters to be used in the simulation are presented in Table 2.1.

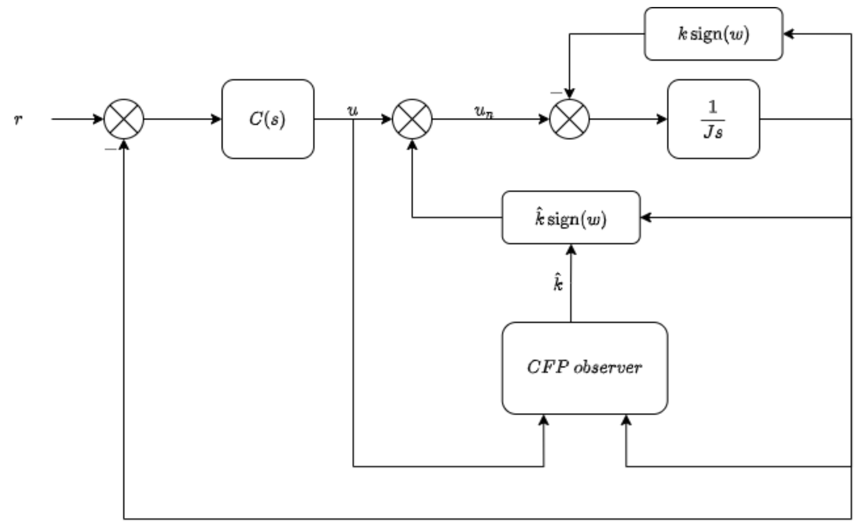

Figure 2.3: System model with CFP observer

Table 2.1: Simulation Parameters for Case 1

Parameter	Value	Unit
Moment of inertia (J)	10	kgm^2
Coulomb friction (k)	20	Nm
Proportional controller gain (k_p)	150	
Integral controller gain (k_i)	200	
Sampling time	0.0001	sec

The simulation duration is 0.5 seconds and the reference input used in the simulation is a 10 Hz sine wave with an amplitude of 1. Sine wave angular velocity reference is preferred to capture the performance in zero velocity crossings. The angular velocity response of the system and the estimated friction torques for four different α values are presented in Figure 2.4 and 2.5, respectively.

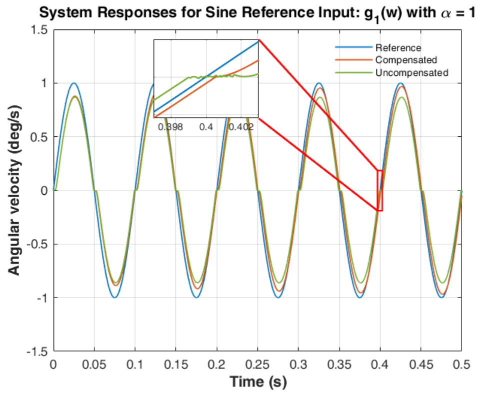

(a) Angular velocities for $\alpha = 1$

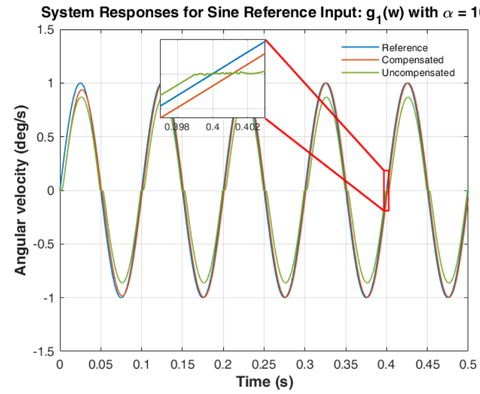

(b) Angular velocities for $\alpha = 10$

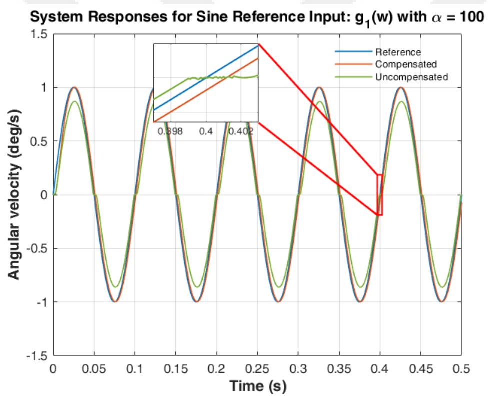

(c) Angular velocities for $\alpha = 100$

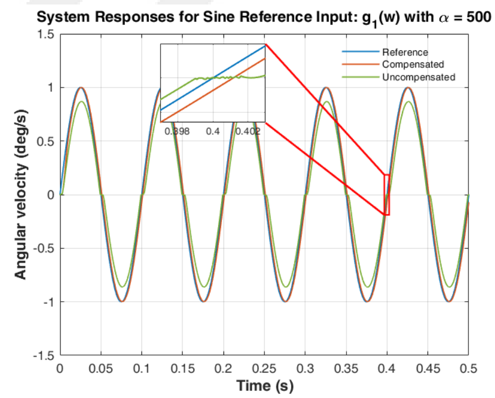

(d) Angular velocities for $\alpha = 500$

Figure 2.4: Friction compensated and uncompensated angular velocity responses of the system for 10 Hz sine wave input with different α parameters of $g_1(w)$

In Figure 2.4, the angular velocity responses of the system for cases with and without friction compensation are presented. There are four graphs for four different α values of the nonlinearity $g_1(w)$ that is used in CFP observer. It can be observed that stick-slip behavior dominates around velocity reversals in the uncompensated case. In contrast, with friction compensation, the chattering effect of the stick-slip phenomenon is not observed near zero velocity. The effect of the α parameter can be also seen from the angular velocity graphs since a better reference tracking is achieved with higher values of α. The reason for improved tracking performance is directly related to the friction estimation shown in 2.5. The figure illustrates the Coulomb friction acting on the system and its estimations for four different α values. An evaluation of the friction torque graphs alongside the corresponding angular velocities in Figure 2.4 reveals that the tracking performance improves with more accurate friction estimation. As α increases, the convergence time of the friction estimation to the existing friction acting on the system decreases, resulting in improved tracking performance in the system response. Hence, it can be concluded that increasing the α parameter enhances the responsiveness of the observer. Mean Absolute Error (MAE) is utilized as an error metric to evaluate the performance of the observer and assess the impact of the α parameter.

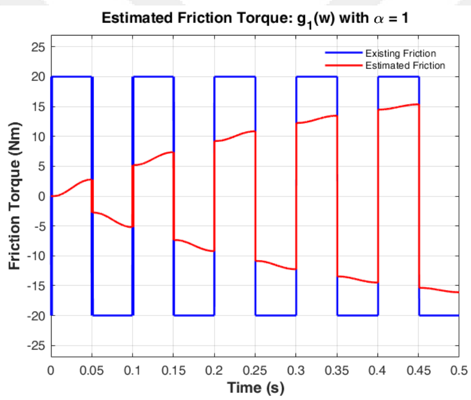

(a) Friction torques for $\alpha = 1$

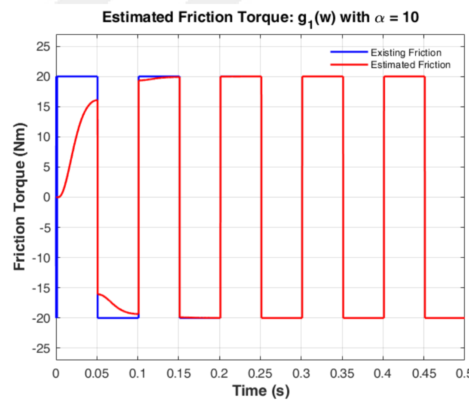

(b) Friction torques for $\alpha = 10$

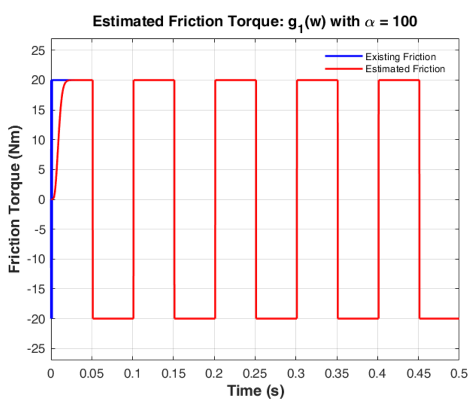

(c) Friction torques for $\alpha = 100$

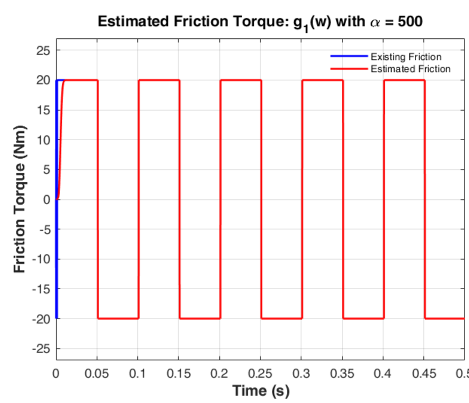

(d) Friction torques for $\alpha = 500$

Figure 2.5: Existing and estimated friction torques for 10 Hz sine wave input with different α parameters of $g_1(w)$

Table 2.2: Mean Absolute Error (MAE) of angular velocities and friction torques for different α values

Mean Absolute Error	$\alpha = 0$ (no comp.)	$\alpha = 1$	$\alpha = 10$	$\alpha = 100$	$\alpha = 500$
Angular velocity (deg/s)	0.1275	0.0733	0.0515	0.0486	0.0475
Friction torque (Nm)	19.99	10.11	1.35	0.38	0.23

The Mean Absolute Error (MAE) on angular velocity and estimated friction torques are presented in Table 2.2. The reduction in angular velocity error between the case without compensation and the case where $\alpha = 1$ is the largest among all cases with 42.51%. The primary reason for this significant reduction in error is the mitigation of the stick-slip behavior due to the presence of the CFP observer. It is also observed that changing α parameter from 1 to 10 results in a dramatic reduction in estimated friction error with 86.65%. Figure 2.5 (a) and (b) also illustrate this effect. With $\alpha = 10$, the observer manages to capture the friction characteristics significantly better and it converges to the actual friction in less than 0.2 seconds. Whereas with $\alpha = 1$, the simulation time is not sufficient for the observer to converge to the true value. According to the results, we can infer that the proposed CFP observer with the nonlinear function defined in (2.28), manages to minimize the undesirable effects of friction by eliminating stick-slip motion and enhancing the tracking performance. The parameter α also improves the system's tracking performance by reducing the estimator's settling time. However, if α is considered as the observer's gain, there is a limit to increasing α as it may lead to system instability. An optimal value for this parameter can be determined, which will be discussed in the subsequent chapters. The nominal input u_n for the system shown in Figure 2.3 is also depicted in Figure 2.6 to analyze the impact of increasing α values on the input to the plant. As α increases, the overshoot in u_n becomes more pronounced, with a percent overshoot of 17% observed for $\alpha = 500$. Notably, u_n does not grow excessively large even for high α values. This observation is critical, as although the system may estimate friction accurately, excessively large inputs could render the system impractical for real-life applications due to actuator limitations.

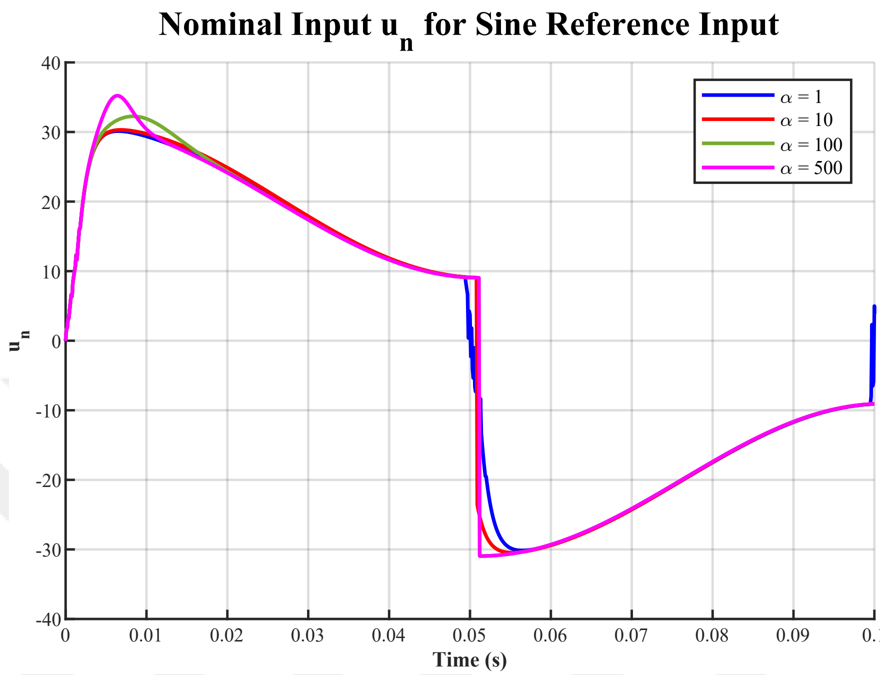

Figure 2.6: Nominal input u_n for different α values

We will now analyze the friction compensation performance of CFP observer in the same manner with $g_2(w)$ function defined in (2.29). As in $g_1(w)$, there is only one parameter in $g_2(w)$ notated as α. The simulation time, the reference input and the simulation parameters in Table 2.1 remain unchanged. The estimated friction torques for four different α values are presented in Figure 2.7. The system output and estimation errors are presented in Table 2.1. The angular velocity response of the system is similar to Figure 2.4, therefore it is provided in Appendix Figure A.2. By observing the error values and friction torques in Figure 2.7 and Table 2.1, respectively, one can state that with the same values of α, better estimation is obtained by using $g_2(w)$ compared to $g_1(w)$. Due to the absolute value of the angular velocity in the definition of $g_2(w)$, the convergence occurs faster. The MAE for angular velocity also decreases by 4%. However, regardless of the type of the nonlinearity in observer, the tracking performance with the compensator remains sufficiently robust to observe this improvement visually. From Figure 2.7 (d), it is observed that the estimator begins to overshoot the desired value. The responsiveness of the observer gradually improves as α is set to 500. However, this adjustment results in overshoot in the friction estimation.

Selecting an appropriate value for the observer parameter involves a design trade-off between convergence time and maximum overshoot.

Lastly, the friction compensation method with CFP observer is simulated with $g_3(w)$ function defined in (2.30). All variables remain unchanged since the simulations that are performed by using the other two functions. One extra parameter λ is considered due to tangent hyperbolic (tanh) function in $g_3(w)$. The λ parameter affects the steepness of the 'tanh' function. As λ increases, the function becomes steeper. The estimated friction torques and Mean Absolute Errors (MAE) for different α and λ values are presented in Figure 2.8 and Table 2.4, respectively. The angular velocity response of the system is provided in Appendix Figure A.3.

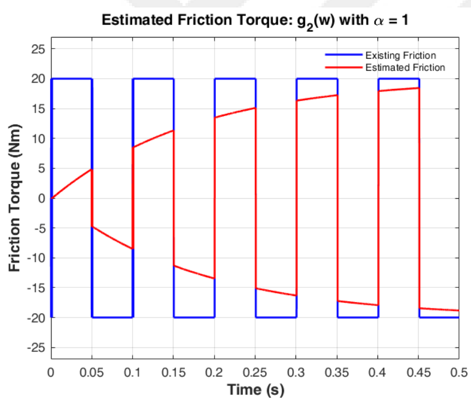

(a) Friction torques for $\alpha = 1$

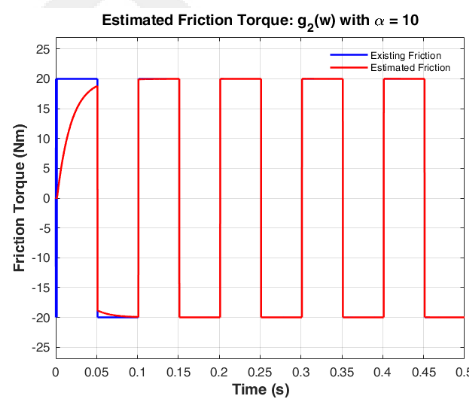

(b) Friction torques for $\alpha = 10$

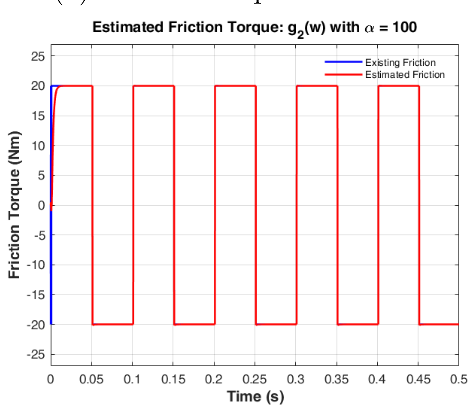

(c) Friction torques for $\alpha = 100$

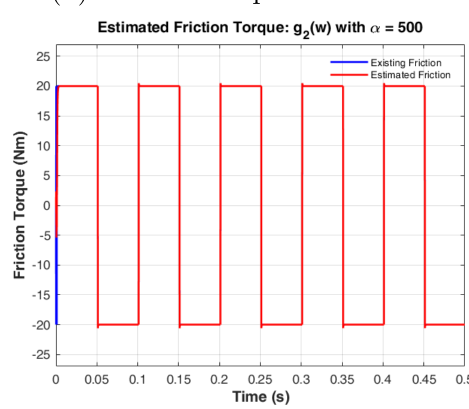

(d) Friction torques for $\alpha = 500$

Figure 2.7: Existing and estimated friction torques for 10 Hz sine wave input with different α parameters of $g_2(w)$

Table 2.3: Mean Absolute Error (MAE) of angular velocities and friction torques for different α values

Mean Absolute Error	$\alpha = 0$ (no comp.)	$\alpha = 1$	$\alpha = 10$	$\alpha = 100$	$\alpha = 500$
Angular velocity (deg/s)	0.1275	0.0623	0.0495	0.0469	0.0465
Friction torque (Nm)	19.99	6.72	0.76	0.13	0.07

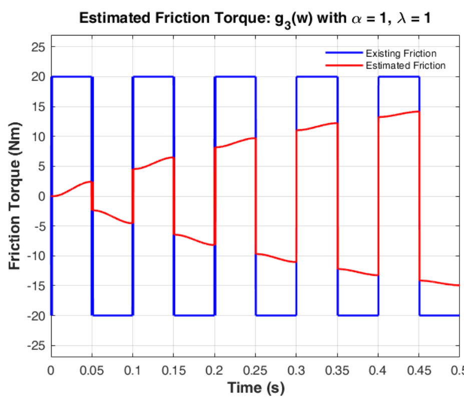

(a) Friction torques for $\alpha = 1$, $\lambda = 1$

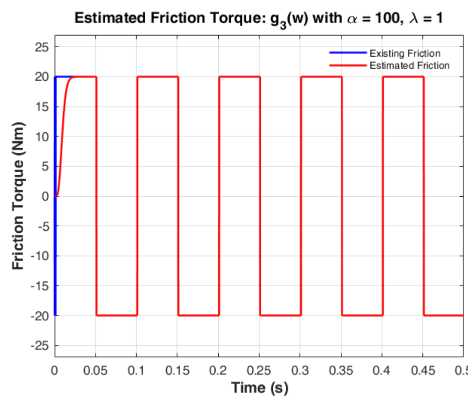

(b) Friction torques for $\alpha = 100$, $\lambda = 1$

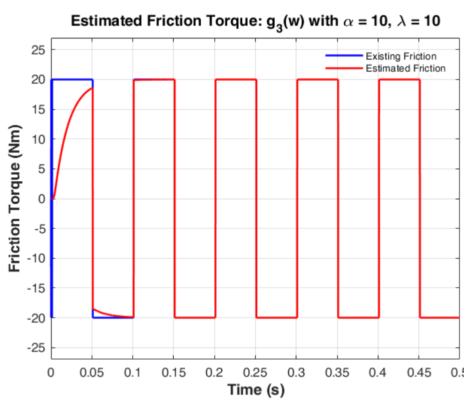

(c) Friction torques for $\alpha = 10$, $\lambda = 10$

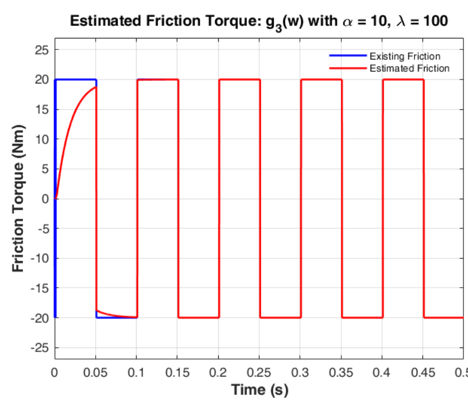

(d) Friction torques for $\alpha = 10$, $\lambda = 100$

Figure 2.8: Existing and estimated friction torques for 10 Hz sine wave input with different α and λ parameters of $g_3(w)$

To observe the individual effects of the parameters on friction compensation, one of the parameters is held constant while the other is altered. By comparing the errors in Table 2.3 and in Table 2.4, it can be deduced that the estimation converges faster using $g_2(w)$ than using $g_3(w)$ if λ parameter is neglected, i.e.

Table 2.4: Mean Absolute Error (MAE) of angular velocities and friction torques for different α and λ values

Mean Absolute Error	$\alpha = 0$ $\lambda = 0$ (no comp)	$\alpha = 1$ $\lambda = 1$	$\alpha = 100$ $\lambda = 1$	$\alpha = 10$ $\lambda = 10$	$\alpha = 10$ $\lambda = 100$
Angular velocity (deg/s)	0.1275	0.0768	0.0486	0.05	0.0496
Friction torque (Nm)	19.99	11.07	0.39	0.86	0.79

$\lambda = 1$. For larger λ values, 'tanh' function approaches to 'signum' function and therefore $g_3'(w)$ to $g_2'(w)$. This can also be observed from the case where $\alpha = 10$ and $\lambda = 100$. The angular velocity and friction torque errors for this case are 0.0496 deg/s and 0.79 Nm, respectively. We can observe that for $\alpha = 10$ in Table 2.3, the angular velocity and friction torque errors are 0.0495 deg/s and 0.76 Nm, respectively. This is approximately the same errors in the case where λ is chosen sufficiently large in $g_3(w)$. Hence, for greater λ, $g_2(w)$ and $g_3(w)$ behave similarly, as expected.

To summarize, the effect of using different nonlinear functions in CFP observer on friction compensation are investigated in this subchapter. It can be concluded that using $g_2(w)$ defined in (2.29), leads to the most efficient observer design. It achieves the tracking performance and convergence rate of other functions with lower gains. The focus of this study is to compensate for the friction, particularly during zero-velocity transitions. It is difficult to assert that one function performs better than the other in this aspect, as both functions behave similarly in regions where the velocity approaches zero. This feature of the functions is illustrated in Figure 2.9. The outputs of the functions are close to each other and approach zero when the velocity is near zero. This corresponds to the condition where the observer, according to (2.12), has its maximum influence on the estimation of Coulomb friction. Due to the similar outputs of these three functions during velocity reversals, it is challenging to draw conclusions about the nonlinear function's impact on stick-slip behavior.

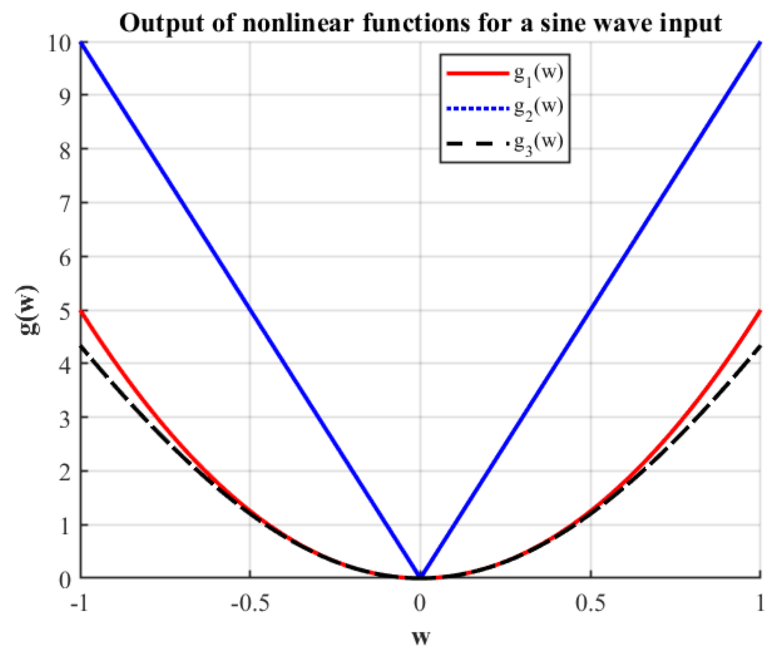

Figure 2.9: Output of nonlinear functions with respect to angular velocity for $\alpha = 10$ and $\lambda = 1$

2.2 Case 2: Friction Compensation Using the Modified Friedland-Park (MFP) Observer

In this chapter, the Modified Friedland-Park (MFP) observer is introduced. The MFP observer shares similarities with the CFP observer discussed in Section 2.1, differing slightly in observer structure. In the CFP observer, we assumed that the Coulomb friction, k is unknown, while the viscous damping coefficient, b is known. The same assumption holds for the MFP case; however, in the CFP scenario, b was perfectly known and thus canceled out. In the MFP case, instead of canceling b, we will include it in the observer state equations. This approach will allow us to analyze the observer's friction compensation performance under these conditions. Since the effects of utilizing different nonlinear functions in the observer are discussed in Section 2.1, this section will focus specifically on the functionality of the MFP observer. We will begin by governing the system and observer state equations. Let $\hat{k}$ denote the estimate of k. Accordingly, the expression for u_n and the differential equation that describes the system model, respectively, are

$$u_n = u + \hat{k}\,\mathrm{sign}(w) \tag{2.31}$$

$$J\dot{w} = u - k\,\mathrm{sign}(w) + \hat{k}\,\mathrm{sign}(w) - bw. \tag{2.32}$$

Notice the viscous damping term in (2.32), which is omitted in (2.10) as part of the CFP observer definition. The observer state equations are also as follows:

$$\dot{z} = \frac{(u - bw)}{J} g'(w) \tag{2.33}$$

$$\hat{k} = z - g(w), \tag{2.34}$$

where z represents the state of the observer and $g(w)$ is an appropriate nonlinear function defined as $g(\cdot) : \mathbb{R} \to \mathbb{R}$. The state of the observer in (2.33) depends directly on angular velocity in MFP observer due to viscous damping term. The error dynamics of the estimation is therefore

$$e_k = k - \hat{k} \tag{2.35}$$

$$\dot{e}_k = -\dot{\hat{k}} = -\dot{z} + g'(w)w'. \tag{2.36}$$

Substituting $\dot{z}$ in (2.33) and $\dot{w}$ in (2.32) into (2.36), yields

$$\dot{e_k} = -\frac{u}{J} g'(w) + bwg'(w) - g'(w)\,\mathrm{sign}(w)\frac{e_k}{J} - bwg'(w) + \frac{u}{J} g'(w). \tag{2.37}$$

By canceling the terms with opposite sign, we obtain

$$\dot{e_k} = -g'(w)\,\mathrm{sign}(w)\frac{e_k}{J}. \tag{2.38}$$

The error dynamics equation for the MFP observer in (2.38) is identical to that of the CFP observer in (2.16). The nonlinear function defined in (2.29) is used in MFP observer. The system model with MFP observer is illustrated in Figure 2.10. The parameters used in simulating this system are provided in Table 2.1.

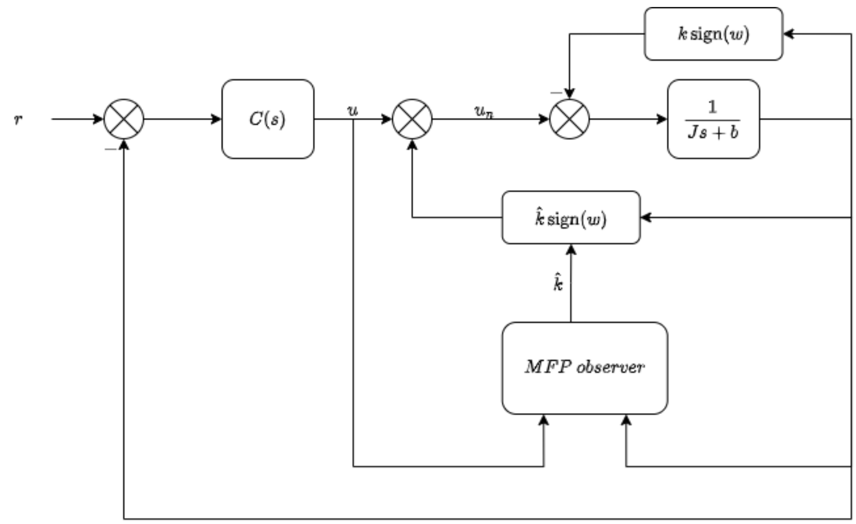

Figure 2.10: System model with MFP observer

Table 2.5: Simulation Parameters for Case 2

Parameter	Value	Unit
Moment of inertia (J)	10	kgm^2
Coulomb friction (k)	20	Nm
Viscous damping coefficient (b)	2	$Nm \cdot s/rad$
Proportional controller gain (k_p)	150	
Integral controller gain (k_i)	200	
Sampling time	0.0001	sec
α in $g_2(w)$	10	

The reference input is 10 Hz sine wave with an amplitude of 1 deg/s. The angular velocity response is presented in Figure 2.5.

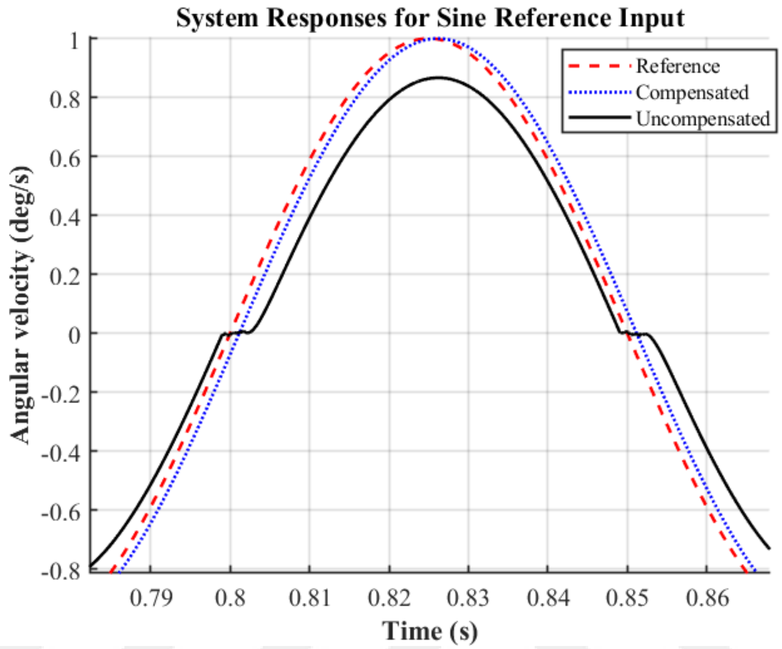

Figure 2.11: Angular velocity responses of the system with and without friction compensation

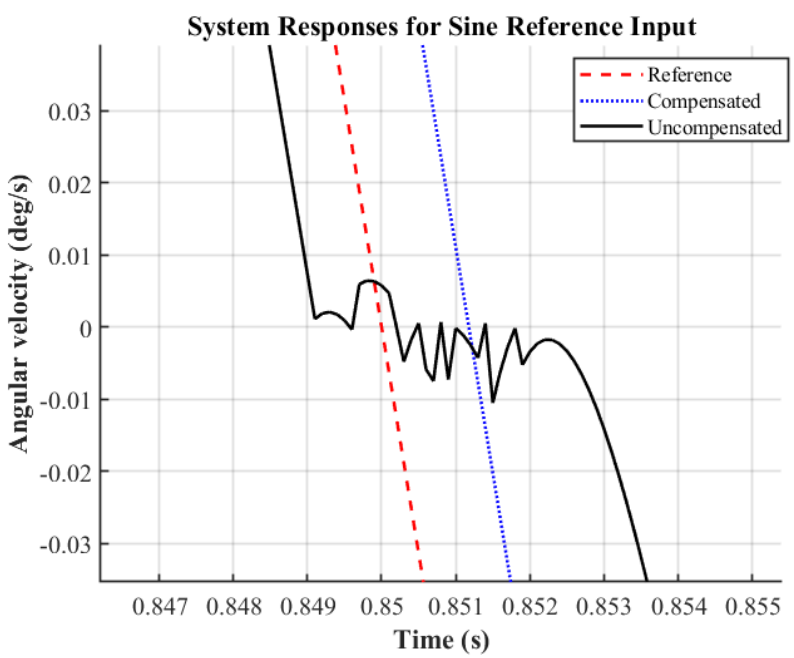

Figure 2.12: Zoomed in version of Figure 2.11

Based on the simulation results, it can be concluded that the MFP observer successfully compensates for friction. Similar to the CFP observer, it eliminates oscillations near zero velocity, resulting in improved tracking performance. Since the error dynamics of CFP and MFP are identical, it is not possible to observe whether there is an improvement in compensation accuracy compared to the CFP observer. The MAE for angular velocity is 0.0472 deg/s and for friction estimation it is 0.19 Nm which are exactly the same provided in Table 2.3. The standard deviations of angular velocity in both observer designs are nearly the same with 0.7 deg/s. Hence, we can conclude that regardless of including viscous damping coefficient in observer structure, the Friedland-Park observer successfully compensates for friction. The sinusoidal tracking responses for different α parameters are also presented in Appendix A.4. The Figure 2.13 below shows the system responses with and without friction compensation with MFP for a chirp reference input. The chirp signal sweeps the frequencies between 1 Hz to 100 Hz.

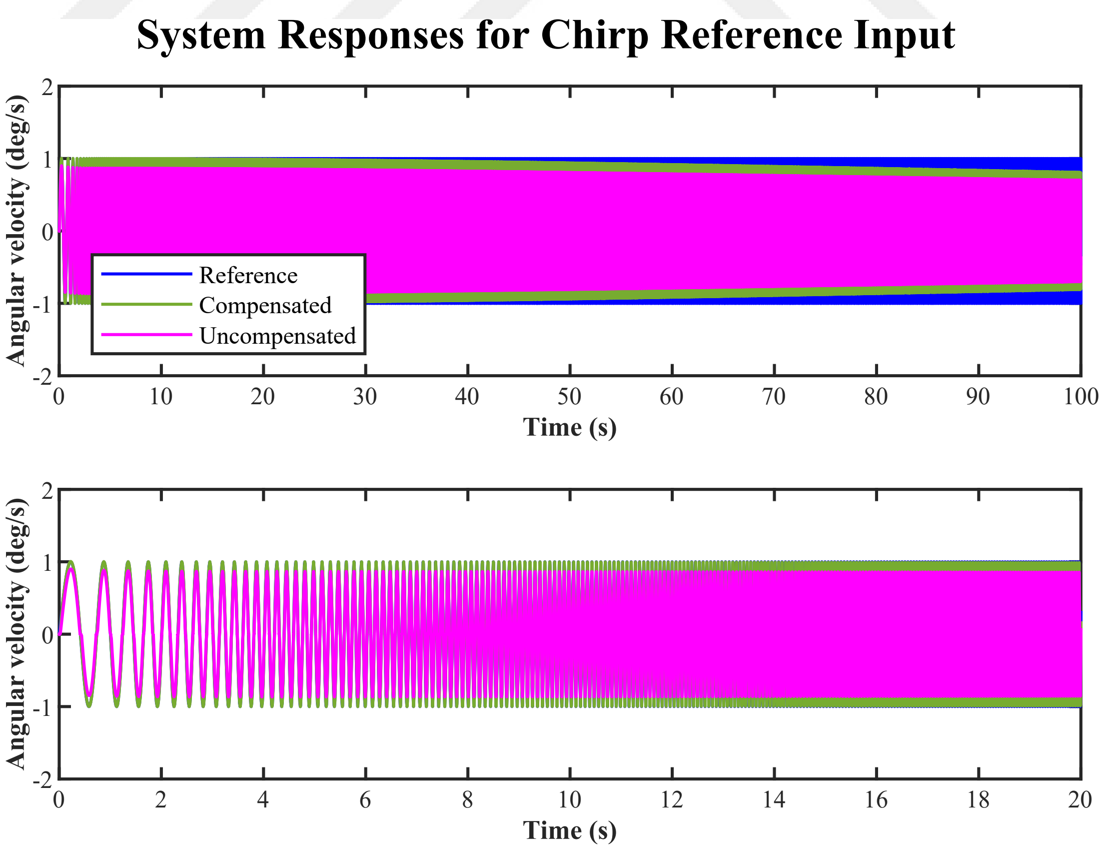

Figure 2.13: Angular velocity responses of the system with and without friction compensation for chirp reference input

From the bottom graph of Figure 2.13, the friction compensated signal tracks the reference input up to 20 Hz without any delays however the uncompensated signal cannot track the reference even for low frequency inputs. After certain frequencies, the bandwidth of the friction compensated case becomes not sufficient, too, due to damping effects of friction. It is known that the stick-slip motion limits the system's ability to respond to high-frequency inputs effectively. With friction compensation, one can observe that the system responds more dynamically to input signals, improving its bandwidth. The MFP observer therefore, helps the system to maintain consistent performance across a wider frequency range by compensating the nonlinear effects of friction.

2.3 Case 3: Friction Compensation Using the Novel Friedland-Park (NFP) Observer

In this section, Novel Friedland-Park (NFP) observer is proposed. Unlike classical and modified Friedland-Park observers, the NFP observer assumes that the Coulomb friction, k, is known and aims to estimate the viscous damping coefficient, b. In this case, the formulation of the system dynamics and observer state equations is performed by neglecting the Coulomb friction since it is perfectly known and can be canceled out. First, the system and observer state equations are derived. Let $\hat{b}$ denote the estimate of b. Thus, the expression for the nominal input u_n and the differential equation that describes the system model, respectively defined as

$$u_n = u + \hat{b}w \tag{2.39}$$

$$J\dot{w} = u - bw + \hat{b}w. \tag{2.40}$$

The structure of the observer state equations are similar to CFP and MFP where the observer internal state variable depends on the input u multiplied by a nonlinear function of angular velocity. The nonlinear function presented in (2.29) is utilized once more. The observer equations are as follows:

$$\dot{z} = \frac{u}{J}g'(w) \tag{2.41}$$

$$\hat{b} = z - g(w). \tag{2.42}$$

where z represents the state of the observer and $g(w)$ is an appropriate nonlinear function defined as $g(\cdot) : \mathbb{R} \rightarrow \mathbb{R}$. Accordingly, the error dynamics can be derived as

$$e_b = b - \hat{b} \tag{2.43}$$

$$\dot{e}_b = -\dot{\hat{b}} = -\dot{z} + g'(w)w'. \tag{2.44}$$

Substituting $\dot{z}$ in (2.41) and $\dot{w}$ in (2.40) into (2.44) yields

$$\dot{e}_b = -\frac{u}{J}g'(w) - wg'(w)\frac{e_b}{J} + \frac{u}{J}g'(w). \tag{2.45}$$

By canceling the terms with opposite sign, we obtain

$$\dot{e}_b = -wg'(w)\frac{e_b}{J}. \tag{2.46}$$

Hence, by utilizing the function defined in (2.29), the error dynamics become

$$\dot{e}_b = -w\alpha \,\mathrm{sign}(w)\frac{e_b}{J}. \tag{2.47}$$

The system model with NFP observer is shown in Figure 2.14. The parameters used in simulation are also provided in Table 2.6.

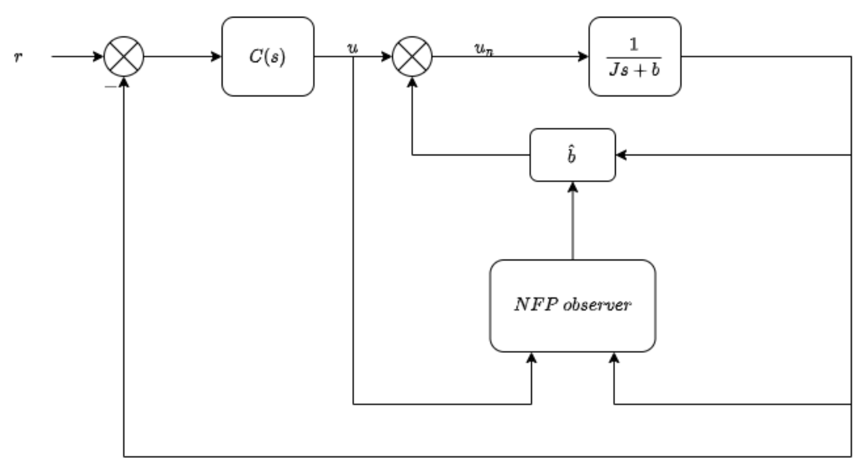

Figure 2.14: System model with NFP observer

Since the Coulomb friction is neglected, the problem is simplified to an estimation problem of viscous coefficient. Hence, the estimation results for different

Table 2.6: Simulation Parameters for Case 3

Parameter	Value	Unit
Moment of inertia (J)	10	kgm^2
Viscous damping coefficient (b)	10	$Nm \cdot s/rad$
Proportional controller gain (k_p)	150	
Integral controller gain (k_i)	200	
Sampling time	0.0001	sec

α values of $g_2(w)$ are presented in Figure 2.15. The true value of the viscous coefficient is selected as 10 $Nm \cdot s/rad$ to have a clearer observation of its influence besides Coulomb friction in Figure 2.16. The reference input is a 1 Hz sine wave with an amplitude of 1 deg/s and the simulation time is 2 seconds.

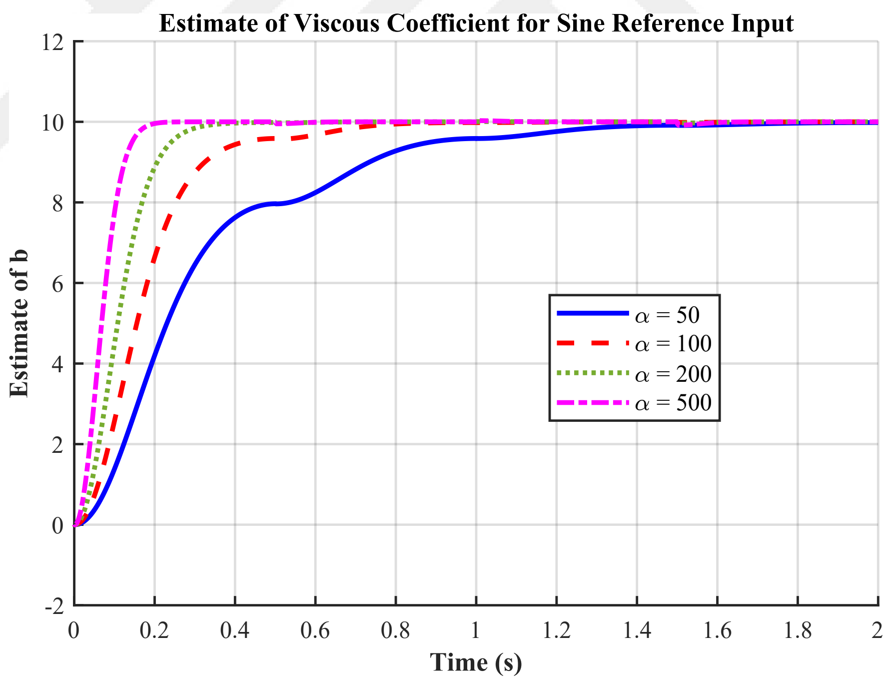

Figure 2.15: Estimation of viscous coefficient (b) for different α values

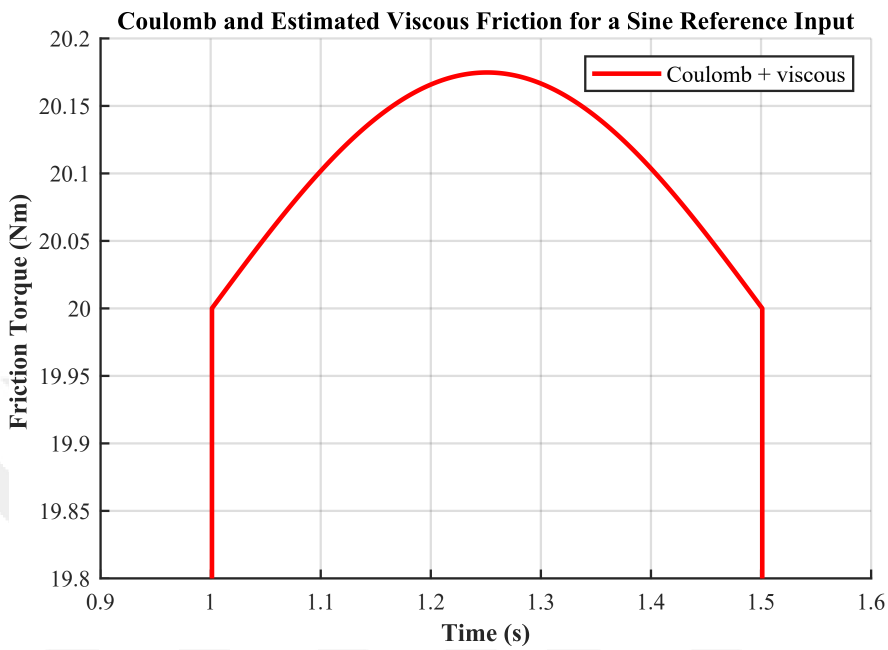

Figure 2.16: Estimated viscous friction effect on top of Coulomb friction

According to 2.15, viscous coefficient parameter is estimated using NFP observer. The variation of the estimation with respect to the gain parameter of the observer, α, are provided, too. As in Case 1 and Case 2 where the goal is to estimate the Coulomb friction, α parameter affects the convergence time of the estimation. Increasing α, reduces the time of convergence, however for some value of α, spikes in estimation occurs due to improver tuning of the observer gain which causes the observer to overreact against measurement errors. The parameter should be selected carefully to ensure the balance between convergence speed and robustness. The sinusoidal tracking responses are also provided in Appendix A.5. This simulation study demonstrates that the viscous friction coefficient can be estimated using the NFP observer. Additionally, for the proposed system, we showed that this parameter can be expressed as a pole of the plant. Considering the plant of the feedback system depicted in Figure 2.14, we estimated the plant's pole under the assumption that J is known. Thus, the NFP observer can also be evaluated within the framework of system identification as in [32] where a deadbeat observer is proposed for system identification. By integrating the modeled friction or any other disturbance effect to the system plant, one can achieve the estimation of the system plant. This proposed structure can be employed for grey-box system modeling. The grey-box modeling approach uses the known physical relationships to formulate the system model and estimate the unknown parameters using system identification methods. To illustrate, [33] implements a grey-box modeling approach to model a rotating arm where the mechanical model is known however friction is unknown and inertia is left to be estimated. Overall, as a system identification method, NFP observer is utilized considering the study presented in this chapter. The plant model is a single rotational mass with a moment of inertia J and an unknown pole b. By estimating b, the approach known in the literature as grey-box modeling is performed.

Chapter 3

Friction Compensation of High-order Systems

The effects of friction tend to be more pronounced in high-order systems, which are often more sensitive to nonlinearities. Even small disturbances can amplify oscillations, causing system instability. Moreover, friction-induced stick-slip motion can interfere with the system's intrinsic damping properties, potentially leading to resonance or instability. Consequently, this chapter investigates friction compensation in inertial mechanical systems, with a particular emphasis on its application to high-order systems. This focus seeks to offer a realistic and comprehensive approach to addressing the complexities and challenges posed by friction in such systems.

3.1 High-order System Model

In system modeling, lumped systems refer to systems where physical properties (e.g., mass, stiffness, damping) are assumed to be concentrated at discrete points rather than distributed continuously over space [34]. Considering the system model used in earlier chapters, the moment of inertia J is lumped at the load position, meaning the entire dynamics of the system is concentrated at this point. In this model, complexities such as motor inertia, stiffness, and damping are neglected in terms of simplicity. Instead, these dynamics are represented as an equivalent inertia on the load side. Higher-order system models are frequently preferred against low-order lumped systems to accurately capture the dynamics of real-world mechanical systems. Hence, a two-mass model that is coupled with a spring is employed. The schematic representation of the model is provided in Figure 3.1. The notation used within the model is also presented in Table 3.1 [35].

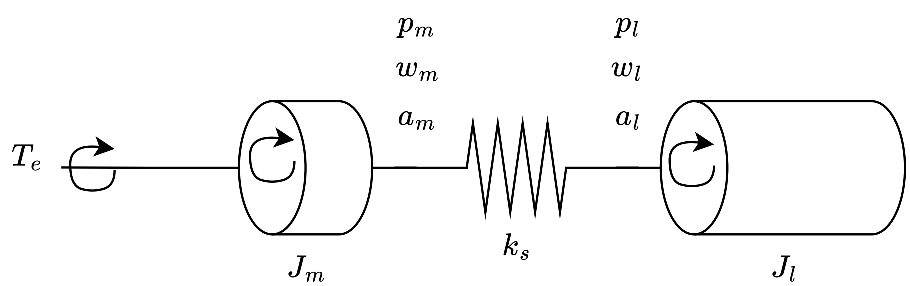

Figure 3.1: Two-mass System Model

Table 3.1: Notation of two-mass model parameters

Parameter	Notation
Electromagnetic torque	T_e
Motor inertia	J_m
Load inertia	J_l
Spring stiffness	k_s
Viscous damping	k_{cv}
Motor position	p_m
Motor velocity	w_m
Motor acceleration	a_m
Load position	p_l
Load velocity	w_l
Load acceleration	a_l

The model assumes that the current is multiplied by the motor torque constant to generate the electromagnetic torque at the motor side. The electromagnetic torque (T_e) drives the motor, resulting in the deformation of the spring which subsequently produces a torque transmitted to the load. The rotation of the load occurs as a consequence of the angular acceleration induced by the torque transmitted from the motor. Using the block diagram provided in Appendix A.1, one can express the equations of the model dynamics as in [35]. These dynamics are also employed in modeling robot manipulators with elastic joints [36]. In such models, a dynamic coupling between the actuators and the links is typically assumed [37]. The model depicted in Figure 3.1, along with its variations, is widely utilized in the literature. Relating the motor and load positions (p_m and p_l) to the electromagnetic torque (T_e) results in the formulation of the following differential equations:

$$J_m \ddot{p_m} + kcv(\dot{p_m} - \dot{p_l}) + k_s(p_m - p_l) = T_e \tag{3.1}$$

$$J_l \ddot{p_l} + kcv(\dot{p_l} - \dot{p_m}) + k_s(p_l - p_m) = 0. \tag{3.2}$$

The matrix representation of (3.1) and (3.2) are obtained as

$$\begin{bmatrix} T_e \\ 0 \end{bmatrix} = \begin{bmatrix} J_m s^2 + k_{cv}s + k_s & -k_{cv}s - k_s \\ -k_{cv}s - k_s & J_l s^2 + k_{cv}s + k_s \end{bmatrix} \begin{bmatrix} p_m \\ p_l \end{bmatrix} \tag{3.3}$$

To obtain the transfer function from T_e to p_m and p_l, the inversion of the two-by-two matrix is performed. Let M be the two-by-two matrix in (3.3).

$$\begin{bmatrix} T_e \\ 0 \end{bmatrix} = M \begin{bmatrix} p_m \\ p_l \end{bmatrix} \tag{3.4}$$

$$M = \begin{bmatrix} J_m s^2 + k_{cv}s + k_s & -k_{cv}s - k_s \\ -k_{cv}s - k_s & J_l s^2 + k_{cv}s + k_s \end{bmatrix} \tag{3.5}$$

Then, the inverse of M can be given as

$$M^{-1} = \frac{1}{(J_m + J_l)s^2} \begin{bmatrix} \frac{J_l s^2 + k_{cv}s + k_s}{\left(\frac{J_m J_l}{J_m + J_l}\right)s^2 + k_{cv}s + k_s} & \frac{k_{cv}s + k_s}{\left(\frac{J_m J_l}{J_m + J_l}\right)s^2 + k_{cv}s + k_s} \\ \frac{k_{cv}s + k_s}{\left(\frac{J_m J_l}{J_m + J_l}\right)s^2 + k_{cv}s + k_s} & \frac{J_m s^2 + k_{cv}s + k_s}{\left(\frac{J_m J_l}{J_m + J_l}\right)s^2 + k_{cv}s + k_s} \end{bmatrix} \tag{3.6}$$

Multiplying both sides in (3.6) with M^{-1} we obtain

$$M^{-1} \begin{bmatrix} T_e \\ 0 \end{bmatrix} = \begin{bmatrix} p_m \\ p_l \end{bmatrix} \tag{3.7}$$

$$\begin{bmatrix} M_{11} & M_{12} \\ M_{21} & M_{22} \end{bmatrix} \begin{bmatrix} T_e \\ 0 \end{bmatrix} = \begin{bmatrix} p_m \\ p_l \end{bmatrix} \tag{3.8}$$

$$p_m = M_{11} T_e \tag{3.9}$$

$$p_l = M_{21} T_e. \tag{3.10}$$

The corresponding transfer functions can be found as

$$\frac{p_m(s)}{T_e(s)} = M_{11} = \frac{1}{(J_m + J_l)s^2} \left\{ \frac{J_l s^2 + k_{cv} s + k_s}{\left(\frac{J_m J_l}{J_m + J_l}\right) s^2 + k_{cv} s + k_s} \right\} \tag{3.11}$$

$$\frac{p_l(s)}{T_e(s)} = M_{21} = \frac{1}{(J_m + J_l)s^2} \left\{ \frac{k_{cv} s + k_s}{\left(\frac{J_m J_l}{J_m + J_l}\right) s^2 + k_{cv} s + k_s} \right\} \tag{3.12}$$

Hence, the transfer functions from T_e to angular velocities (w_m) and (w_l) are

$$\frac{w_m(s)}{T_e(s)} = s\frac{p_m(s)}{T_e(s)} = \frac{1}{(J_m + J_l)s} \left\{ \frac{J_l s^2 + k_{cv} s + k_s}{\left(\frac{J_m J_l}{J_m + J_l}\right) s^2 + k_{cv} s + k_s} \right\} \tag{3.13}$$

$$\frac{w_l(s)}{T_e(s)} = s\frac{p_l(s)}{T_e(s)} = \frac{1}{(J_m + J_l)s} \left\{ \frac{k_{cv} s + k_s}{\left(\frac{J_m J_l}{J_m + J_l}\right) s^2 + k_{cv} s + k_s} \right\} \tag{3.14}$$

The transfer function from T_e to w_l will be used in simulations since friction compensation performance is evaluated at the load side.

The application of the friction compensation method in a two-mass system is particularly significant for evaluating its performance under the influence of resonance frequency. This frequency is determined by minimizing the denominator of (3.14), as given below:

$$f_r = \frac{1}{2\pi}\sqrt{\frac{k_s(J_l + J_m)}{J_l J_m}} Hz. \tag{3.15}$$

3.2 Friedland-Park Observer Application on High-order System

The objective of this chapter is to apply the friction compensation method outlined in the earlier chapters to the high-order system presented in Section 3.1. Prior to this, it is essential to examine the system's frequency response to assess its stability. Given the high-order nature of the system, it is particularly susceptible to excessive vibrations, which may arise from the excitation of its natural frequencies. A frequency response analysis will help mitigate these risks and ensure robust performance. The frequency response analysis conducted here will also play a crucial role in supporting the design of a controller compatible with the system's characteristics. Frequency-domain controllers are often preferred for disturbance rejection applications, particularly in high-order systems, as they facilitate the evaluation of key performance metrics such as closed-loop stability margins and bandwidth. In contrast, time-domain controller design focuses on analyzing the transient response, which is especially relevant for capturing friction-related phenomena like stick-slip motion.

To address both aspects, two distinct controllers—one in the frequency domain and the other in the time domain—are designed. The primary purpose of implementing these different controllers is to demonstrate that the effectiveness of the friction compensation scheme is independent of the controller's performance or complexity. While controllers can mitigate the adverse effects of disturbances to a certain extent, this study highlights the necessity of friction compensation regardless of the specific controller design. In the time-domain design, a PI controller is employed, as in the previous chapter where the tuning of the controller parameters are performed according to step response of the system. In contrast, a lead controller is utilized for the frequency-domain design. The lead compensator enhances the system's bandwidth by introducing phase lead, improving its dynamic performance. Additionally, it refines the transient response by reducing metrics such as overshoot and settling time. The design goals of the lead controller are provided as given below:

- Open loop crossover frequency at $w_c = 45$ Hz
- $45°$ of phase margin

The lead controller has the following transfer function:

$$G_c(s) = K_c\left(\frac{s + z_{lead}}{s + p_{lead}}\right). \tag{3.16}$$

The controller parameters in (3.16) are identified according to the design criteria provided above. The parameters are selected to closely align with real-life applications.

It is essential to determine the additional phase lead to achieve the desired phase margin. Therefore, we will compute the phase margin based on the open loop response of the system model assuming that the gain crossover frequency (w_c) is at 45 Hz. The open loop response of the system model described in 3.14 is presented in Figure 3.2. The phase reading at 45 Hz is -148°. The phase margin is therefore

$$\phi_{pm} = 180 + \angle G(j\omega_c) \tag{3.17}$$
$$= 180 - 148 \tag{3.18}$$
$$= 32° \tag{3.19}$$

According to the calculated phase margin, there should be at least 13° phase addition to satisfy the 45° phase margin. Thus, an additional phase of 15° is selected to compensate for potential imperfections in implementation. The α parameter related to the zero and pole locations of the controller are therefore

$$\alpha = \frac{1 + \sin(\phi_{add})}{1 - \sin(\phi_{add})} \tag{3.20}$$
$$= 1.7 \tag{3.21}$$

The corresponding pole and zero locations are given by

$$p = \alpha z \tag{3.22}$$
$$p = 368 \tag{3.23}$$

such that

$$\sqrt{zp} = w_c \tag{3.24}$$

$$z = 217 \tag{3.25}$$

The gain of the controller (K_c) is determined by setting the loop gain at gain crossover frequency (w_c) to 1.

$$K_c \left| \left(\frac{jw_c + z_{lead}}{jw_c + p_{lead}} \right) G(jw_c) \right| = 1 \tag{3.26}$$

By substituting the transfer function in (3.14) with $G(jw_c)$ and setting w_c to 45 Hz, one can obtain the controller gain as $K_c = 57.1$ from 3.26.

The primary objective of selecting such an aggressive lead controller is to achieve a higher bandwidth, allowing the evaluation of friction compensation performance under high-frequency input signals, too.

With the presence of the designed controller, the open loop frequency response of the system model can be reevaluated as in Figure 3.3.

Table 3.2: Two-mass model parameters

Parameter	Value	Unit
Motor inertia (J_m)	0.02	kgm^2
Load inertia (J_l)	10	kgm^2
Spring stiffness (k_s)	1000	Nm/rad
Viscous damping (k_{cv})	5	$Nm \cdot s/rad$

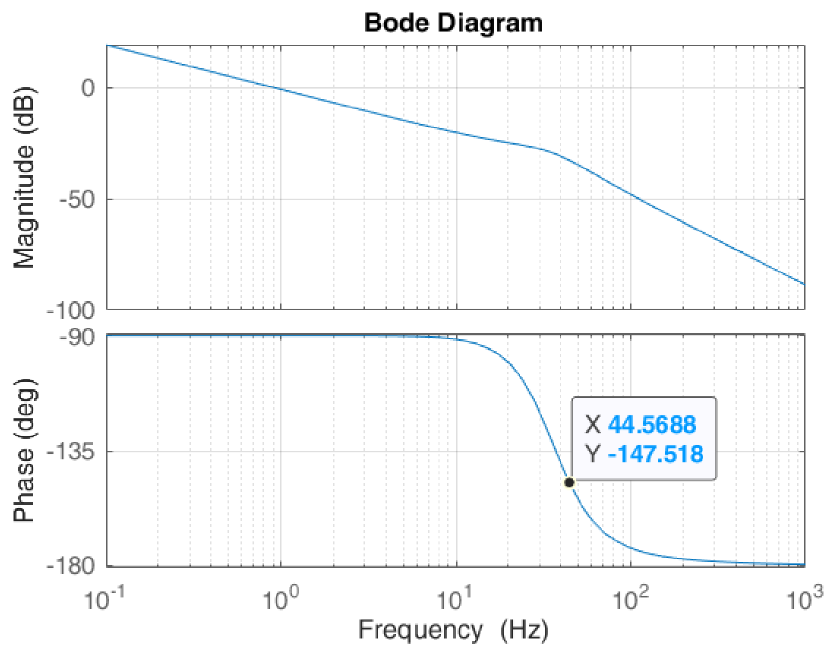

Figure 3.2: Open-loop frequency response of system model

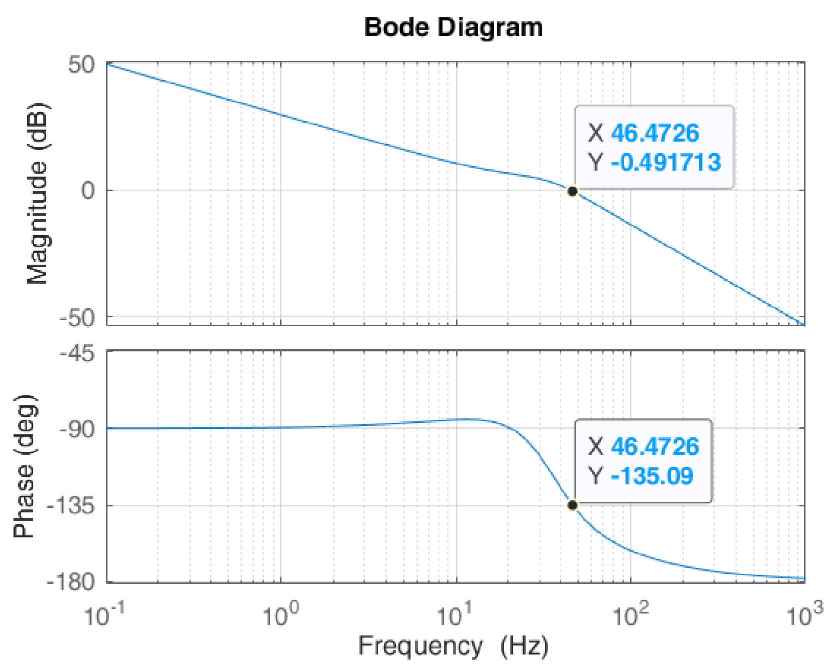

Figure 3.3: Open-loop frequency response of system model with controller

The gain crossover frequency is calculated to be 45 Hz, with a corresponding phase of $-133°$. The resulting phase margin is $47°$, meeting the design criterion. The closed loop system response is also provided in Figure 3.4 with a 3dB bandwidth of 68 Hz.

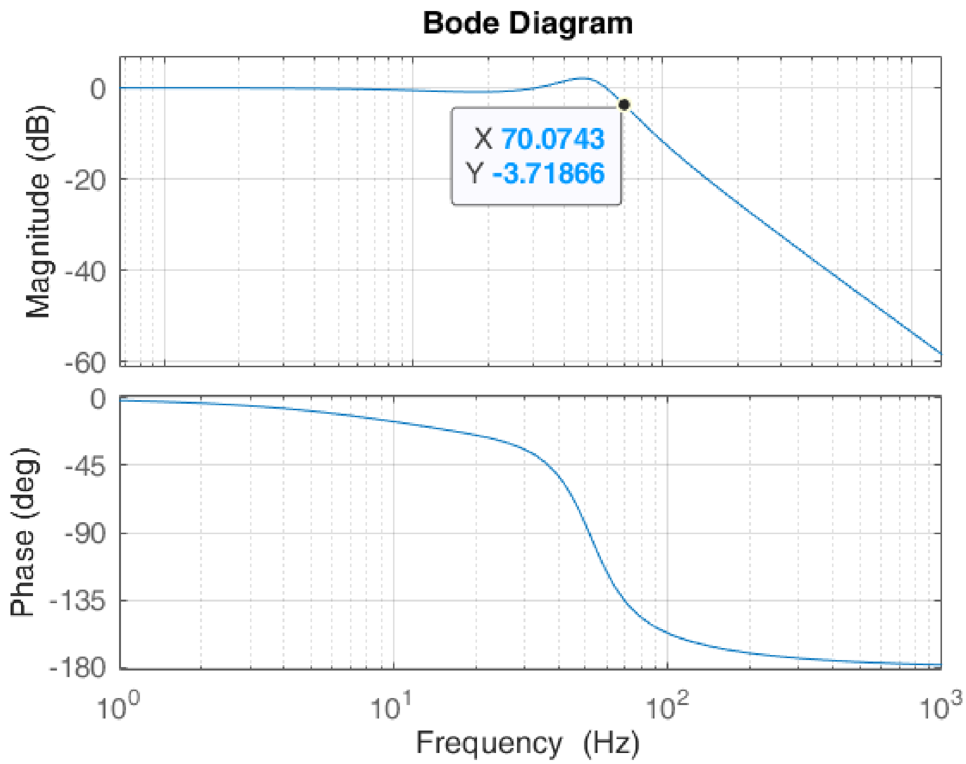

Figure 3.4: Closed-loop frequency response of the feedback system

Adapting the Friedland-Park observer structure to the described feedback system can be performed, particularly when considering the system model given in (3.14). The Friedland-Park observer structures introduced in Chapter 2 are based on a one-mass plant model that relies on a single inertia. The transfer function of the two-mass model in (3.14) is decomposed into two components:

$$P_{LO}(s) = \frac{1}{(J_m + J_l)s} \tag{3.27}$$

$$P_{HO}(s)\frac{k_{cv}s + k_s}{\left(\frac{J_m J_l}{J_m + J_l}\right)s^2 + k_{cv}s + k_s} \tag{3.28}$$

The term in (3.27) resembles the one-mass model, with the exception that the total inertia is considered in this case. The term in (3.28) represents the higher-order components of the transfer function. The Friedland-Park (FP) observer is adapted by incorporating the higher-order terms through feedforwarding them into the observer. These terms are included as part of the system input, u, which serves as the input to the system where the friction is applied. To sum up, the CFP observer introduced in Chapter 2 with the inclusion of high-order term is utilized. The overall system model is presented in below:

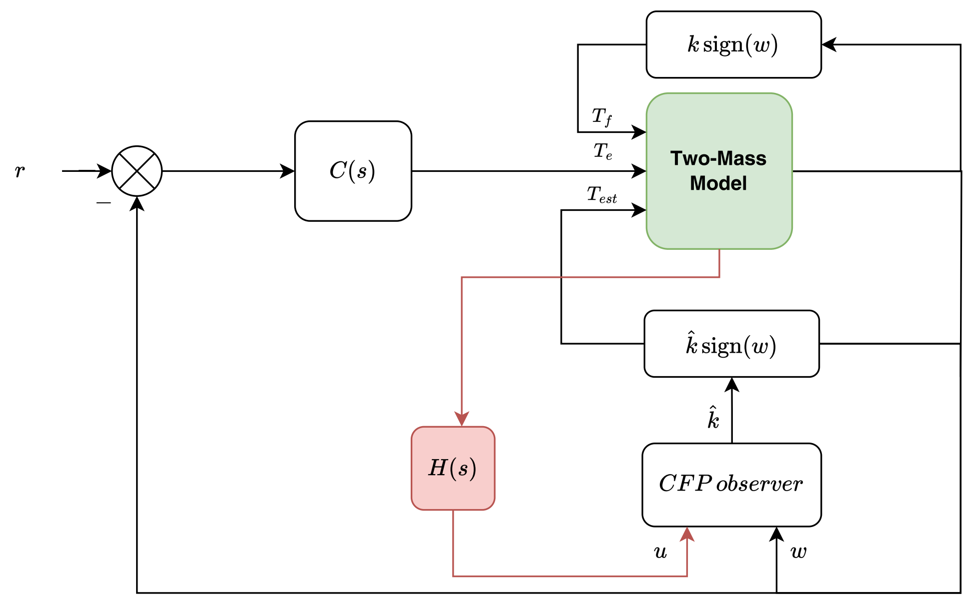

Figure 3.5: Two-mass system model with CFP observer

$H(s)$ is the high-order component of the transfer function in (3.14). The friction is applied from the load side. The input signal is therefore, the torque exerted on load. We will now present the simulations to asses the performance of the friction compensation method on a high-order system. As mentioned earlier, the system is analyzed for two different controllers. The lead controller design was explained. The performance criteria for PI controller is defined as given in below:

- Maximum percent overshoot (PO) $< 30\%$
- Settling time t_s (2% of the final value) < 0.2 seconds

The PI controller parameters are identified from the step response of the system without including friction. The step response of the system for both of the controllers are presented in Figure 3.6.

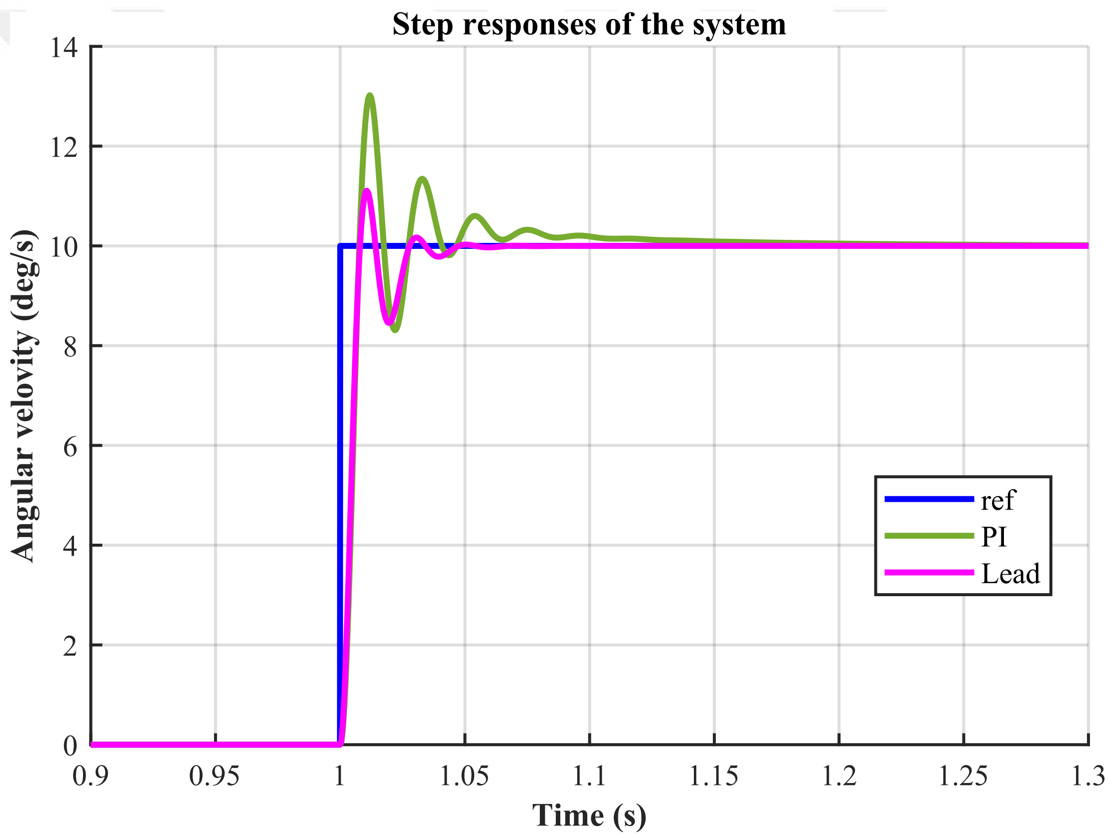

Figure 3.6: Step responses of the system for PI and lead controllers

The underlined criteria are satisfied for both of the controllers. The tuned parameters are presented in Table 3.3. The parameters of the CFP observer are also provided. The nonlinear function $g_2(w)$ described in 2.29 is utilized.

The disturbing effect of friction can be observed on top of the tuned responses of the system in Figure 3.7 and Figure 3.8 for PI and lead controllers, respectively.

Table 3.3: Simulation model parameters

Parameter	Value	Unit
Coulomb friction (k)	20	Nm
Proportional controller gain (k_p)	40	
Integral controller gain (k_i)	500	
Sampling time	0.0001	sec
α in $g_2(w)$	100	

The input is 1 Hz sine wave. The tuned response perfectly tracks the reference input. With the introduction of the friction component, stick-slip behavior emerges, causing a chattering effect near zero angular velocity. Additionally, oscillations occur following the stick and slip motion. The spring in the system transforms the energy from the slip phase into oscillatory motion. The oscillation continues until the damping dissipates the stored energy [38]. The mentioned stick-slip phenomenon in simulations does not reflect the stick-slip motion totally but it has similar behaviors. Stick-slip phenomenon occurs during transitions between static and kinetic friction torques. When the torque exceeds the static friction the system slips. In Coulomb friction model, static friction is neglected and a discontinuity is introduced in friction torque during velocity reversals. The abrupt sign change in friction torque may generate a similar phenomenon as presented in Figure 3.9. When the system velocity approaches to zero, the motion slows down due to friction which resembles the stick phase. The inertia attempts to maintain motion, causing further slipping despite the opposing friction. The spring elasticity also plays a role in slip phase since it accelerates the mass in opposite direction, creating a slip phase.

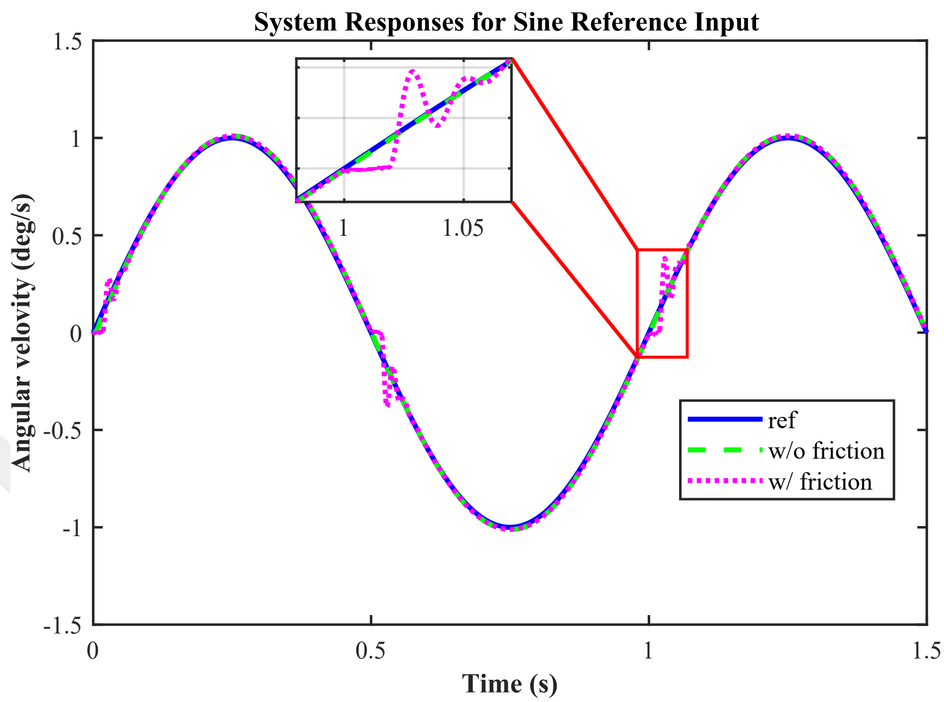

Figure 3.7: Responses of the system with PI controller for sine reference input

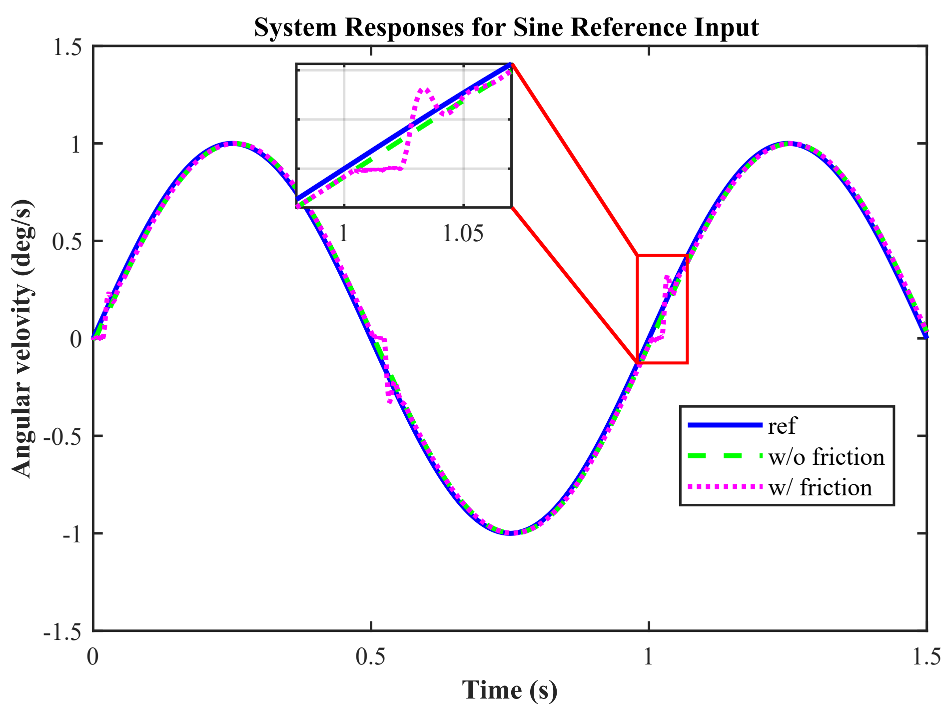

Figure 3.8: Responses of the system with lead controller for sine reference input

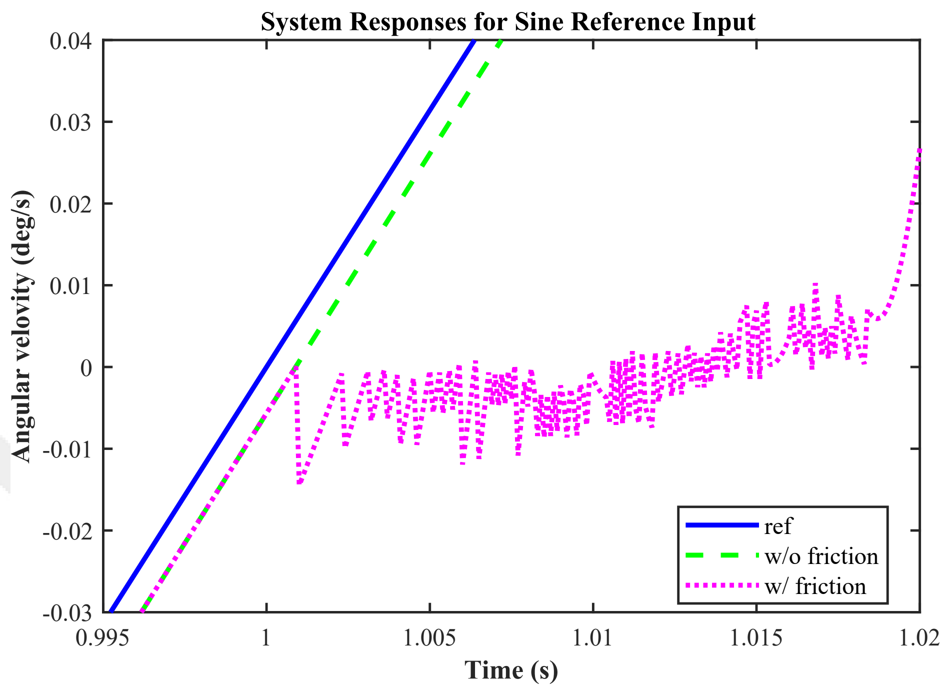

Figure 3.9: Stick-slip behavior with Coulomb friction model

The system model in Figure 3.5 is simulated without the estimator for different controllers, revealing that friction induces undesirable behavior in the angular velocity feedback, as shown in Figure 3.7 and 3.8. The PI controller amplifies the oscillations more than the system response with the lead controller. Given the poor tracking performance near zero velocity, we will now analyze the results of using a friction estimator. The angular velocity responses of the system with and without friction compensation are provided in below.

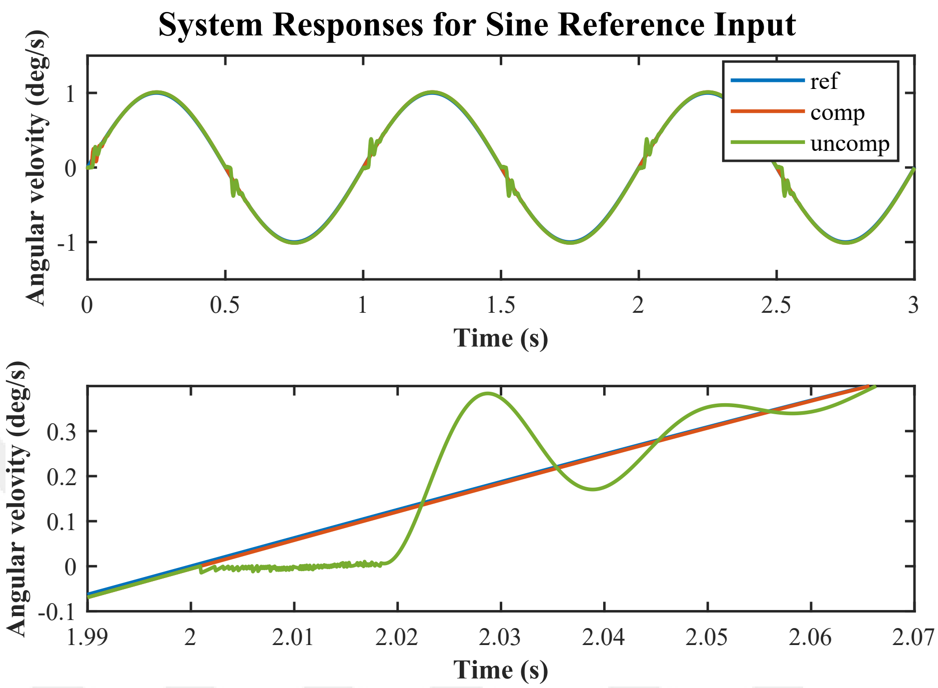

Figure 3.10: Angular velocity responses with and without friction compensation for PI controller

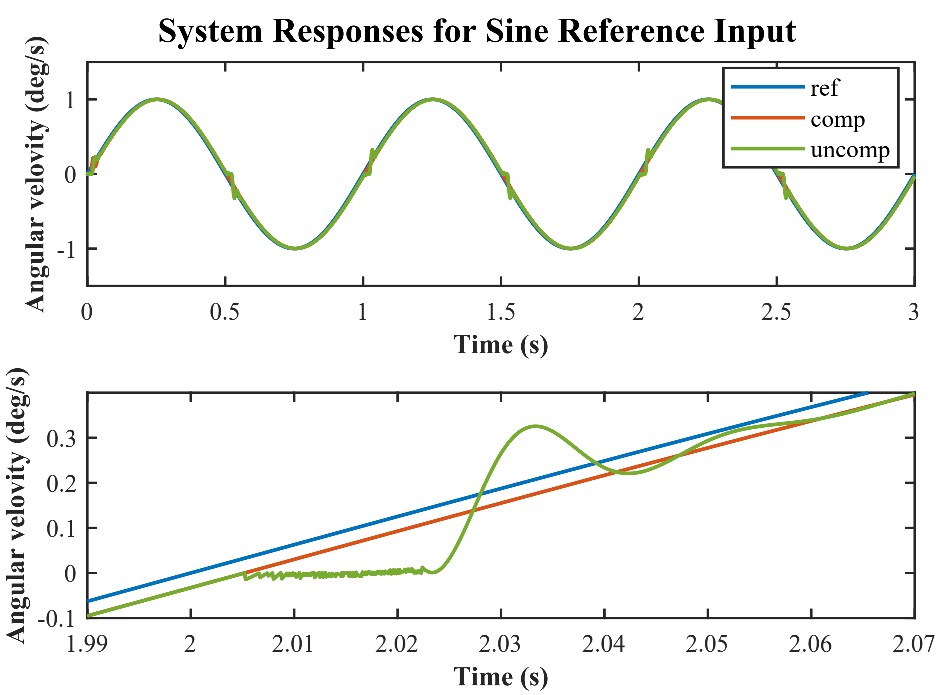

Figure 3.11: Angular velocity responses with and without friction compensation for lead controller

Based on Figures 3.10 and 3.11, the friction compensation using the CFP observer is functioning effectively for the two-mass system. It can be concluded that friction compensation is necessary regardless of the controller design. In both setups, the compensator removes the chattering during velocity sign changes and mitigates the oscillatory behavior caused by damping issues, thereby enhancing tracking performance. To evaluate the tracking performance, Root Mean Squared Error (RMSE) of gradient is employed on angular velocity. Since stick-slip motion involves sudden changes or spikes, RMSE can highlight how the friction compensation method smooths out oscillatory behavior. The rate of change may capture the unexpected variations in velocity. The errors associated to the two controller designs are provided in Table 3.4. With the presence of the friction compensator, the errors are reduced by 71.9% for both controller designs. Therefore, the friction compensation method proves to be highly effective in reducing abrupt velocity variations. To assess the high-frequency input performance of the friction compensation, a chirp input ranging from 1 to 100 Hz is applied to the system with the lead controller, as shown in Figure 3.12. The friction compensation enhances the system's responsiveness to high-frequency inputs, as seen in the chirp response. The overshoot between 40 and 60 Hz can also be observed in the closed-loop frequency response, shown in Figure 3.4. This is a consequence of the aggressive controller design. Hence, the friction compensation of a two-mass system using CFP not only enhances tracking performance but also increases the system's bandwidth.

Table 3.4: Gradient of RMSE of angular velocities

Gradient of RMSE	Comp.	Uncomp.
with PI controller (deg/s)	3.09×10^{-4}	1.1×10^{-3}
with lead controller (deg/s)	2.81×10^{-4}	1×10^{-3}

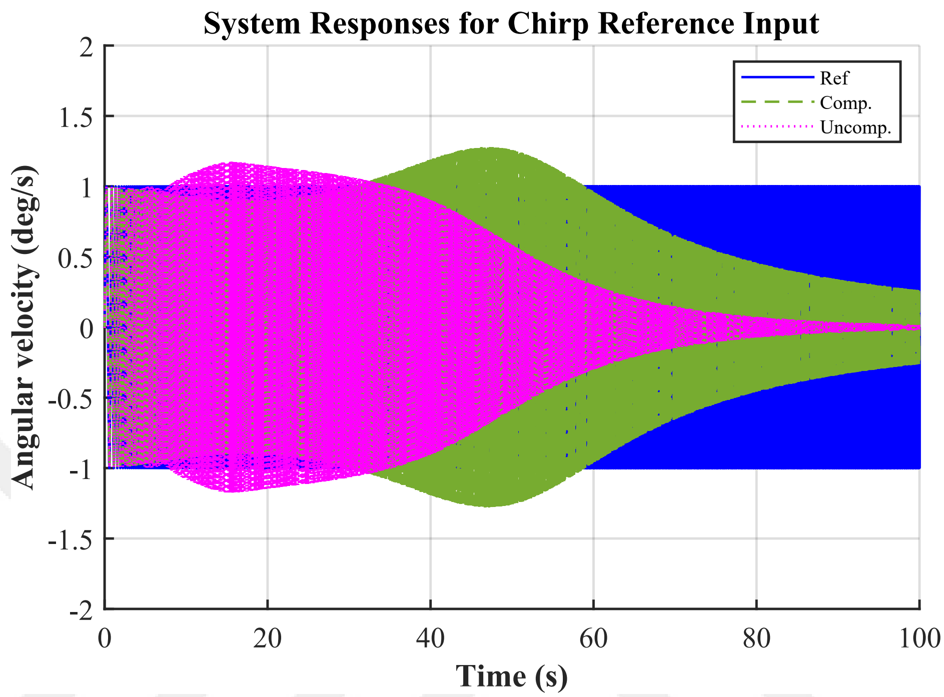

(a) Angular velocities for chirp input

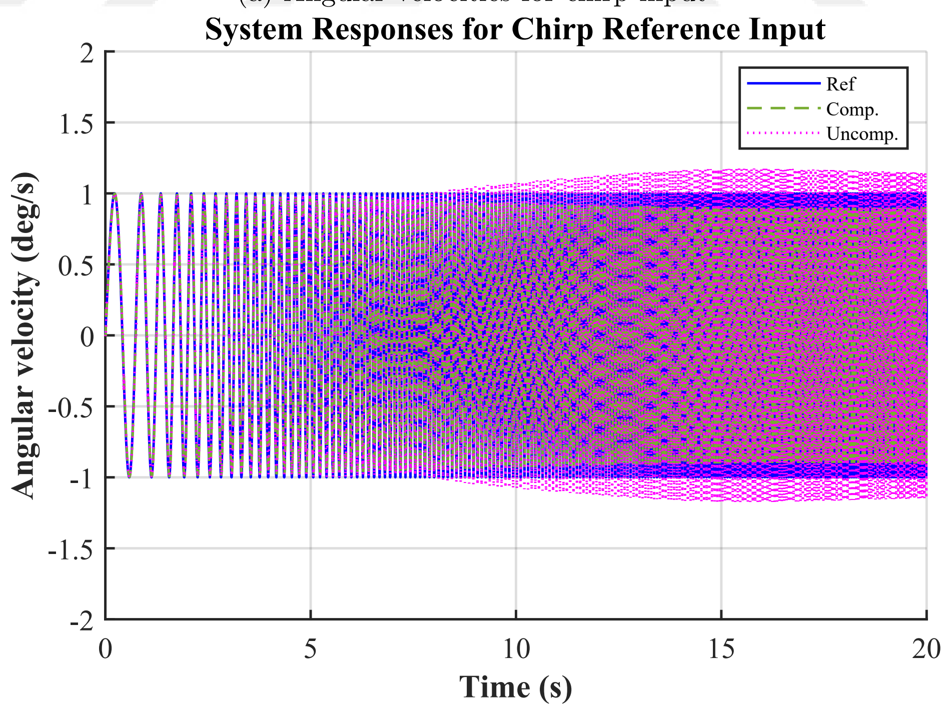

(b) Angular velocities for chirp input for a narrow time interval

Figure 3.12: Angular velocity responses of chirp reference input with and without friction compensation for lead controller

Finally, we will evaluate the position accuracy of the proposed compensation method. To achieve that, a position loop is added to the feedback system. The resulting block diagram of the system is presented in Figure 3.13.

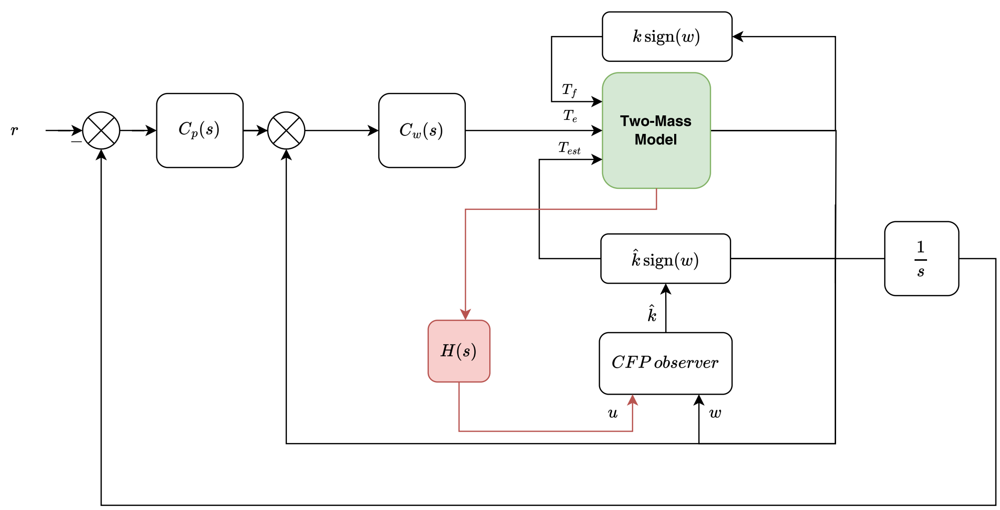

Figure 3.13: Two-mass system model with position loop

The integral term is added after the angular velocity feedback to obtain position in degrees. The position controller is defined as $G_p(s)$ which is a proportional term denoted as k_{pp}. The proportional gain is selected as $k_{pp} = 50$ according to its sine reference tracking performance. The angular position response is shown in Figure 3.14. The oscillatory behavior observed in the velocity response is reflected as a disruptive effect on position signal as depicted by the pink-colored signal in Figure 3.14. In the velocity reversal regions, the system exhibits a pausing movement where the position remains constant for 10 ms. This behavior is a result of the stick-slip phenomenon. For different systems, the duration of the motionless state may vary depending on the controller design and the system model specifications. For systems with larger inertia, this behavior becomes more dominant as the deceleration takes longer. In target tracking applications, particularly at low speeds, this friction-induced consequence in the position loop is undesirable and needs to be compensated. The proposed friction compensation scheme effectively eliminates this adverse effect.

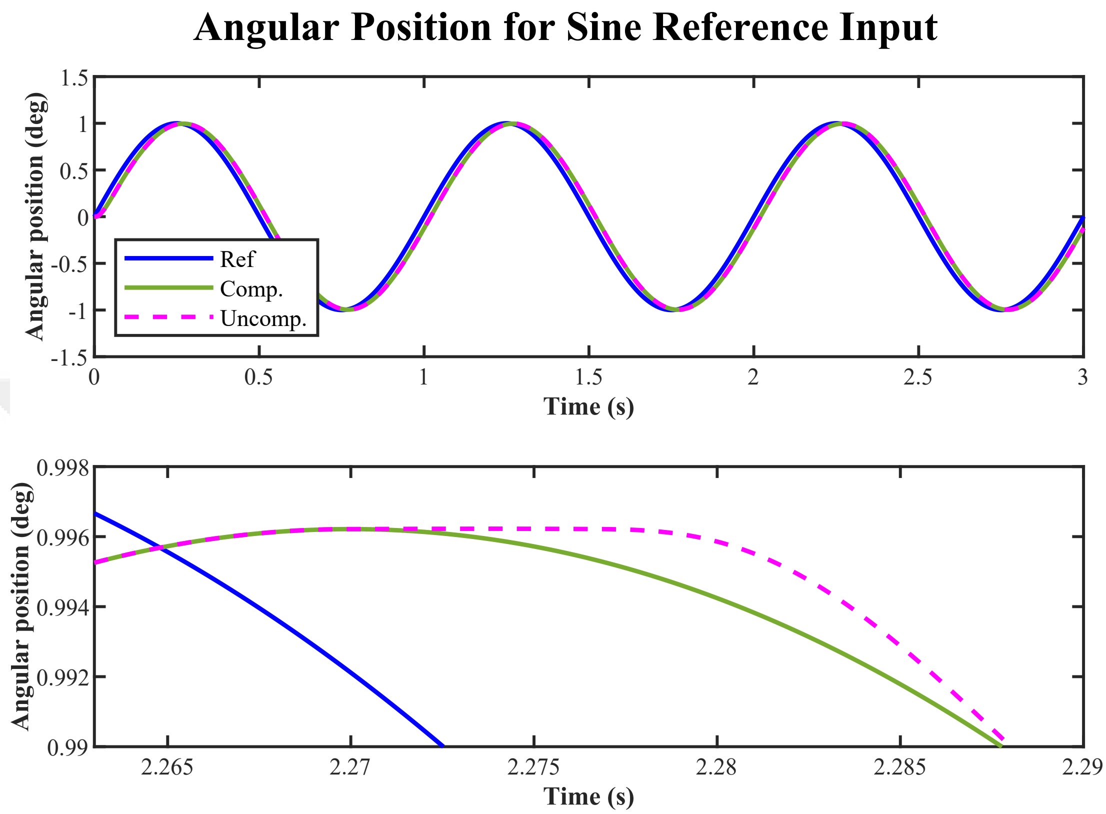

Figure 3.14: Angular position response of the system described in Figure 3.13

Chapter 4

Friction Compensation Using Extended Friedland-Park (EFP) Observer

The Coulomb friction model is characterized by two parameters: the Coulomb friction coefficient and the viscous damping coefficient. In the preceding chapters, the proposed friction compensation schemes have relied on single-parameter estimation, with the other parameter assumed to be known. This chapter introduces a two-parameter estimation approach. The Friedland-Park observer is modified to estimate both unknown parameters, leading to the development of the Extended Friedland-Park (EFP) observer.

4.1 Application of EFP Observer for Coulomb and Viscous Friction Compensation

Estimating the Coulomb and viscous frictions without relying on a dynamic friction model is advantageous for systems where the friction characteristics are difficult to model. Several observer-based approaches have been proposed in the literature to address this challenge. For instance, in [39], an asymptotic observer is designed for two-state friction dynamics, effectively compensating for nonlinear friction effects. The Extended Friedland-Park (EFP) observer achieves a similar objective, while the Classical Friedland-Park (CFP) observer specifically focuses on the estimation of the Coulomb friction coefficient. The EFP observer extends this approach by also estimating the viscous friction component. To facilitate this, an adaptive control law for two-state estimation is derived. For EFP observer-based friction compensation, the plant model is found in below. The nominal input for two-parameter estimation is

$$u_n = u + \hat{k}\,\mathrm{sign}(w) + \hat{b}w + u \tag{4.1}$$

$$J\dot{w} = u_n - k\,\mathrm{sign}(w) - bw + u. \tag{4.2}$$

Substituting u_n in (4.1) yields

$$J\dot{w} = (\hat{k} - k)\,\mathrm{sign}(w) + (\hat{b} - b)w + u \tag{4.3}$$

$$J\dot{w} = -e_k\,\mathrm{sign}(w) - e_b w + u, \tag{4.4}$$

where

$$e_k = k - \hat{k} \tag{4.5}$$

$$b_k = b - \hat{b}. \tag{4.6}$$

are the estimation errors. Using the combination of ideas discussed in previous chapters, the two-state adaptive update law related to EFP observer can be derived as follows:

$$\dot{z}_1 = g_2'(w)\frac{u}{J} \tag{4.7}$$

$$\dot{z}_2 = g_1'(w)\frac{u}{J} \tag{4.8}$$

$$\hat{k} = z_1 - g_2(w) \tag{4.9}$$

$$\hat{b} = z_2 - g_1(w). \tag{4.10}$$

where $g_1(w)$ and $g_2(w)$ are the nonlinear functions defined in (2.28) and (2.29), respectively. The error vector is therefore defined as

$$e_p = \begin{bmatrix} e_k \\ e_b \end{bmatrix} = \begin{bmatrix} k - \hat{k} \\ b - \hat{b} \end{bmatrix} \tag{4.11}$$

The error dynamics equation can be derived. The individual error dynamics equations were derived in (2.16) and in (2.46), respectively for Coulomb and viscous friction coefficients. By employing these equations, the following matrix equation is obtained:

$$\dot{e_p} = -\begin{bmatrix} g_2'(w) \\ g_1'(w) \end{bmatrix} \begin{bmatrix} \text{sign}(w) & w \end{bmatrix} e_p \tag{4.12}$$

This can be rewritten as

$$\dot{e_p} = -G(w(t))e_p, \tag{4.13}$$

where $G(.)$ is,

$$G(w(t)) = \begin{bmatrix} g_2'(w) \\ g_1'(w) \end{bmatrix} \begin{bmatrix} \text{sign}(w) & w \end{bmatrix}. \tag{4.14}$$

In single parameter estimation case, we showed that the error is asymptotically stable with a proper selection of the nonlinearity, $g(w)$. If the nonlinearity is a first or third quadrant nonlinearity, then the error converges to 0. Note that, for the error dynamics defined in (4.13), the following condition for convergence holds as described in Chapter 2 Lemma 2.

Remark 2. *Consider Lemma 2. If $w(t)$ is persistently exciting (PE), i.e.*

$$\frac{1}{T}\int_t^{t+T} G(w(t))\,dt, \tag{4.15}$$

is positive definite for some $T > 0$, $\forall t \geq 0$, then $e_p(t)$ exponentially converges to 0.

Persistent excitation is a concept for ensuring the parameter convergence in adaptive systems. A signal is said to be persistently exciting (PE) if the reference input includes frequency components equal to the number of unknown parameters [40]. This is related to the sufficient variability of the input over time. In this case, the estimation error converge exponentially to 0. In other words, if a signal is sufficiently rich, i.e. contains a broad range of frequencies, the signal is PE and therefore the convergence occurs [41]. The concept of PE is associated with ensuring convergence, meaning that parameter estimation may still converge even if the system is not PE. The friction estimation problem is therefore studied by considering the PE concept, where various reference inputs containing different frequency components are utilized. The system model to be simulated is shown in Figure 4.1.

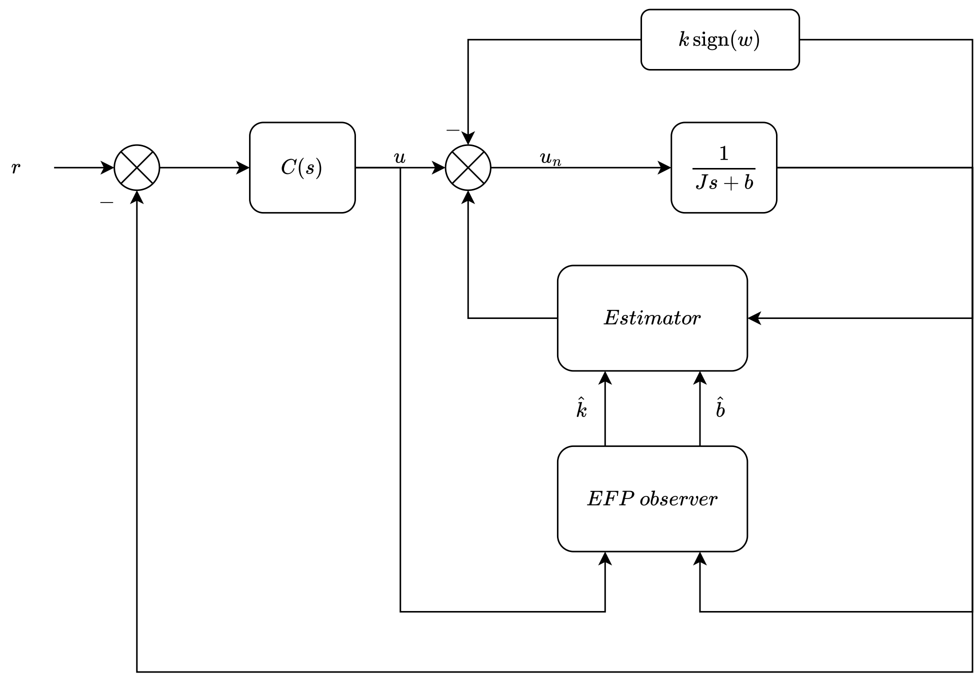

Figure 4.1: System Model with EFP observer

The EFP observer block implements the adaptive update law defined in (4.7)-(4.10). The controller $C(s)$ is a PI controller with the same parameters that are used in Chapter 2. The simulation parameters are provided in Table 4.1.

The initial values of α_2 and α_1 are set to 10. The estimation performance of the EFP observer is investigated for various combinations of the α_2 and α_1 parameters. The reference input is a 1 Hz sine wave. The estimation results are shown in Figure 4.2.

Table 4.1: Simulation Parameters for friction compensation with EFP observer

Parameter	Value	Unit
Moment of inertia (J)	10	kgm^2
Coulomb friction (k)	20	Nm
Viscous damping coefficient (b)	2	$Nm \cdot s/rad$
Proportional controller gain (k_p)	150	
Integral controller gain (k_i)	200	
Sampling time	0.0001	sec
α_2 in $g_2(w)$	10	
α_1 in $g_1(w)$	10	

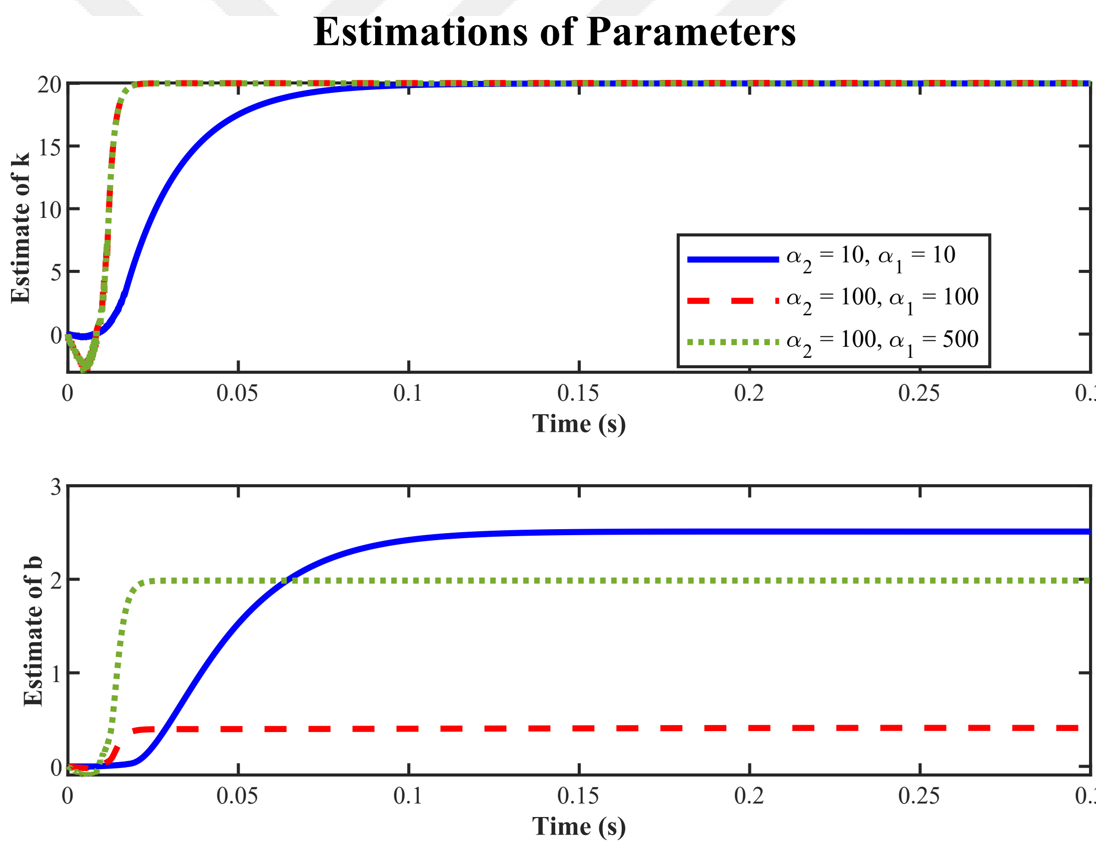

Figure 4.2: Estimation results of Coulomb and viscous friction parameters with respect to varying α parameters

Convergence for the Coulomb friction parameter (k) is achieved; however, the viscous damping coefficient (b) exhibits different convergence behaviors depending on the values of α_1. The value of one parameter influences the other, and thus, combinations of α_2 and α_1 are considered. For the pair (10,10), b converges to 2.51, whereas for (100,100), convergence does not occur, and the estimation oscillates around 0.41. For the combination (100,500), convergence to the true value is observed with a small error. These results demonstrate that the choice of α_2 and α_1 significantly impacts the accuracy of the estimation. Since these parameters act as gain factors in the EFP observer structure, tuning them is essential. The tuning process can be carried out by directly observing the system's response. To find the optimal gain parameters, a grid search algorithm is employed. The implemented search algorithm is presented below.

Algorithm 1 Grid Search to Parameter Tuning

Require: Initial values of α_2 and α_1 , step sizes $\Delta\alpha_2$ and $\Delta\alpha_1$, error threshold
Ensure: Value of α_2^* and α_1^* that minimizes the cost function, and the corresponding value of the cost function f^*

$\alpha_2 \leftarrow 10$
$\alpha_1 \leftarrow 100$
$f \leftarrow \infty$
Initialize F as an empty array
while $f^* <$ error threshold **do**
    $i \leftarrow i + 1$
    $\alpha_2 \leftarrow \alpha_2 \pm \Delta\alpha_2$
    $\alpha_1 \leftarrow \alpha_1 \pm \Delta\alpha_1$
    Run simulation for 4 combinations of Δ sign
    Compute f for each
    $f^* = min(f_1, f_2, f_3, f_4)$
    $F[i] \leftarrow f^*$
    if $F[i] > F[i-1]$ **then**
        $\Delta\alpha_2 \leftarrow \Delta\alpha_2/2$
        $\Delta\alpha_1 \leftarrow \Delta\alpha_1/2$
    end if
end while
$\alpha_2^* \leftarrow \alpha_2$
$\alpha_1^* \leftarrow \alpha_1$
return α_2^*, α_1^*, f^*

The error function utilized in the algorithm is the Mean Absolute Error (MAE). The total error serves as the cost function for the optimization problem. The mean absolute errors for each parameter are computed, and their summation is employed as the overall cost function. By applying the grid search algorithm for parameter tuning, the optimal values for estimating the Coulomb and viscous friction coefficients are determined. The algorithm is implemented with a reference input of a 1 Hz sine wave and a simulation duration of 0.5 seconds. Under these conditions, the parameters successfully converge, as shown in Figure 4.3.

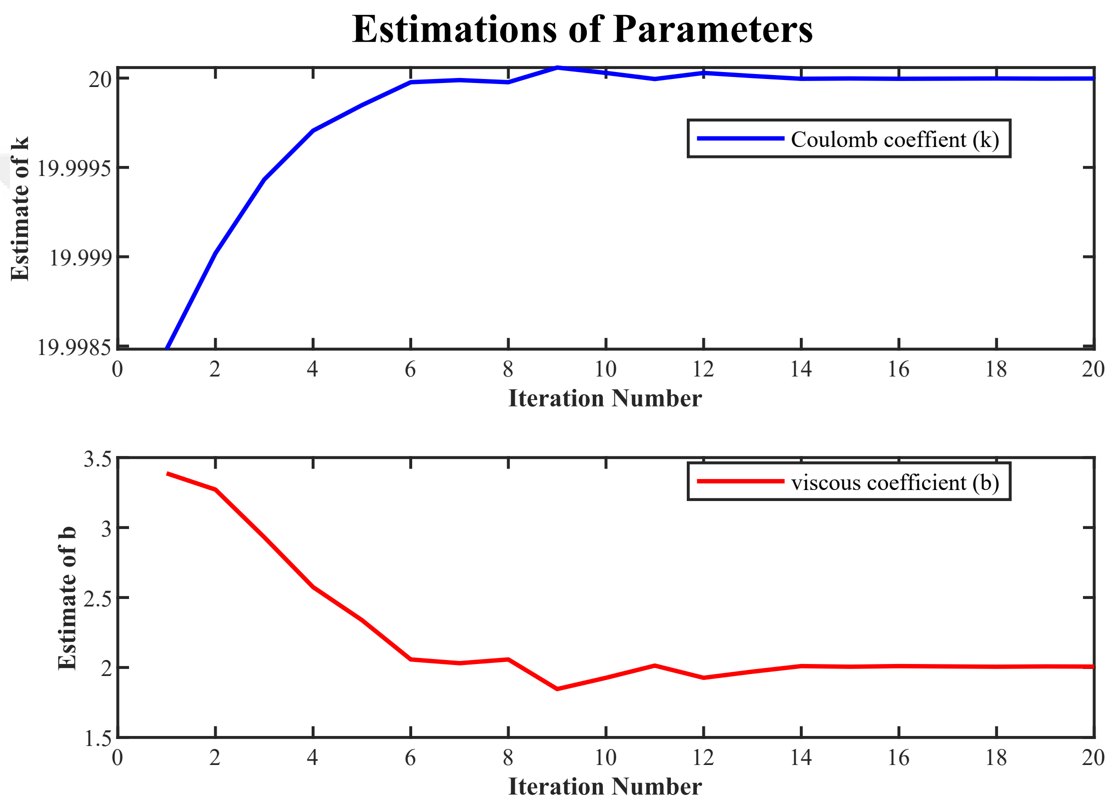

Figure 4.3: Convergence of parameter search algorithm for 1 Hz sine input

A simulation study is conducted to assess the impact of different reference inputs on estimation performance. Table 4.2 presents the estimation results for various reference inputs, along with the optimal observer gains, α_2 and α_1. The iteration number indicates the number of iterations required for convergence, which is considered achieved when the error falls below a threshold of 0.001. The convergence rates for sine and constant inputs, as well as for square and triangular inputs, are similar. The slower convergence of triangular and square inputs may be attributed to the step size and initial condition settings. However, the chirp signal, which varies between 1 and 10 Hz, stands out as an outlier. Based on the discussion of persistent excitation, the chirp signal is the richest in terms of variation over time. This is reflected in the results, with the number of iterations required for convergence being significantly lower compared to the other inputs.

Table 4.2: Estimation results for different reference inputs

Parameter	Sine	Constant	Chirp	Triangular	Square
α_2^*	72.6	59.9	23.7	28.4	65.3
α_1^*	298	8.4	168.7	2.6	3.6
Iteration number	28	29	11	36	37
Error after 20 iterations	0.0071	0.0124	0.0009	0.08	0.1787

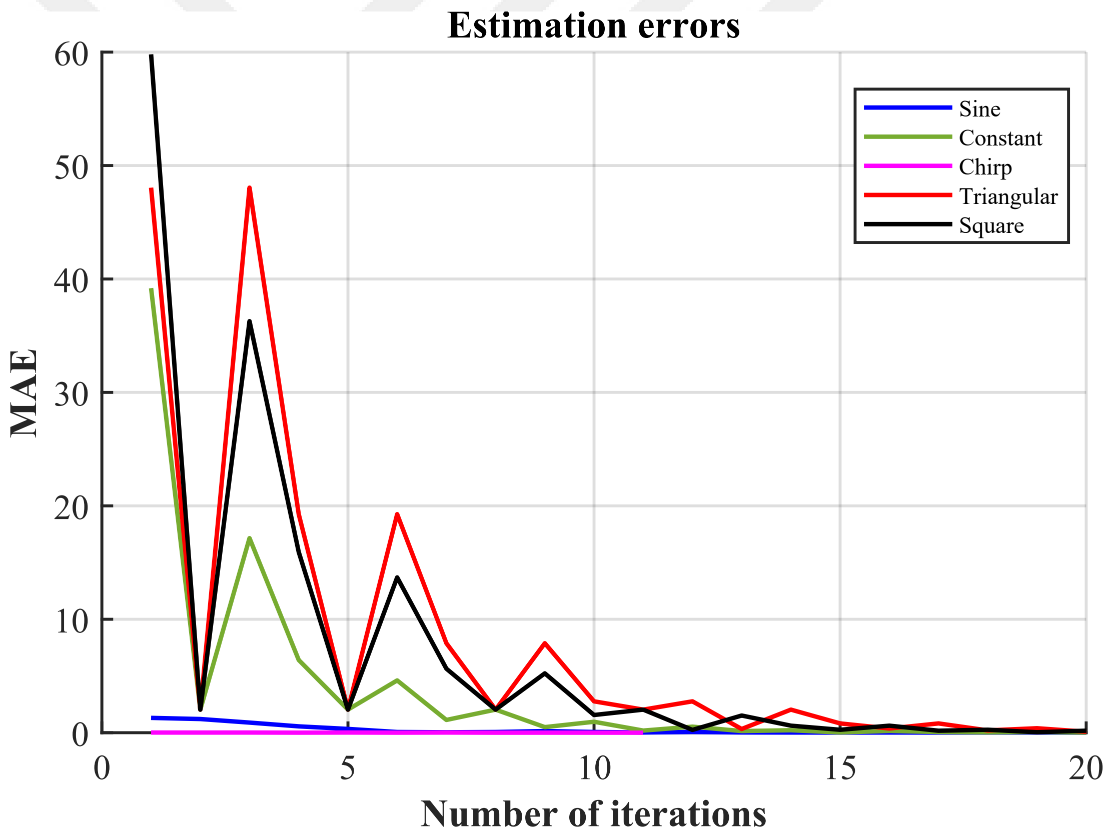

Figure 4.4: Estimation errors for different reference inputs

Consequently, it can be concluded that the chirp signal exhibits the fastest convergence rate. The other signals show similar convergence rates, as they lack sufficient richness in their frequency content. The estimation errors with respect to iterations are presented in Figure 4.4 for the mentioned reference inputs. The error graph for chirp input indicates the fast convergence as it is near 0 in a few iterations. The sine wave can also be considered as a better estimator compared to other three references as it is more stable independent of the initial conditions.

We have demonstrated that the EFP observer successfully estimates the unknown parameters of the Coulomb friction model, with the viscous friction term included. To assess the performance of the proposed friction estimation method, the velocity response of the system is examined using the optimal observer parameters. For 1 Hz sine and 1 Hz triangular wave inputs, the optimal parameters α_2 and α_1 are (72.6, 298) and (28.4, 2.6), respectively.

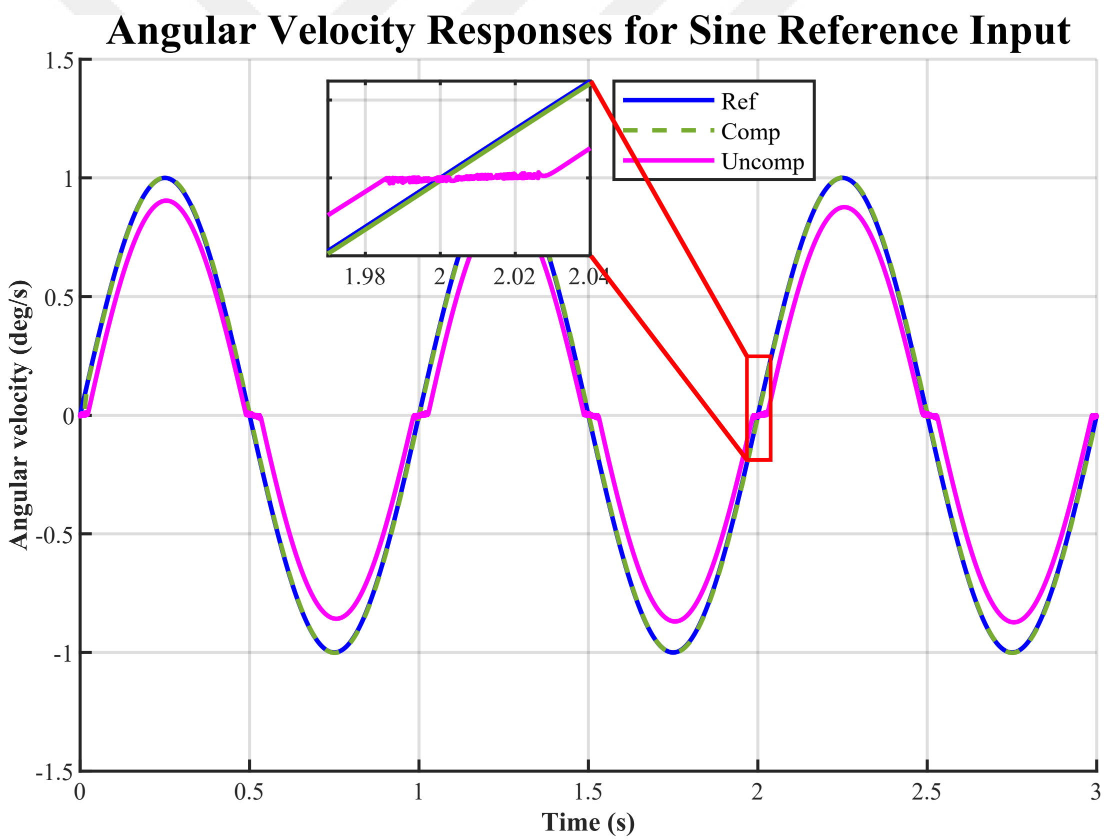

Figure 4.5: Angular velocity response of the system for a sine reference with and without friction compensation

The angular velocity responses, with and without friction compensation for these reference inputs, are presented in Figures 4.5 and 4.6. The EFP observer-based compensation method effectively compensates for friction. Regardless of the input type, the proposed method functions effectively. When compared to other friction compensation methods discussed in previous chapters, EFP shows better tracking performance due to the optimization of the parameters. The faster convergence of the estimation results in a better transient response, leading to enhanced tracking.

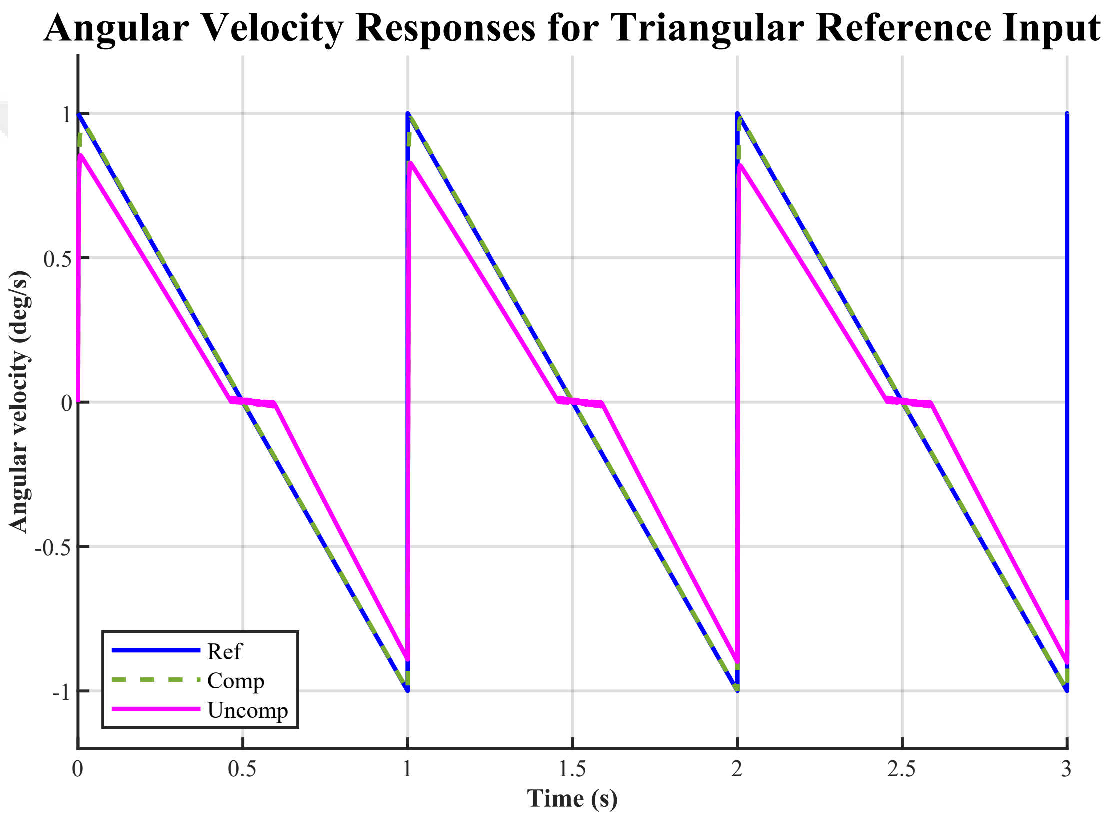

Figure 4.6: Angular velocity response of the system for a triangular reference with and without friction compensation

4.2 Applications of Various Friction Models for Friction Compensation and Their Integration into the EFP Observer

Friction is a complex phenomenon, and its modeling is inherently challenging. In the literature, various friction models exist that aim to capture both the static and dynamic characteristics of friction. Static friction models are relatively simple to implement, requiring fewer parameters for identification. However, in certain systems where dynamic friction plays a dominant role, it becomes essential to account for the dynamic behavior of friction. Nevertheless, implementing a dynamic friction model and accurately identifying its parameters for a specific system can be a difficult and sometimes unfeasible task. Therefore, in cases where friction exhibits complex behavior, such as the presence of a pre-sliding regime, it is often preferable to use a simplified model for friction. In this context, it is valuable to demonstrate that the proposed friction compensation method remains effective, even when the friction in the system is complex and the estimator used is comparatively simpler. To demonstrate this, the LuGre model, discussed in Chapter 1, is employed to model the friction acting on the system. For the estimator, the Coulomb friction model is utilized. Hence, we perform the estimation and compensation of the real friction, LuGre, by assuming as it is a Coulomb friction. The effectiveness of the friction compensation is illustrated by showing that the system response improves even when friction is estimated using a simpler model. The parameters of the LuGre model are presented in Table 4.3, and they are selected specifically to capture the dynamic behavior of the friction more effectively. The reference input is a 1 Hz sine wave, and the simulation parameters are consistent with those provided in 2.1. The angular velocity responses are presented with and without friction compensation in Figure 4.7.

Table 4.3: Simulation Parameters for LuGre Model

Parameter	Value	Unit
Moment of inertia (J)	10	kgm^2
Coulomb friction (F_c)	20	Nm
Stribeck velocity (V_s)	0.03	rad/s
Bristle stiffness (σ_0)	20000	Nm/rad
Bristle damping (σ_1)	1000	$Nm \cdot s/rad$
Viscous damping (σ_2)	2	$Nm \cdot s/rad$

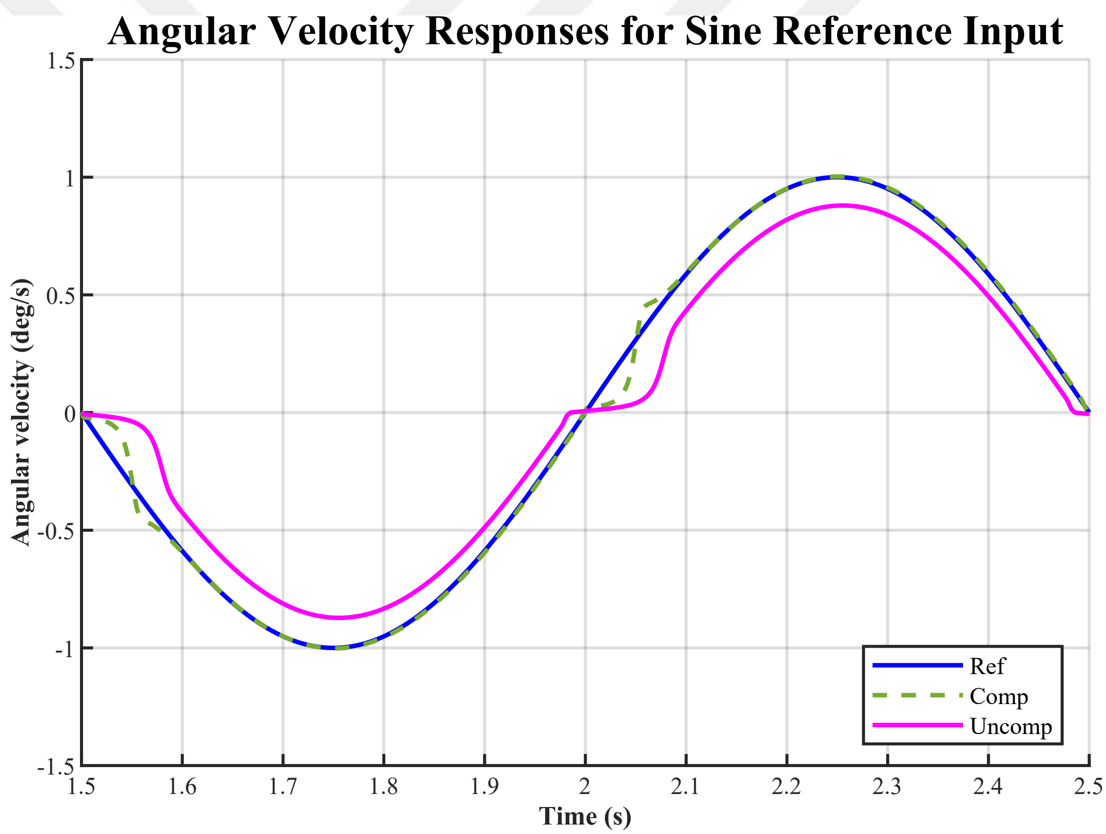

Figure 4.7: Angular velocity response of the system for a sine reference with LuGre friction model

The positive effect of friction compensation on the angular velocity response is evident. The stick-slip phenomenon is more accurately captured using the LuGre model, as it takes into account the pre-sliding regime. Notably, the transition from the pre-sliding phase to the sliding phase is smoother. In contrast, in simpler models like the Coulomb model, the stick-slip phenomenon is interpreted as chattering, resulting from the abrupt sign changes in the friction torque. The compensated signal mitigates the effects of stick-slip during the pre-sliding phase, even though it does not directly estimate the dynamic parameters of the LuGre model. Additionally, the compensation enhances tracking in the sliding regions by effectively addressing the Coulomb friction. Thus, we can conclude that the proposed friction compensation effectively meets the requirement of compensating for complex friction using a simpler model.

As previously discussed, various friction models of differing complexities can be applied to the friction compensation problem. The proposed friction compensation method does not rely exclusively on model-based approaches, where the goal is to match the friction characteristics of the system to a specific model. Instead, the objective is to estimate the parameters of the friction model through experimental data. In the context of the Friedland-Park observer-based friction compensation, friction models are treated as disturbances to be estimated. Therefore, an investigation into the use of the hyperbolic tangent (tanh) function, as an alternative to the signum function for modeling friction, is conducted. The hyperbolic tangent function offers a smoother transition during sign reversals of friction, making it particularly suitable for optimization tasks. The tunable parameter, λ, which controls the steepness of the curve, provides flexibility in adjusting the smoothness of the transition of the input sign. In rotational systems, the velocity sign changes frequently, leading to numerous discontinuities in the friction torque. These discontinuities can result in complex system responses, such as the chattering observed in angular velocity responses in our study. Thus, the Coulomb friction model can be represented by the hyperbolic tangent function, where the value of λ determines the accuracy of representing signum function [42]. The plant model for the system exerting a hyperbolic tangent function is described in below:

$$u_n = u + \hat{k}\tanh(\lambda w) \tag{4.16}$$

$$J\dot{w} = u_n - k\tanh(\lambda w) - bw. \tag{4.17}$$

Substituting (4.16) into (4.17), we obtain

$$J\dot{w} = -e_k \tanh(\lambda w) - bw + u. \tag{4.18}$$

The Friedland-Park observer can be designed as follows:

$$\dot{z} = \frac{(u - bw)}{J} g'(w) \tag{4.19}$$

$$\hat{k} = z - g(w). \tag{4.20}$$

The error dynamics of the estimation is therefore

$$e_k = k - \hat{k} \tag{4.21}$$

$$\begin{aligned}
\dot{e}_k = -\dot{\hat{k}} &= -\dot{z} + g'(w)w' && (4.22)\\
&= -\frac{u}{J} g'(w) + bwg'(w) - g'(w)\tanh(\lambda w)\frac{e_k}{J} - bwg'(w) + \frac{u}{J} g'(w) && (4.23)\\
&= -g'(w)\tanh(\lambda w)\frac{e_k}{J} && (4.24)
\end{aligned}$$

where $g(w)$ is defined as in (2.30). Using the same value of λ both for friction coefficient and observer nonlinearity, results in

$$\dot{e_k} = -\tanh^2(\lambda w)\frac{e_k}{J}. \tag{4.25}$$

The term $-\tanh^2(\lambda w)$ saturates to -1 as the velocity increases in both directions and converges to 0 as the velocity approaches zero. It has been demonstrated that the system described in equations (4.16)-(4.25) successfully compensates for friction in the Modified Friedland-Park (MFP) observer case, where Coulomb friction with the signum function is employed. To further validate the friction compensation method, simulations are conducted for the case where the friction model acting on the plant utilizes the signum function and the estimator utilizes the hyperbolic tangent function. This comparison aims to demonstrate the effectiveness of the compensation method across various friction model pairs. The simulation parameters are consistent with those in Table 2.5, except for the α parameter. The α and λ parameters in $g_3(w)$ are fixed to 100 and 1, respectively. The reference input is a 1 Hz sine wave. The real friction acting on the plant and the estimated friction obtained by the observer are compared in Figure 4.8

for different values of λ. As previously noted, the accuracy of the representation of the signum function depends on the λ parameter of the hyperbolic tangent function. Consequently, the accuracy of the estimation improves as the value of λ increases. This result is crucial for evaluating the performance of friction compensation under varying estimation accuracies. To illustrate this, angular velocity responses are presented. From Figure 4.9, it can be concluded that friction compensation is ineffective when the estimation of the friction acting on the system is inaccurate. Therefore, it is essential to use an estimator model that accurately represents the actual friction in the system.

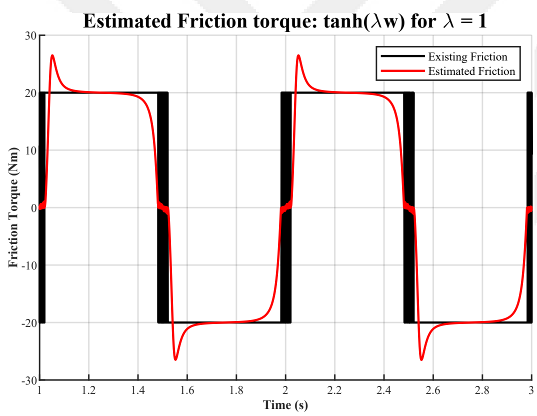

(a) Friction torques for $\lambda = 1$

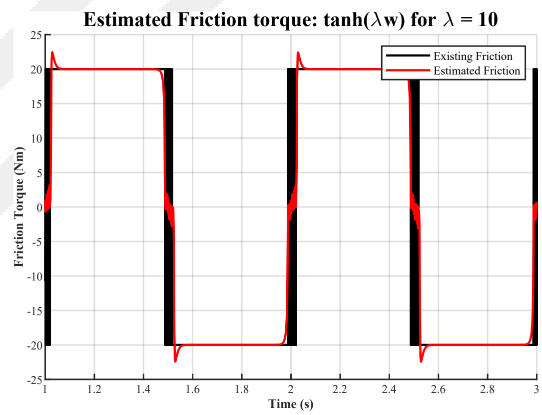

(b) Friction torques for $\lambda = 10$

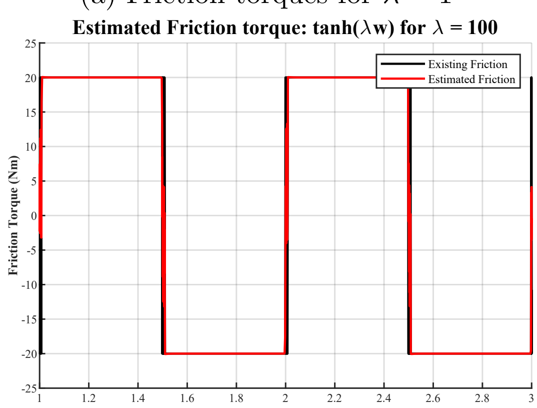

(c) Friction torques for $\lambda = 100$

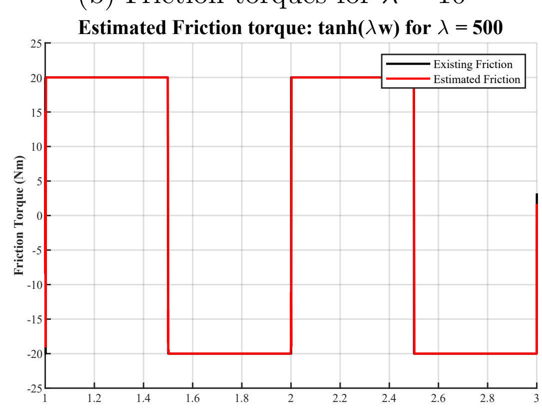

(d) Friction torques for $\lambda = 500$

Figure 4.8: Existing and estimated friction torques for 1 Hz sine wave input for different λ parameters of $\tanh(\lambda w)$

For $\lambda = 1$, the estimation of Coulomb friction is inaccurate, resulting in an uncompensated velocity response, as shown in Figure 4.9 (a). For $\lambda = 10$ the estimation remains insufficiently accurate, and friction compensation is still not achieved. At $\lambda = 100$, the tanh function closely approximates the signum function, providing enough accuracy to mitigate the chattering observed in the velocity response, as seen in Figure 4.9. Finally, for $\lambda = 500$ the tanh function converges to classical Coulomb friction, resulting in a perfect estimation of the friction and a fully compensated velocity response, as shown in Figure 4.9 (d). For increasing values of λ, the control signal, remains at the desired range, meaning that it does not generate unrealizable inputs to the plant. These analyses focus on the compensation performance near zero velocity. In the sliding phase, friction is compensated due to the similarity between the actual and estimated friction torques, as depicted in Figure 4.8. For velocity readings that are far from 0, the error of estimation converges to 0 as shown in (4.25).

Table 4.4: Mean Absolute Error (MAE) of angular velocities and friction torques for different λ values

Mean Absolute Error	$\lambda = 0$ (no comp.)	$\lambda = 1$	$\lambda = 10$	$\lambda = 100$	$\lambda = 500$
Angular velocity (deg/s)	0.1208	0.0162	0.0091	0.0057	0.0054
Friction torque (Nm)	19.99	3.43	1.64	0.41	0.16

The mean absolute errors (MAE) on estimated friction torques and angular velocity responses are also provided in Table 4.4. As discussed, friction compensation is achieved with accurate estimations for $\lambda = 100$ and $\lambda = 500$. In these cases, estimation errors in friction torque are less than 1 Nm. The reduction in error from $\lambda = 1$ to $\lambda = 500$ is 66.7%, while the improvement from no compensation to full compensation is 95.5%.

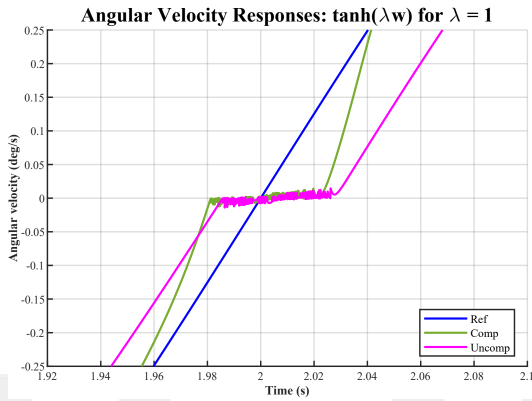

(a) Angular velocities for $\lambda = 1$

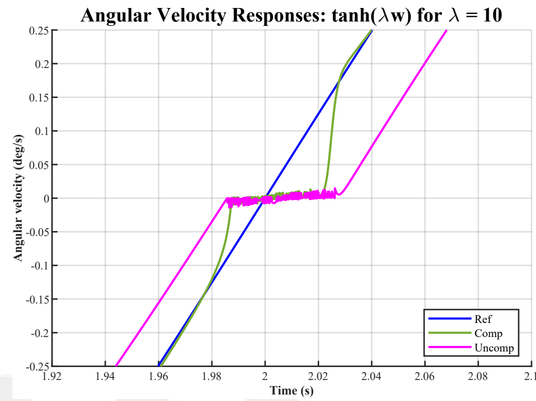

(b) Angular velocities for $\lambda = 10$

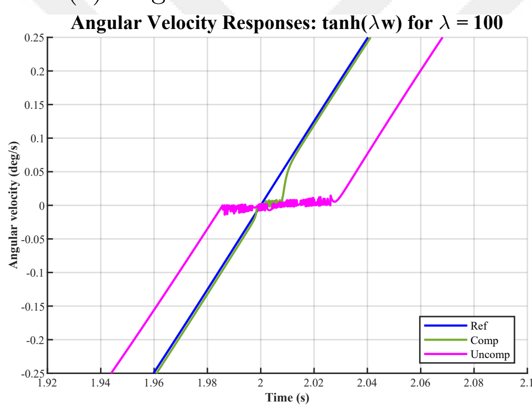

(c) Angular velocities for $\lambda = 100$

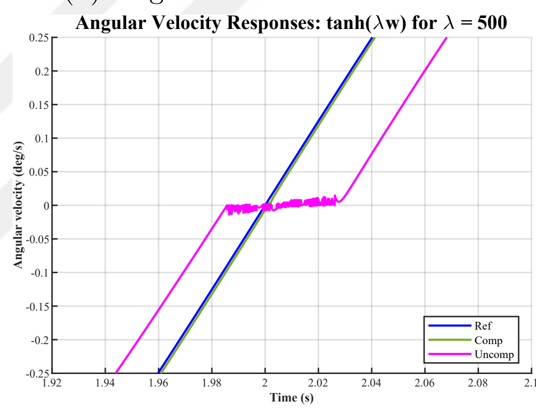

(d) Angular velocities for $\lambda = 500$

Figure 4.9: Friction compensated and uncompensated angular velocity responses of the system for 1 Hz sine wave input for different λ parameters of $\tanh(\lambda w)$

Assuming the existing friction follows a hyperbolic tangent function rather than the standard Coulomb friction model, one can apply a similar friction compensation analysis as presented in Chapter 2. The Modified Friedland-Park (MFP) observer involves estimating the Coulomb friction coefficient (k) under the assumption that the viscous coefficient (b) is known. In contrast, the Novel Friedland-Park (NFP) observer estimates the viscous coefficient (b) while assuming that the Coulomb friction coefficient (k) is known. Since the proposed friction model $F_f = k\tanh(\lambda w)$ includes two parameters, it is possible to apply the same structure as in the NFP and investigate whether the λ parameter can be estimated. The equations of the system and the observer structure is presented in below:

$$u_n = u + k\tanh(\hat{\lambda}w) \tag{4.26}$$

$$J\dot{w} = u_n - k\tanh(\lambda w). \tag{4.27}$$

Hence, the observer can be designed as follows:

$$\dot{z} = \frac{u}{J}g'(w) \tag{4.28}$$

$$\hat{\lambda} = z - g(w), \tag{4.29}$$

where the estimation error is defined as

$$e_k = \lambda - \hat{\lambda}. \tag{4.30}$$

The error dynamics of the estimation is therefore

$$\begin{aligned}
\dot{e}_\lambda = -\dot{\hat{\lambda}} &= -\dot{z} + g'(w)w' && (4.31)\\
&= \frac{-g'(w)k}{J}[\tanh(\lambda w) - \tanh(\hat{\lambda}w)] && (4.32)\\
&\approx -\frac{-g'(w)kwe_\lambda}{J} && (4.33)
\end{aligned}$$

by utilizing the following approximation

$$\tanh(\lambda w) - \tanh(\hat{\lambda}w) \approx (\lambda - \hat{\lambda})w. \tag{4.34}$$

With this design, it is expected that the observer will estimate the λ parameter and compensate for friction, as was observed in the case of the unknown viscous coefficient (b). For the simulations, the observer gain parameters α_3 and λ_3 in $g_3(w)$ are selected as 500 and 100, respectively to obtain a better estimation convergence according to the results as in NFP case. The simulation parameters are presented in Table 4.5. The angular velocity responses with and without friction compensation applied are presented in Figure 4.10.

Table 4.5: Simulation Parameters for tanh Friction Estimation of λ parameter

Parameter	Value	Unit
Moment of inertia (J)	10	kgm^2
Coulomb friction coefficient (k)	20	Nm
Steepness of tanh friction (λ)	25	
α_3 in $g_3(w)$	500	
λ_3 in $g_3(w)$	100	
Proportional controller gain (k_p)	150	
Integral controller gain (k_i)	200	
Sampling time	0.0001	sec

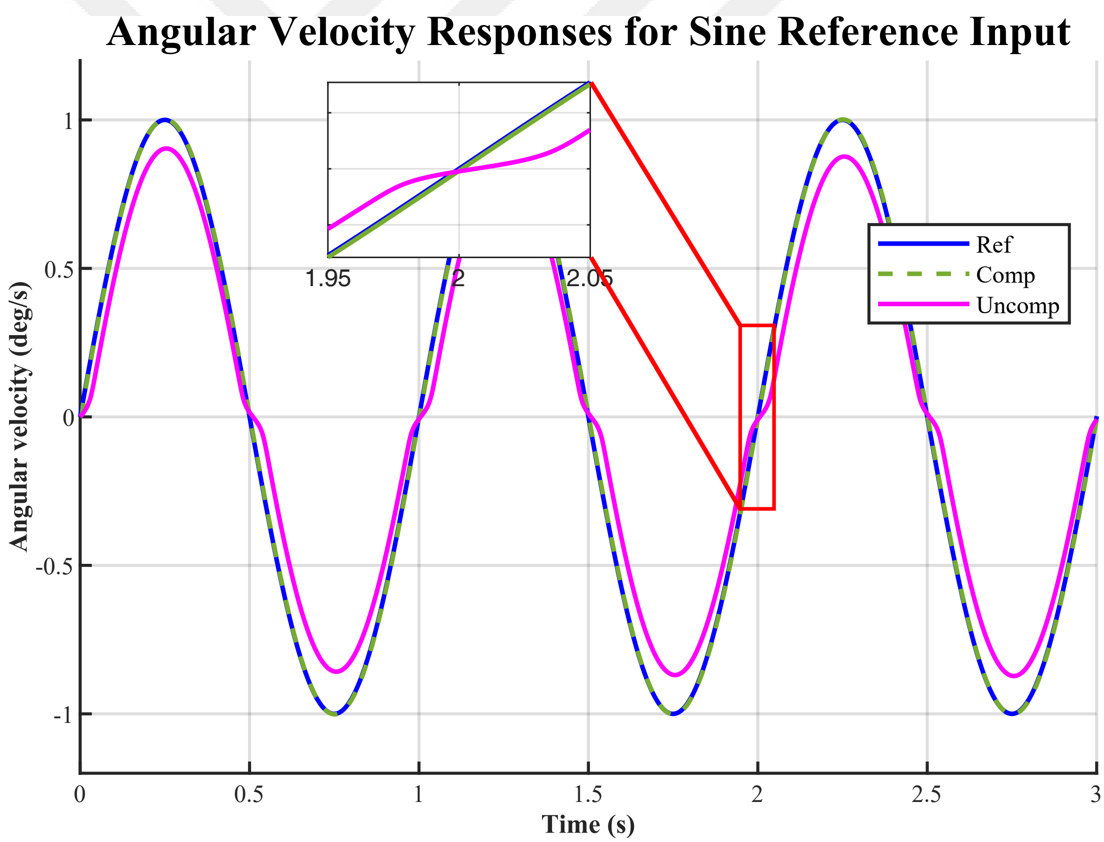

Figure 4.10: Angular velocity responses for the case of estimating λ

Note that the smoothness of the transition during velocity reversals is a result of the continuous nature of the proposed friction model. The sticky behavior of the velocity response remains present, but it is effectively compensated using a friction observer. Another observation from the simulations pertains to the selection of observer parameters based on the parameter to be estimated. Using the observer parameter values provided in Table 4.5, simulations were conducted for different values of the steepness parameter, λ, of the hyperbolic tangent function. For lower values of λ, the observer gain parameters remain excessively high relative to the low value of the parameter being estimated, resulting in system instability. The control signals corresponding to different λ values can be observed in Figure 4.11. The system exhibits oscillations periodically resulting in an unstable system behavior.

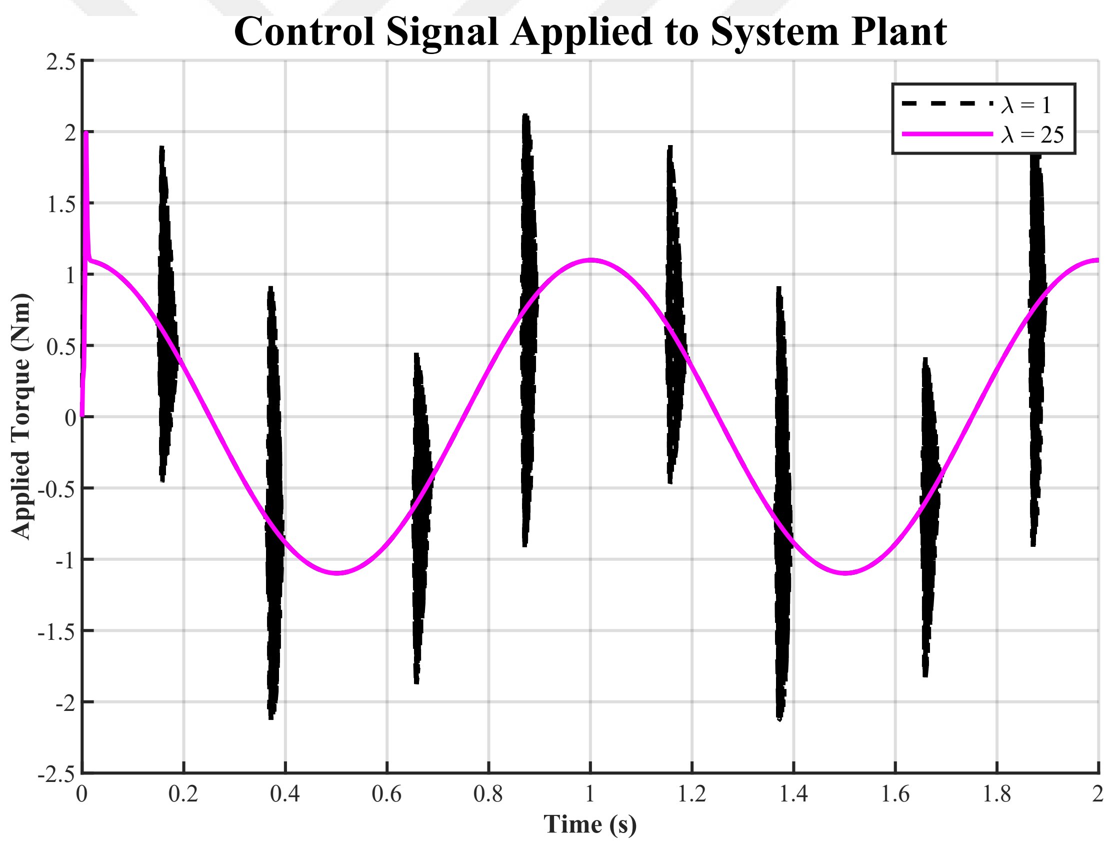

Figure 4.11: Control signals for $\lambda = 1$ and $\lambda = 25$

We have demonstrated that the parameters of the hyperbolic tangent friction model can be estimated using the Friedland-Park observer structure. Building on this foundation, we will extend the discussion to the estimation of two parameters using the tanh model. It has been shown that the proposed Extended

Friedland-Park (EFP) observer successfully estimates the two parameters of the classical Coulomb friction model. Accordingly, the implementation of the two-state EFP observer structure for estimating the parameters of the tanh model can be undertaken. This implementation is analyzed as two extensions.

Extension 1: Viscous damping coefficient is assumed to be known. Coulomb friction coefficient (k) and steepness of tanh (λ) are unknown parameters.

Extension 2: Coulomb friction coefficient (k) is assumed to be known. The steepness of tanh (λ) and viscous damping coefficient (b) are unknown parameters.

Using the same EFP observer structure presented in 4.1, simulations for the extension cases are conducted. The only difference is that the existing friction is not the standard Coulomb friction but is instead replaced with the hyperbolic tangent (tanh) model. The simulation parameters are presented in Table 4.6. The reference input is 1 Hz sine wave. The nonlinear functions described in (2.28) and (2.29) are utilized within the observer. In Extension 1, $g_1(w)$ is employed to estimate the parameter k, while in Extension 2, it is used to estimate b. For the estimation of λ, $g_2(w)$ is applied in both cases. The α parameters of the observer are tuned using Algorithm 1, which identifies the optimal gains that result in fast and accurate parameter estimation. The angular velocity responses of the system are presented in Figures 4.12 and 4.13, respectively. The friction is successfully compensated for both cases with the velocity errors in Table 4.7. It is noteworthy that the uncompensated velocity response exhibits a smoother transition near velocity reversals compared to Figure 4.10. This difference is attributed to the variations in the steepness of the friction model. The steepness parameter is set to 25 for single-parameter estimation and 10 for two-parameter estimation. For $\lambda = 10$, the friction model is less steep, leading to a smoother transition in zero velocity crossings.

Table 4.6: Simulation Parameters for Two-state tanh Friction Estimation

Parameter	Value	Unit
Moment of inertia (J)	10	kgm^2
Coulomb friction coefficient (k)	20	Nm
Steepness of tanh friction (λ)	10	
Viscous damping coefficient (b)	2	$Nm \cdot s/rad$
Proportional controller gain (k_p)	150	
Integral controller gain (k_i)	200	
Sampling time	0.0001	sec
α_1 in $g_1(w)$ for Extension 1	338	
α_2 in $g_2(w)$ for Extension 1	10.8	
α_1 in $g_1(w)$ for Extension 2	90	
α_2 in $g_2(w)$ for Extension 2	30	

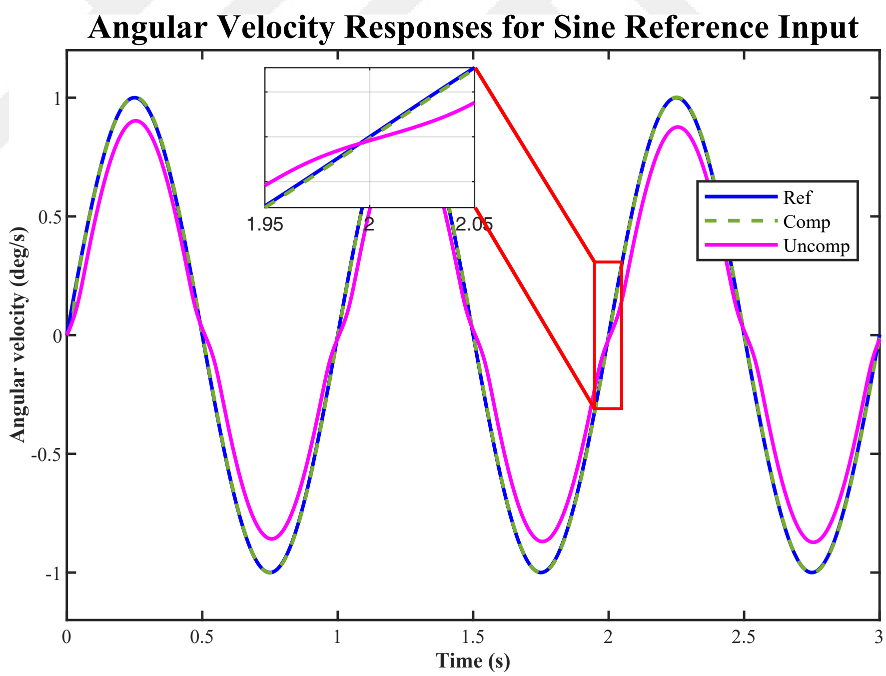

Figure 4.12: Angular velocity responses for Extension 1

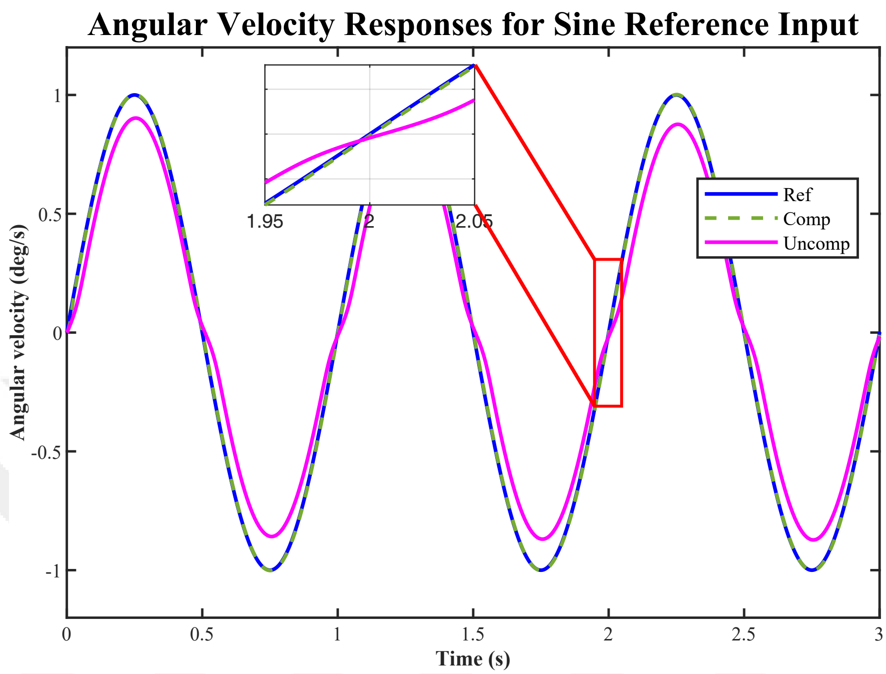

Figure 4.13: Angular velocity responses for Extension 2

Table 4.7: Errors on Angular Velocities of Extension 1 and Extension 2

MAE on velocity (deg/s)	Comp.	Uncomp.
Extension 1	0.0048	0.0116
Extension 2	0.0046	0.0116

One observation is made about the selection of observer gain parameters for two-state estimation. The search algorithm finds the optimum α values by minimizing the error, however the accuracy and the rate of the estimation is quite sensitive to the changes in α values. Friedland and Park states in [27] that the bandwidth of the observer increase for larger values of α which yields a faster response. In [43], the convergence rate is also analyzed by approximating the pole location of the observer from error dynamics of the estimation. The error dynamics for classical Friedland-Park observer that we discussed is as in (2.16):

$$\dot{e_k} = -g'(w)\,\mathrm{sign}(w)\frac{e_k}{J}, \tag{4.35}$$

where the nonlinear function can be selected as $g(w) = \alpha|w|$. The derivative of $g(w)$ is

$$g'(w) = \alpha \operatorname{sign}(w). \tag{4.36}$$

By plugging $g'(w)$ into (4.35), the error dynamics equation becomes

$$\dot{e_k} = -\frac{\alpha}{J} e_k, \tag{4.37}$$

since $sign(w) \cdot sign(w) = 1$. The explicit solution of the differential equation in (4.37) is therefore

$$e(t) = e(0)e^{-\frac{\alpha}{J}t} \tag{4.38}$$

Hence, the pole of the observer is at

$$p = -\frac{\alpha}{J}. \tag{4.39}$$

The pole of the observer is directly influenced by the gain parameter α. Poles farther from the origin result in faster convergence of the state estimates, corresponding to larger values of α. This observation aligns with the findings of Friedland and Park. However, faster poles can increase the system's sensitivity to noise. Additionally, inaccuracies in the friction model may degrade estimation performance due to the amplification of modeling mismatches with faster poles. This trade-off should be considered in terms of the robustness of the estimation process. By framing the selection of observer parameters as a pole placement problem, the parameters can be designed to meet specific performance criteria. In summary, the proper selection of observer gain parameters is critical, as they determine the observer poles and directly impact the estimation performance.

Chapter 5

Conclusion

In this dissertation, the primary objective was to design and analyze a friction compensation method to mitigate stick-slip motion in nonlinear systems. The study aimed to enhance the system performance through adaptive control strategies. Initially, the classical Friedland-Park observer was employed to address friction compensation in a single-mass model, where the system assumes the inertia is lumped at the load. This observer was used to estimate the Coulomb friction coefficient. Additionally, two variations of the classical Friedland-Park observer were explored. The first variation incorporated the viscous damping coefficient into the observer structure, demonstrating that different system parameters can be integrated into the observer framework to enhance its versatility. The second variation aims to extend the observer's capability by estimating the viscous damping term under the assumption of known Coulomb friction coeffient. By adapting the viscous damping term to the plant model, we concluded that the Friedland-Park observer can be utilized for system identification applications where the objective is estimate the plant parameters. It was shown that the classical Friedland-Park and its variations demonstrated significant improvements in reducing friction-induced oscillations, as evidenced by a 60-65% reduction in tracking error. Comparative analysis of compensated and uncompensated cases highlighted the effectiveness of the methods in addressing non-linear effects caused by friction.

The study further investigates the application of the Friedland-Park observer in high-order systems. In this regard, a two-mass model comprising a motor and a load was implemented. The friction compensation performance of the Friedland-Park observer for the two-mass system was analyzed. Two distinct controller schemes were employed, and it was demonstrated that friction compensation is necessary regardless of the controllers' differing bandwidths and transient characteristics. The proposed method's effectiveness in high-order systems was evaluated in both the velocity and position control loops. Without friction compensation, the system's velocity and angular position tracking performance are significantly affected by the disruptive effects of friction, particularly during velocity direction changes. This implementation demonstrates that the Friedland-Park observer can be applied to more complex systems while maintaining its effectiveness in compensating for friction.

Finally, a friction compensation scheme was proposed by extending the Friedland-Park observer to enable two-state estimation. For the two-state parameter estimation scenario, it was demonstrated that tuning the observer parameters is essential for achieving convergence. Optimal parameters were determined by identifying those that minimized the velocity tracking error. The performance of the estimation was analyzed in terms of both convergence rate and accuracy using various reference inputs. The method was evaluated within the framework of persistently exciting signals, revealing that input signals with frequent variations facilitate faster convergence. The two-state estimation approach was also implemented for various friction models beyond the Coulomb and viscous friction models. Specifically, a friction model employing a hyperbolic tangent function was utilized. It was shown that the two-state estimation scheme effectively estimated different parameter combinations in the friction model, including the steepness of the friction. The system's tracking performance with friction compensation improved significantly when the two-state estimator with optimal observer parameters was applied. Additionally, the proposed friction model reduced the chattering effect during velocity sign reversals, resulting in smoother transitions.

The study presents several opportunities for future extensions. One potential direction is the inclusion of a gyroscope model to achieve a more realistic representation of angular velocity measurements. This enhancement would enable the evaluation of the proposed friction estimation method under the influence of noisy measurements. Additionally, a Kalman filter could be implemented to fuse the sensor measurements from the gyroscope and encoder, thereby improving estimation accuracy in practical applications. Another extension involves the estimation of plant model parameters. By considering the stiffness and damping in a two-mass model as unknown system parameters and formulating the observer equations accordingly, the proposed method could be adapted for plant model parameter estimation. This outcome may be beneficial for broadening the scope of the problem to system identification purposes. With this approach, the problem can be extended to identify the system parameters including plant, friction, or other components of the system. Finally, hardware implementation of the proposed method on a simple inertial mechanical system could be undertaken. Such experiments would provide valuable insights into the compensation performance of the method, particularly in terms of reference tracking accuracy in real-world applications. These future directions offer significant potential to enhance the applicability and robustness of the proposed method.

Bibliography

[1] J. Den Hartog, "Forced vibrations with combined coulomb and viscous friction," *Transactions of the American Society of Mechanical Engineers*, vol. 53, no. 2, pp. 107–115, 1931.

[2] M. Jelali and B. Huang, *Detection and diagnosis of stiction in control loops: state of the art and advanced methods.* Springer Science & Business Media, 2009.

[3] R. Stribeck, "The key qualities of sliding and roller bearings," *Zeitschrift des Vereines Seutscher Ingenieure*, vol. 46, no. 38, pp. 1342–1348, 1902.

[4] P. R. Dahl, "Solid friction damping of mechanical vibrations," *AIAA journal*, vol. 14, no. 12, pp. 1675–1682, 1976.

[5] B. Armstrong-Hélouvry, P. Dupont, and C. C. De Wit, "A survey of models, analysis tools and compensation methods for the control of machines with friction," *Automatica*, vol. 30, no. 7, pp. 1083–1138, 1994.

[6] C. C. De Wit, H. Olsson, K. J. Astrom, and P. Lischinsky, "A new model for control of systems with friction," *IEEE Transactions on automatic control*, vol. 40, no. 3, pp. 419–425, 1995.

[7] E. Berger, "Friction modeling for dynamic system simulation," *Appl. Mech. Rev.*, vol. 55, no. 6, pp. 535–577, 2002.

[8] J. Swevers, F. Al-Bender, C. G. Ganseman, and T. Projogo, "An integrated friction model structure with improved presliding behavior for accurate friction compensation," *IEEE Transactions on automatic control*, vol. 45, no. 4, pp. 675–686, 2000.

[9] H. Olsson, K. J. Åström, C. C. De Wit, M. Gäfvert, and P. Lischinsky, "Friction models and friction compensation," *Eur. J. Control*, vol. 4, no. 3, pp. 176–195, 1998.

[10] K. Johanastrom and C. Canudas-De-Wit, "Revisiting the lugre friction model," *IEEE Control systems magazine*, vol. 28, no. 6, pp. 101–114, 2008.

[11] E. Sincar, "Friction identification and compensation of its effects in stabilized platforms," Master's thesis, Middle East Technical University, 2013.

[12] Y. Chen, X. Lv, J. Zhang, and W. Zhang, "An adaptive compensation method of lugre model-based friction for electromechanical actuator servo system," in *2022 41st Chinese Control Conference (CCC)*, pp. 2168–2173, IEEE, 2022.

[13] L. Freidovich, A. Robertsson, A. Shiriaev, and R. Johansson, "Lugre-model-based friction compensation," *IEEE Transactions on Control Systems Technology*, vol. 18, no. 1, pp. 194–200, 2009.

[14] G. Bishop, G. Welch, *et al.*, "An introduction to the kalman filter," *Proc of SIGGRAPH, Course*, vol. 8, no. 27599-23175, p. 41, 2001.

[15] Z. Jamaludin, H. Van Brussel, and J. Swevers, "Friction compensation of an xy feed table using friction-model-based feedforward and an inverse-model-based disturbance observer," *IEEE Transactions on Industrial Electronics*, vol. 56, no. 10, pp. 3848–3853, 2009.

[16] W.-F. Xie, "Sliding-mode-observer-based adaptive control for servo actuator with friction," *IEEE Transactions on Industrial Electronics*, vol. 54, no. 3, pp. 1517–1527, 2007.

[17] T. H. Lee, K. K. Tan, and S. Huang, "Adaptive friction compensation with a dynamical friction model," *IEEE/ASME transactions on mechatronics*, vol. 16, no. 1, pp. 133–140, 2010.

[18] C. Tang, Y. Fan, C. Yang, M. Cheng, and C. H. Lee, "Friction identification and compensation for spmsm using robust adaptive observer," *IEEE Journal of Emerging and Selected Topics in Power Electronics*, 2024.

[19] L. Schuchman, "Dither signals and their effect on quantization noise," *IEEE Transactions on Communication Technology*, vol. 12, no. 4, pp. 162–165, 1964.

[20] A. Bonchis, P. I. Corke, D. C. Rye, and Q. P. Ha, "Variable structure methods in hydraulic servo systems control," *Automatica*, vol. 37, no. 4, pp. 589–595, 2001.

[21] V. Lampaert, J. Swevers, and F. Al-Bender, "Comparison of model and non-model based friction compensation techniques in the neighbourhood of pre-sliding friction," in *Proceedings of the 2004 American control conference*, vol. 2, pp. 1121–1126, IEEE, 2004.

[22] G. Palli and C. Melchiorri, "Velocity and disturbance observer for non-model based load and friction compensation," in *2008 10th IEEE international workshop on advanced motion control*, pp. 194–199, IEEE, 2008.

[23] C. C. De Wit and S. Ge, "Adaptive friction compensation for systems with generalized velocity/position friction dependency," in *Proceedings of the 36th IEEE Conference on Decision and Control*, vol. 3, pp. 2465–2470, IEEE, 1997.

[24] J.-H. Ryu, J. Song, and D.-S. Kwon, "A nonlinear friction compensation method using adaptive control and its practical application to an in-parallel actuated 6-dof manipulator," *Control Engineering Practice*, vol. 9, no. 2, pp. 159–167, 2001.

[25] K. Verbert, R. Tóth, and R. Babuška, "Adaptive friction compensation: a globally stable approach," *IEEE/ASME Transactions on Mechatronics*, vol. 21, no. 1, pp. 351–363, 2015.

[26] M. Noorbakhsh and A. Yazdizadeh, "Adaptive friction compensation in a two-link planar robot manipulator using a new lyapunov-based controller," in *IEEE ICCA 2010*, pp. 2132–2137, IEEE, 2010.

[27] B. Friedland, Y.-J. Park, *et al.*, "On adaptive friction compensation," *IEEE Transactions on automatic control*, vol. 37, no. 10, pp. 1609–1612, 1992.

[28] C. Odabaş, *Adaptive observer designs for friction estimation in position control of simple mechanical systems with time delay.* PhD thesis, Bilkent Universitesi (Turkey), 2021.

[29] C. Odabaş and Ö. Morgül, "A novel observer design for lugre friction estimation and control," *arXiv preprint arXiv:2501.04793*, 2025.

[30] C. Odabaş and Ö. Morgül, "Adaptive friction compensations for mechanical systems with measurement delay," *Transactions of the Institute of Measurement and Control*, vol. 43, no. 8, pp. 1745–1759, 2021.

[31] C. Odabaş and Ö. Morgül, "A novel observer design for friction estimation," *International Journal of Control*, vol. 97, no. 6, pp. 1418–1431, 2024.

[32] M. Phan, L. G. Horta, J.-N. Juang, and R. W. Longman, "Linear system identification via an asymptotically stable observer," *Journal of Optimization Theory and Applications*, vol. 79, pp. 59–86, 1993.

[33] R. Hellsen, G. Z. Angelis, M. Van de Molengraft, A. De Jager, and J. Kok, "Grey-box modeling of friction: An experimental case-study," *European Journal of Control*, vol. 6, no. 3, pp. 258–267, 2000.

[34] S. S. Rao and F. F. Yap, *Mechanical vibrations*, vol. 4. Addison-Wesley New York, 1995.

[35] G. Ellis, *Control system design guide: using your computer to understand and diagnose feedback controllers.* Butterworth-Heinemann, 2012.

[36] M. C. Readman, *Flexible joint robots.* CRC press, 1994.

[37] M. Spong, "Modeling and control of elastic joint robots," *Mathematical and Computer Modelling*, vol. 12, no. 7, p. 912, 1989.

[38] Z. Zheng, G. Hu, and B. Hu, "Phase slips and phase synchronization of coupled oscillators," *Physical Review Letters*, vol. 81, no. 24, p. 5318, 1998.

[39] M. Ruderman and M. Iwasaki, "Observer of nonlinear friction dynamics for motion control," *IEEE Transactions on Industrial Electronics*, vol. 62, no. 9, pp. 5941–5949, 2015.

[40] S. Boyd and S. S. Sastry, "Necessary and sufficient conditions for parameter convergence in adaptive control," *Automatica*, vol. 22, no. 6, pp. 629–639, 1986.

[41] S. Boyd and S. Sastry, "On parameter convergence in adaptive control," *Systems & control letters*, vol. 3, no. 6, pp. 311–319, 1983.

[42] N. Mostaghel and T. Davis, "Representations of coulomb friction for dynamic analysis," *Earthquake engineering & structural dynamics*, vol. 26, no. 5, pp. 541–548, 1997.

[43] S. Tafazoli, C. W. de Silva, and P. D. Lawrence, "Tracking control of an electrohydraulic manipulator in the presence of friction," *IEEE Transactions on Control Systems Technology*, vol. 6, no. 3, pp. 401–411, 1998.

Appendix A

Figures

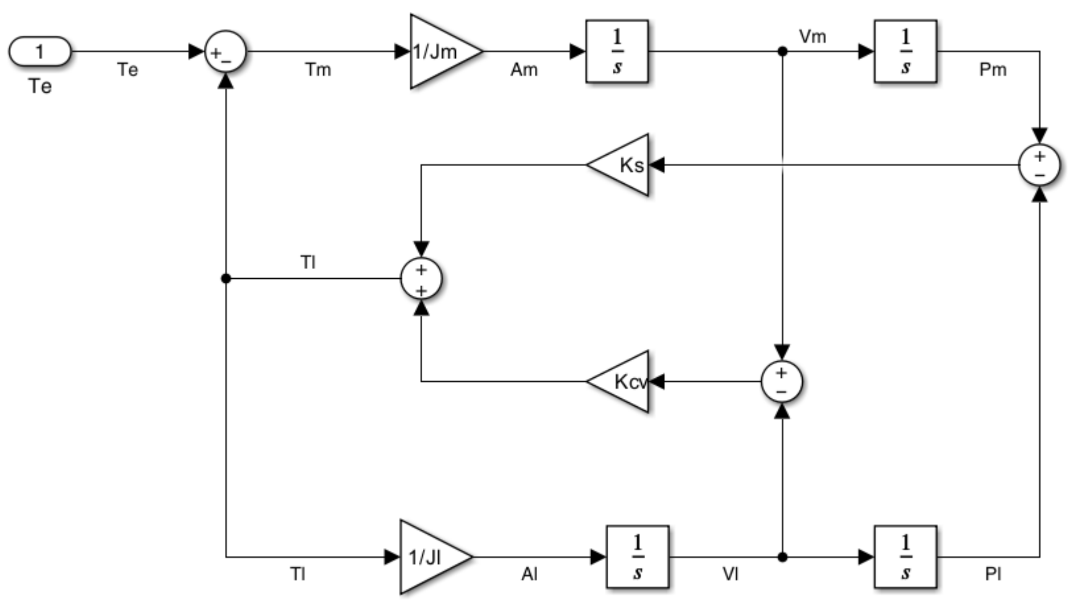

Figure A.1: Two-mass model implementation in Simulink

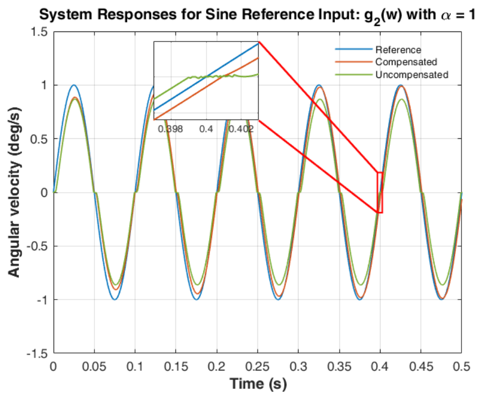

(a) Angular velocities for $\alpha = 1$

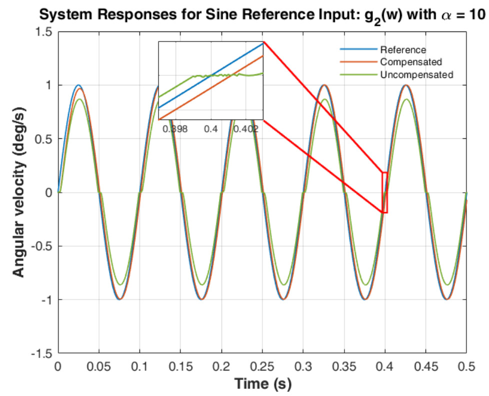

(b) Angular velocities for $\alpha = 10$

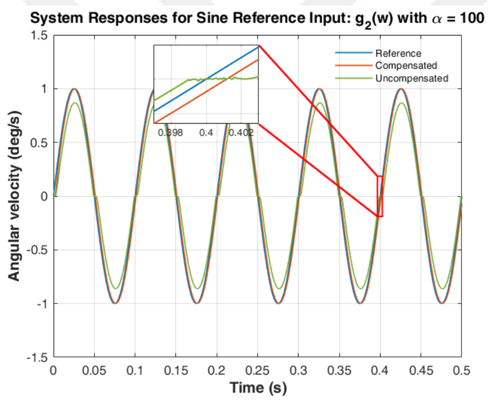

(c) Angular velocities for $\alpha = 100$

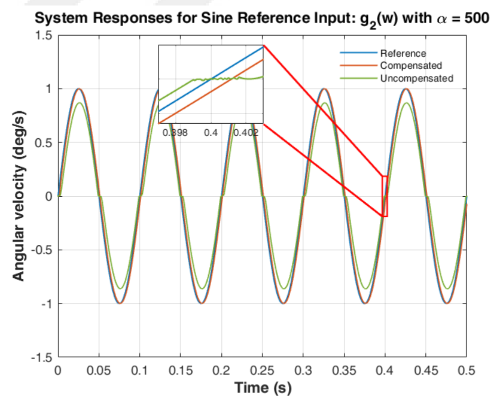

(d) Angular velocities for $\alpha = 500$

Figure A.2: Friction compensated and uncompensated angular velocity responses of the system for 10 Hz sine wave input with different α parameters of $g_2(w)$ for CFP observer

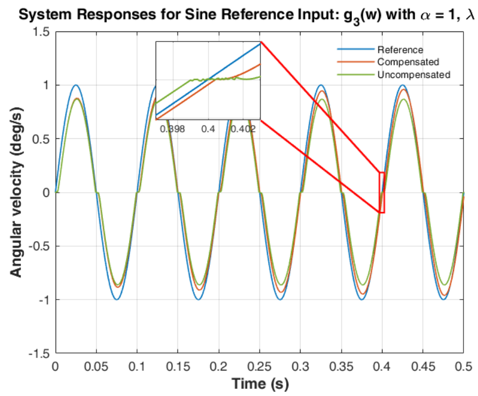

(a) Angular velocities for $\alpha = 1$, $\lambda = 1$

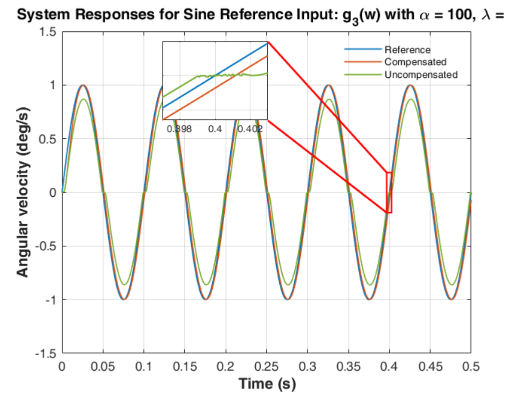

(b) Angular velocities for $\alpha = 100$, $\lambda = 1$

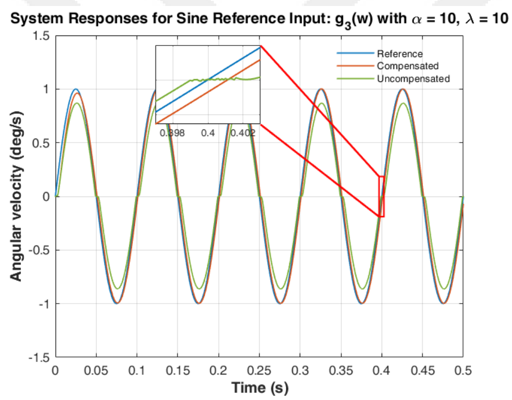

(c) Angular velocities for $\alpha = 10$, $\lambda = 10$

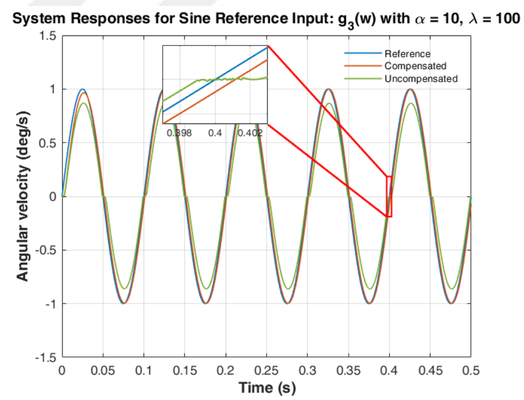

(d) Angular velocities for $\alpha = 10$, $\lambda = 100$

Figure A.3: Friction compensated and uncompensated angular velocity responses of the system for 10 Hz sine wave input with different α and λ parameters of $g_3(w)$ for CFP observer

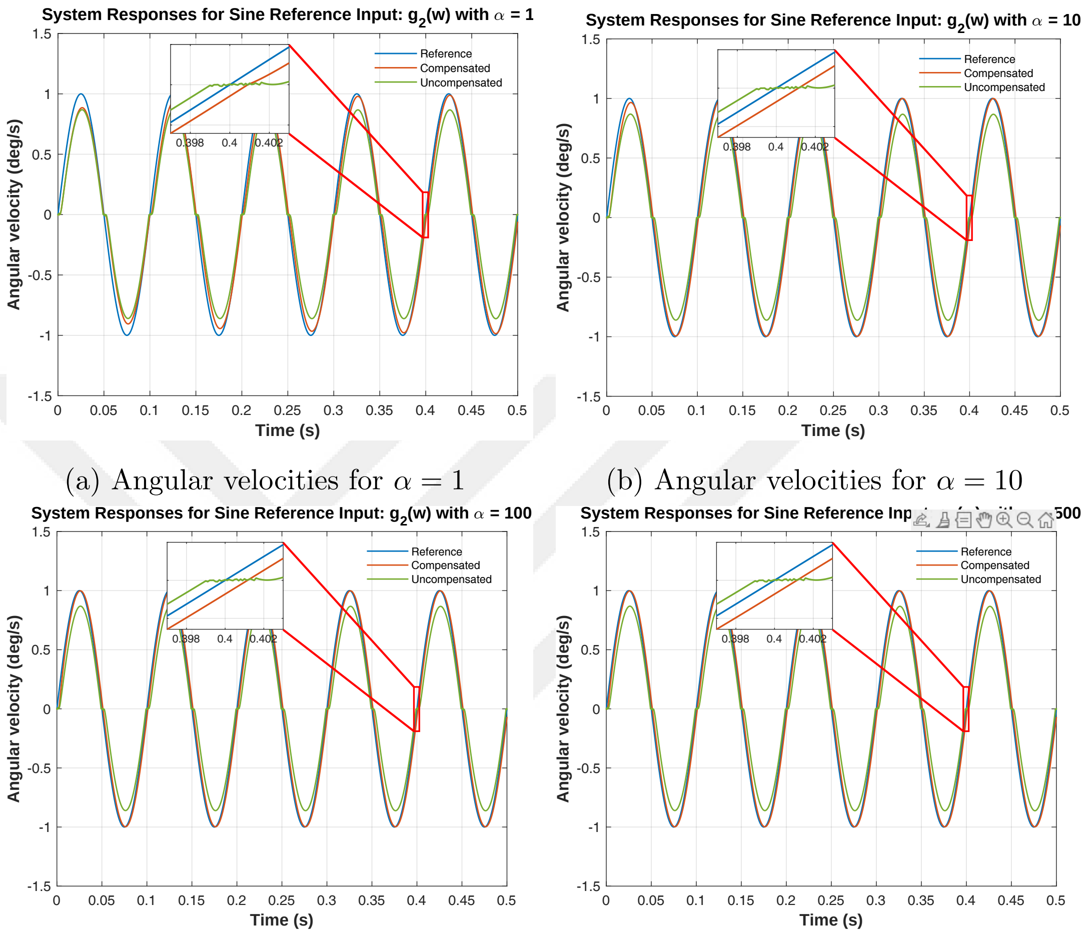

(a) Angular velocities for $\alpha = 1$

(b) Angular velocities for $\alpha = 10$

(c) Angular velocities for $\alpha = 100$

(d) Angular velocities for $\alpha = 500$

Figure A.4: Friction compensated and uncompensated angular velocity responses of the system for 10 Hz sine wave input with different α parameters of $g_2(w)$ for MFP observer

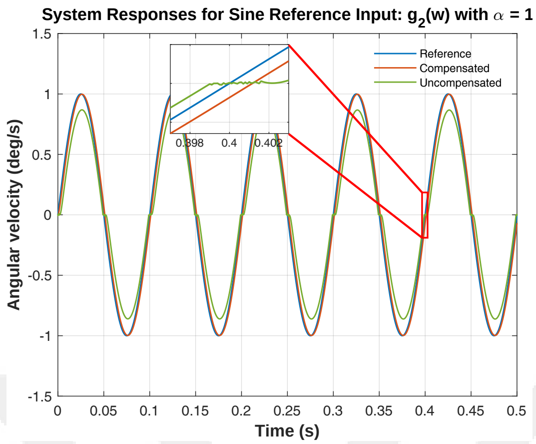

(a) Angular velocities for $\alpha = 1$

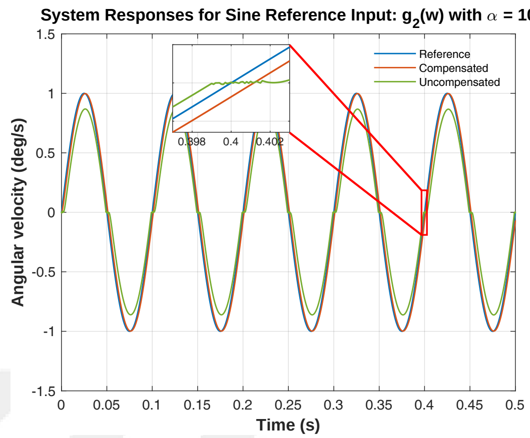

(b) Angular velocities for $\alpha = 10$

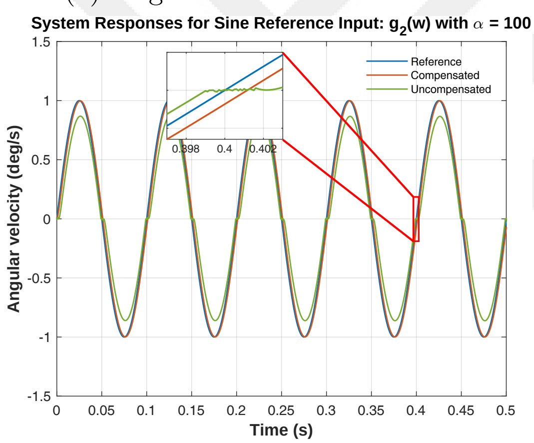

(c) Angular velocities for $\alpha = 100$

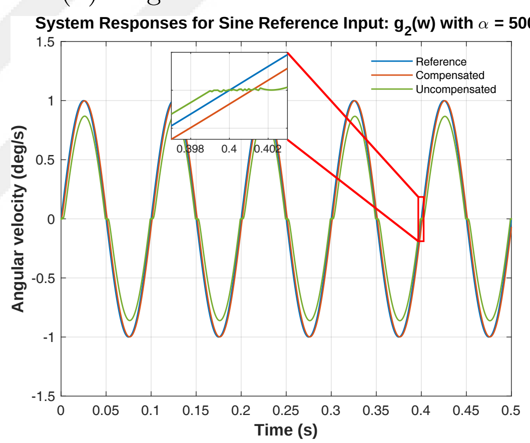

(d) Angular velocities for $\alpha = 500$

Figure A.5: Friction compensated and uncompensated angular velocity responses of the system for 10 Hz sine wave input with different α parameters of $g_2(w)$ for NFP observer

Appendix B

Code for finding the optimum observer parameters

```
%% Finding the optimum observer gain using abs error
k_est = 0;
a_g2v = 10;
b_est = 0;
a_g1v = 100;
modelName = 'FriedlandPark';
MSE_k_est = 1000;
MSE_b_est = 1000;
MSE_out = 1000;
step_size_k_est = 10;
step_size_b_est = 50;
thresh = 0.001;
count = 0;
sim_count = 20;
MSE_est_log = zeros(1,sim_count);
k_est_log = zeros(1,sim_count);
b_est_log = zeros(1,sim_count);

a_g2_v_arr = zeros(1,4);
a_g1_v_arr = zeros(1,4);
```

```
k_est_arr = zeros(1,4);
b_est_arr = zeros(1,4);
MSE_arr = zeros(1,4);
sampling_time= 0.0001;
sampling_freq = 1/sampling_time;
while (count < sim_count)
    if MSE_out < thresh
        break
    end
    count = count + 1;
    a_g2v_temp = a_g2v;
    a_g2v = a_g2v + step_size_k_est;
    a_g2_v_arr(1) = a_g2v;
    a_g1v_temp = a_g1v;
    a_g1v = a_g1v + step_size_b_est;
    a_g1_v_arr(1) = a_g1v;
    load_system(modelName);
    simOut = sim(modelName);
    outputData_k_1 = simOut.get('k_est_tanh');
    k_est_ss = outputData_k_1.Data;
    k_est_arr(1) = k_est_ss(end);
    outputData_b_1 = simOut.get('lam_est_tanh');
    b_est_ss = outputData_b_1.Data;
    b_est_arr(1) = b_est_ss(end);
    n = length(k_est_ss);
    % n_xd = length(k_est_ss(17000:end));
    MSE_est_pos_1 = abs(20-k_est_ss(end)) + abs(10-b_est_ss
       (end)) ;
    MSE_arr(1) = MSE_est_pos_1;

    a_g2v = a_g2v_temp;
    a_g2v = a_g2v - step_size_k_est;
    a_g2_v_arr(2) = a_g2v;
    a_g1v = a_g1v_temp;
    a_g1v = a_g1v + step_size_b_est;
```

```
    a_g1_v_arr(2) = a_g1v;
    load_system(modelName);
    simOut = sim(modelName);
    outputData_k_2 = simOut.get('k_est_tanh');
    k_est_ss = outputData_k_2.Data;
    k_est_arr(2) = k_est_ss(end);
    outputData_b_2 = simOut.get('lam_est_tanh');
    b_est_ss = outputData_b_2.Data;
    b_est_arr(2) = b_est_ss(end);
    n = length(k_est_ss);
    % n_xd = length(k_est_ss(17000:end));
    MSE_est_pos_2 = abs(20-k_est_ss(end)) + abs(10-b_est_ss
       (end));
    MSE_arr(2) = MSE_est_pos_2;

    a_g2v = a_g2v_temp;
    a_g2v = a_g2v + step_size_k_est;
    a_g2_v_arr(3) = a_g2v;
    a_g1v = a_g1v_temp;
    a_g1v = a_g1v - step_size_b_est;
    a_g1_v_arr(3) = a_g1v;
    load_system(modelName);
    simOut = sim(modelName);
    outputData_k_3 = simOut.get('k_est_tanh');
    k_est_ss = outputData_k_3.Data;
    k_est_arr(3) = k_est_ss(end);
    outputData_b_3 = simOut.get('lam_est_tanh');
    b_est_ss = outputData_b_3.Data;
    b_est_arr(3) = b_est_ss(end);
    n = length(k_est_ss);
    % n_xd = length(k_est_ss(17000:end));
    MSE_est_pos_3 = abs(20-k_est_ss(end)) + abs(10-b_est_ss
       (end));
    MSE_arr(3) = MSE_est_pos_3;

```

```
    a_g2v = a_g2v_temp;
    a_g2v = a_g2v - step_size_k_est;
    a_g2_v_arr(4) = a_g2v;
    a_g1v = a_g1v_temp;
    a_g1v = a_g1v - step_size_b_est;
    a_g1_v_arr(4) = a_g1v;
    load_system(modelName);
    simOut = sim(modelName);
    outputData_k_4 = simOut.get('k_est_tanh');
    k_est_ss = outputData_k_4.Data;
    k_est_arr(4) = k_est_ss(end);
    outputData_b_4 = simOut.get('lam_est_tanh');
    b_est_ss = outputData_b_4.Data;
    b_est_arr(4) = b_est_ss(end);
    n = length(k_est_ss);
    % n_xd = length(k_est_ss(17000:end));
    MSE_est_pos_4 = abs(20-k_est_ss(end)) + abs(10-b_est_ss
       (end));
    MSE_arr(4) = MSE_est_pos_4;

    [out,ind] = sort(MSE_arr);
    MSE_out = out(1);
    MSE_ind = ind(1);
    a_g2v = a_g2_v_arr(MSE_ind);
    a_g1v = a_g1_v_arr(MSE_ind);
    k_est_log(count) = k_est_arr(MSE_ind);
    b_est_log(count) = b_est_arr(MSE_ind);
    MSE_est_log(count) = MSE_out;

    if count > 1
        if MSE_est_log(count) >= MSE_est_log(count-1)
            step_size_k_est = step_size_k_est/2;
            step_size_b_est = step_size_b_est/2;
        end
    end
```

```


    abs_error = MSE_out
    k_est_out = k_est_arr(MSE_ind)
    b_est_out = b_est_arr(MSE_ind)
end
```